THE RADIATION BELTS OF JUPITER

BY

JOSEPH JEAN CHARLES DEGIOANNI

B.Sc., McGill University, 1967
M.S., University of Illinois, 1969

THESIS

Submitted in partial fulfillment of the requirements
for the degree of Doctor of Philosophy in Astronomy
in the Graduate College of the
University of Illinois at Urbana-Champaign, 1973

Urbana, Illinois

THE RADIATION BELTS OF JUPITER

BY

JOSEPH JEAN CHARLES DEGIOANNI

B.Sc., McGill University, 1967
M.S., University of Illinois, 1969

THESIS

Submitted in partial fulfillment of the requirements
for the degree of Doctor of Philosophy in Astronomy
in the Graduate College of the
University of Illinois at Urbana-Champaign, 1973

Urbana, Illinois

THE RADIATION BELTS OF JUPITER

Joseph Jean Charles Degioanni, Ph.D.
Department of Astronomy
University of Illinois at Urbana-Champaign, 1973

A model of the Jovian radiation belts is assumed to consist of a dipolar magnetic field inclined ten degrees to the axis of rotation and of trapped relativistic electrons whose motions can be described by the guiding-center approximation. Synchrotron emission from these electrons results in the observed non-thermal microwave spectrum. The IBM 360/75 computer at the University of Illinois was used to calculate the Stokes parameters of synchrotron radiation integrated over a dipolar shell as a function of the energy-dependent variable $u' = \sqrt{B_S}\,\varepsilon/\varepsilon_0$ where B_S is the equatorial, surface magnetic field, ε is the electron energy, and ε_0 is the electron rest mass energy. The integration takes into account the partial eclipse of the dipolar shells by the planet at different System III longitudes. Furthermore, the Stokes parameters are integrated separately for two types of electron populations, i.e., one whose pitch angle distribution is isotropic, and another whose distribution is sharply confined to the magnetic equator.

The magnetosphere is divided into two zones near L = 2, the approximate distance at which the gravitational and the centrifugal forces are equal and oppose each other. The two zones are treated independently and are assigned intensity profiles which are based, in part, upon high-resolution observational data.

We find that the observed curvature in the radio spectrum implies the existence of a double belt system. The outer belt consists of low energy electrons ($u' = 60$ Gauss$^{1/2}$) whose equatorial density falls as L^{-4} for $L > 2$. The model predicts a peak equatorial electron density of about $60\ B_S^{-1}\ \text{cm}^{-3}$ at L = 2. The inner belt, located in the region

$1 < L < 2$ consists of higher energy electrons ($u' = 200$ Gauss$^{1/2}$) and has an equatorial density which is about one-half the peak density in the outer zone. The pitch angle distribution of the electrons becomes gradually more confined to the magnetic equator with increasing distance from the planet in the outer zone. We find that a distribution which is isotropic for $1.1 < L < 1.8$, 67 per cent confined(†) for $1.8 < L < 2$ and 80 per cent confined for $L > 2$ satisfactorily accounts for the degree of polarization and the intensity variation with rotation of the planet. The eclipse of the radiation belts by the planet satisfactorily explains the asymmetry of the observed radiation between northern and southern zenomagnetic latitudes of the Earth. The departure from a pure sinusoid in the variation of the orientation of the plane of polarization with Jovian rotation and the asymmetry in east-west components of the source on projected maps are probably better explained by a regional anomaly in the dipole field rather than occultation of the radiation belts by the planet. The broadening effect of the radiation belts with decreasing frequency of observation is clearly demonstrated. The observed spectral characteristics of the non-thermal emission are reproduced by the model although the peak in the spectrum of the total intensity is not as prominent as previously expected. This implies a brightness temperature for the thermal emission from the planetary disk of 180° K at 3000 MHz. B-L plots of the radiation belts show little fine structure except near the boundary of the outer belt with the more energetic inner belt. Electron fluxes are of the order of 1000 times those found in the terrestrial belts if the surface field on Jupiter is 30 Gauss.

(†) The confinement refers to the proportion of electrons which belongs to a population with equatorial pitch angle distribution of the form $\sin^{60}\alpha_e$. (See text, Chapter II, Section G).

ACKNOWLEDGMENT

I would like to thank my thesis advisor, Dr. John R. Dickel, for his constant support, guidance and encouragement during the course of this work.

I am also grateful to Dr. G. C. McVittie, Dr. G. W. Swenson, Dr. S. P. Wyatt, Dr. E. C. Olson, and Miss Murle Edwards for their valuable support and assistance.

In addition, I am indebted to many members of the staff at Northwestern University Medical School for their support and encouragement.

Thanks are due to Mrs. Holly Jimison for technical assistance in the preparation of my thesis.

Finally, I would like to acknowledge my deepest gratitude to Miss Jean C. Hager for her ever-present support, imagination, and patience, all of which have made this undertaking possible.

This research was supported in its early phases by the National Science Foundation Grant GP 8161 and in its last stage by the National Aeronautics and Space Administration Grant NGR-14-005-176. The research board at the University of Illinois provided computer funds.

TABLE OF CONTENTS

LIST OF FIGURES

Page

LIST OF TABLES

LIST OF SYMBOLS

α	electron pitch angle
ξ	angle between the velocity vector of the electron and the line of sight to the observer $\hat{n}$
$\tilde{\omega}$	angle between the direction of the magnetic field and the line of sight to the observer $\hat{n}$
χ	angle between the major axis of the polarization ellipse and the reference axis $\hat{e}_y$
λ	$\tan\lambda$ is the ratio of the principal axes of the polarization ellipse
I,Q,U,V	Stokes parameters as defined in Born and Wolf, 1965
η_f	flux density per unit volume at frequency f
$\eta_f^{(p)}$	polarized part of the total emission per unit volume at frequency f
$\eta(\varepsilon/\varepsilon_0)$	number density of electrons with energy $\varepsilon/\varepsilon_0$ in the range $\varepsilon/\varepsilon_0$ to $\varepsilon/\varepsilon_0 + d(\varepsilon/\varepsilon_0)$, where ε_0 is the rest mass energy
$\Gamma(\alpha)$	number density of electrons with pitch angle α in the range α to $\alpha + d\alpha$
f_B	local gyrofrequency
f_C	critical frequency
F, F_P, F_S	emission polarization functions of $x = f/f_C$
B_S	magnetic field strength at the equatorial surface of the planet
θ_0	zenomagnetic colatitude of the observer
λ_{III}	System III Central Meridian Longitude (CML)
Ω	rotation angle of the planet measured in the magnetocentric (MC) system
L	distance measured in units of the Jovian equatorial radius
θ_M	magnetic colatitude of the mirror point of electrons with the equatorial pitch angle α_e
$A(\varepsilon/\varepsilon_0)$	energy distribution function for a shell at the equatorial distance r_e

$N(r_e)$	number density of electrons as function of the equatorial distance r_e
u'	energy dependent variable, $u' = \sqrt{B_S}\,\varepsilon/\varepsilon_0$
u	energy dependent variable, $u = u'/(f^{1/2}L^{3/2})$
K_q	normalization constant for the equatorial pitch-angle distribution
m_0	fraction of particles which belong to a population with an isotropic pitch angle distribution
m_{60}	fraction of particles which belong to a population with a pitch angle distribution of the form $\sin^{60}\alpha_e$
NQ	ratio m_{60}/m_0
Δ	measure of asymmetry in the intensity of emission between northern and southern zenomagnetic colatitudes
P_{NT}	fractional degree of polarization of the non-thermal (synchrotron) emission
R	ratio of the flux density at 1430 MHz of the outer and inner zones, $R = F_0(1430)/F_i(1430)$
C	spectral index between f = 1000 MHz and f = 3000 MHz
$J(\theta)$	omnidirectional electron flux as function of the magnetic colatitude θ

CHAPTER I. INTRODUCTION

A. General Conditions

A simplified model of the Jovian magnetosphere consists of a thermal plasma with superimposed radiation belts. Recently Melrose (1966) and Ioannidis and Brice (1971) have described the possible sources and distribution of the thermal plasma trapped in the magnetosphere of Jupiter. The model to be described here deals exclusively with the cloud of relativistic electrons which forms the radiation belts at a distance of a few Jovian radii from the planet and is responsible for the intense continuum of decimetric emission. The purpose of this model is to describe the structure of the radiation belts on the basis of the observations of their continuum emission at decimetric wavelengths. Most of this data was obtained in the past decade and consists of the following: (i) observations of the integrated flux in the decimetric continuum (See Figure 16a); (ii) observations of the degree of polarization of the radiation (See Figures 17 and 18); (iii) observations of the dependence on the rotation of Jupiter (or dependence on the System III longitude) of the integrated flux, degree of polarization, and orientation of the plane of polarization (See Figure 33a); (iv) high-resolution interferometric studies of the radiation belts (Berge, 1966; Branson, 1968); (v) lunar occultation studies of the radiation belts (Gulkis, 1970). In addition, the non-thermal emission is separated from the thermal emission of the planetary disk with the aid of the observations by Berge (1966) and Branson (1968) and models of Jupiter's atmosphere by Goodman (1969).

The model is derived using the following assumptions: (i) The radiation belts are located in a cavity of the Jovian magnetosphere and

the field geometry in that cavity is a pure dipole. Its magnetic moment points in the direction of the Northern Hemisphere and is inclined 10^{o} from the rotational axis of the planet; (ii) The conductivity in the Jovian ionosphere is large enough to force the magnetosphere to corotate; (iii) The population of electrons in the radiation belts is in a steady state, and the observational data are representative of such average conditions; (iv) The non-thermal continuum is produced by the synchrotron radiation of trapped relativistic electrons.

The dipolar approximation for the trapping zone is probably more valid for Jupiter than it is for the Earth because the energy density of the solar wind falls off as the inverse square of the distance from the Sun. The ratio of the size of the Jovian cavity to the terrestrial cavity is 5.3 in units of the respective planetary radii (Melrose, 1966). Thus, if the distance to the boundary of the magnetosphere of the Earth on the day side is 10 Earth radii, the corresponding distance on Jupiter is 53 Jovian radii. The solar wind, as a consequence, is unlikely to affect the magnetosphere of Jupiter in the way that it affects that of the Earth. In particular, the trapping zone, hereafter described at less than six Jovian radii, is probably relatively free from any deformities and asymmetries on the day and night sides of the planet. There is no evidence for a significant contribution from a quadrupole moment. The tilt of the dipolar axis to the axis of rotation is obtained from the amplitude in the oscillations of the plane of polarization with rotation of the planet and is probably one of the most accurately measured quantities. The sign of the magnetic moment follows from the observed right-handed polarization of the decametric emission (Warwick, 1967).

B. Particle Trapping and Energies

Hones and Bergeson (1965) show that the plasma around a rotating, conducting, magnetized sphere with its magnetic dipole axis and rotational axis oriented at an angle to each other will corotate with the sphere if the plasma particles are constrained to move along the field lines.

The trapping potential of the Jovian magnetosphere can be demonstrated as follows. The equations below represent the inner and outer boundaries enclosing the allowed (trapping) shell for particles with a Störmer constant γ (Störmer, 1955)(a parameter having the dimension of length which is determined by the initial conditions of particle injection into the dipole field).

$$\frac{r_1}{b} = \frac{\cos^2 \lambda}{-(\gamma/b) + [(\gamma/b)^2 + \cos^3 \lambda]^{1/2}} ,$$

and

$$\frac{r_2}{b} = \frac{\cos^2 \lambda}{-(\gamma/b) + [(\gamma/b)^2 - \cos^3 \lambda]^{1/2}} ,$$

where $b = \left(\frac{|e|M}{pc}\right)^{1/2}$ and also has the dimensions of length, λ is the magnetic latitude, M is the magnetic moment, e and p are the charge and momentum of the electron, respectively, and c is the speed of light. Setting $\gamma = b$ and solving for the outermost extent r_2 (at $\lambda = 0^\circ$) of a shell containing relativistic electrons of energy pc, one finds the following relations [assuming Warwick's (1967) magnetic moment $M = 4.24 \times 10^{30}$ Gauss-cm^3].

r_1(MIN) (JOVIAN RADII)	r_2(MAX)	ELECTRON ENERGY (Mev)
1.24	3.00	2.8×10^6
2.07	5.00	1.0×10^6
3.31	8.00	3.9×10^5
4.97	12.00	1.7×10^5
6.21	15.00	1.1×10^5

These results predict that the Jovian magnetosphere could hold electrons with energies in the range of millions of electron volts. It is very unlikely that any mechanism could be so efficient as to produce such energetic particles. Electrons in the range $1\text{-}10^2$ Mev are more plausible and sufficient to explain the radiation as described in Chapter III. Again, assuming Warwick's (1967) magnetic moment, b equals $5000/\sqrt{E}$ (in Jovian radii) for a relativistic electron with energy E (Mev). Thus, in the energy range $1\text{-}10^2$ Mev, b is very large and from the equations above we may use the approximation (Van Allen, 1967)

$$r_2 \rightarrow r_1 \rightarrow (-b^2/2\gamma) \cos^2 \lambda \quad ,$$

which is true in the limit $b \rightarrow \infty$. This is the equation for a line of force and says that for trapped particles in the energy range $1\text{-}10^2$ Mev the two bounding surfaces r_1 and r_2 closely approach the same magnetic shell. In other words, the field is so strong that the injection of a particle within the plausible range of energy values will essentially "freeze" it to the field line at the site of injection, allowing only the motion parallel to the field line and a drift in longitude. The cyclotron oscillation around a field line will have an amplitude much smaller than the planetary radius.

In the balance of energy for the steady state the great unknown is the source of this energy. The net radiation from the belts amounts to about 6×10^{16} erg sec^{-1} (Gary, 1963). There are an estimated 10^{29} electrons in the "visible" radiation belts of Jupiter (Wilkinson, 1970) and the time required for an electron to lose half of its energy by synchrotron radiation is of the order of 100 days (Wilkinson, 1970).

A significant source of the energy for the radiation belts comes from interchange instability. This mechanism results from the finite conductivity of the ionosphere and causes an outward diffusion of plasma to occur beyond about eight Jovian radii. This outward convection is accompanied by an inward diffusion of particles from the solar wind into the magnetosphere. The particle energy would then increase almost as L^{-3} (where L is the distance from the planet in Jovian radii) so that solar wind electrons with energies of 100-500 eV at L = 50 would have an energy of about 1-5 MeV at L = 5 (Ioannidis and Brice, 1971). Further inward, diffusion beyond the region of interchange would be expected to be slow, but this mechanism can provide a significant source of high energy electrons relatively close to the planet as required to explain the decimetric radiation (Drake and Hvatum, 1959; Warwick, 1967).(*) Neutron albedo, so effective on Earth (Hess, 1965), might populate only the very inner regions of the magnetosphere since most neutrons will probably decay before they reach the radiation zones, because their lifetime is relatively short (1000 seconds) and the distance scale on Jupiter is increased by a factor of 10 relative to the Earth.

Other possible sources of energy could result from intermittent major deformations of the magnetosphere. These could be produced by

---

* Further investigation should be carried out to evaluate the efficiency of this mechanism to supply the density of relativistic electrons in the radiation belts described in Chapter III.

oscillations in the shock boundary of the heliosphere since the latter may coincide with the magnetosphere, particularly during solar minimum (Lanzerotti and Schulz, 1969). An indication of another major deformation is the correlation between the position of the moon Io and the decametric bursts. Another possible factor is satellite V which,orbiting at 2.5 Jovian radii,could produce enough field disturbance to effect energy changes in the radiation belts.

CHAPTER II. THE STOKES PARAMETERS FOR SYNCHROTRON RADIATION IN A DIPOLAR FIELD

A. Stokes Parameters of Synchrotron Radiation by a Single Electron in the General Case

Let us consider a relativistic electron moving with velocity $\vec{\beta}(t)$ at time t in a magnetic field $B\hat{k}$ (See Figure 1). α is the pitch angle or angle between the field direction $\hat{k}$ and the velocity vector $\vec{\beta}(0)$ of the electron at the time of injection t = 0. The observer lies in the direction $\hat{n}$. ξ is the angle between $\hat{n}$ and the velocity vector at time t. $\tilde{\omega}$ is the angle between the field direction and $\hat{n}$. Two cases are shown: for $\tilde{\omega} < \frac{\pi}{2}$ and $\tilde{\omega} > \frac{\pi}{2}$.

Synchrotron radiation takes place within a very narrow cone centered about the instantaneous direction of motion. This is typical of the radiation patterns of relativistic particles regardless of the vectorial relationship between $\vec{\beta}$ and $\dot{\vec{\beta}}$. The root-mean-square angle of emission of the radiation in the relativistic limit is $\langle\xi^2\rangle^{1/2} = 1/\gamma = \varepsilon_0/\varepsilon$, where ε_0 is the rest energy of the electron (Jackson, 1966). For $\varepsilon = 0$, the major axis of the polarization ellipse is perpendicular to the projection of $\hat{k}$ onto a plane normal to $\hat{n}$, i.e., parallel to $\hat{i}_2 = -\hat{k} \times \hat{n}$. As ε increases, the form of the ellipse varies from circular to elliptic with the major axis parallel to the projection of $\hat{k}$ onto the plane normal to $\hat{n}$, i.e., parallel to $\hat{i}_1 = (\hat{k} \times \hat{n}) \times \hat{n}$. Furthermore, as shown in Figure 1, the sense of description of the ellipse is right-handed (RH) or left-handed (LH) depending upon whether $\tilde{\omega}$ is in the first or second quadrant.

For highly relativistic particles, $\langle\xi^2\rangle^{1/2}$ much less than 1, we may approximate the pattern of emission by assuming that radiation is detected

by the observer only when the electron moves within an angular distance of the order of $\langle\xi^2\rangle^{1/2}$ from the direction to the observer. Using this degree of approximation, Westfold (1959) has shown that the major axis of the polarization ellipse remains perpendicular to the projection of $\hat{k}$ onto a plane normal to $\hat{n}$. Thus, we may apply the geometry adopted by Thorne (1963) to describe the Stokes parameters of such elliptically polarized light with respect to the fixed reference axis $\hat{e}_y$ (Chandrasekhar, 1950) (See Figure 1).

$$I = I_1 + I_2 \quad , \tag{1}$$

$$Q = (I_1 - I_2) \cos 2\lambda \cos 2\chi \quad , \tag{2}$$

$$U = (I_1 - I_2) \cos 2\lambda \sin 2\chi \quad , \tag{3}$$

and

$$V = (I_1 + I_2) \sin 2\lambda \quad , \tag{4}$$

where I_1 is the mean intensity of the emission with the electric vector in the direction $-\hat{k} \times \hat{n}$; I_2 is the mean intensity with the electric vector in the direction $(\hat{k} \times \hat{n}) \times \hat{n}$; χ is the angle made by the major axis of the polarization ellipse with the reference axis $\hat{e}_y$; $|\tan \lambda|$ is the ratio of the principal axes ($-\frac{\pi}{4} \leq \lambda \leq \frac{\pi}{4}$), and the sense of description of the ellipse is right-handed (RH) for $\lambda > 0$ and left-handed (LH) for $\lambda < 0$.

B. Stokes Parameters of Synchrotron Radiation by an Assembly of Electrons in the General Case.

The Stokes parameters of an assembly of electrons are the sum of the parameters of the individual electrons. In a field geometry where χ is a function of position, we may assign the same χ for a group of

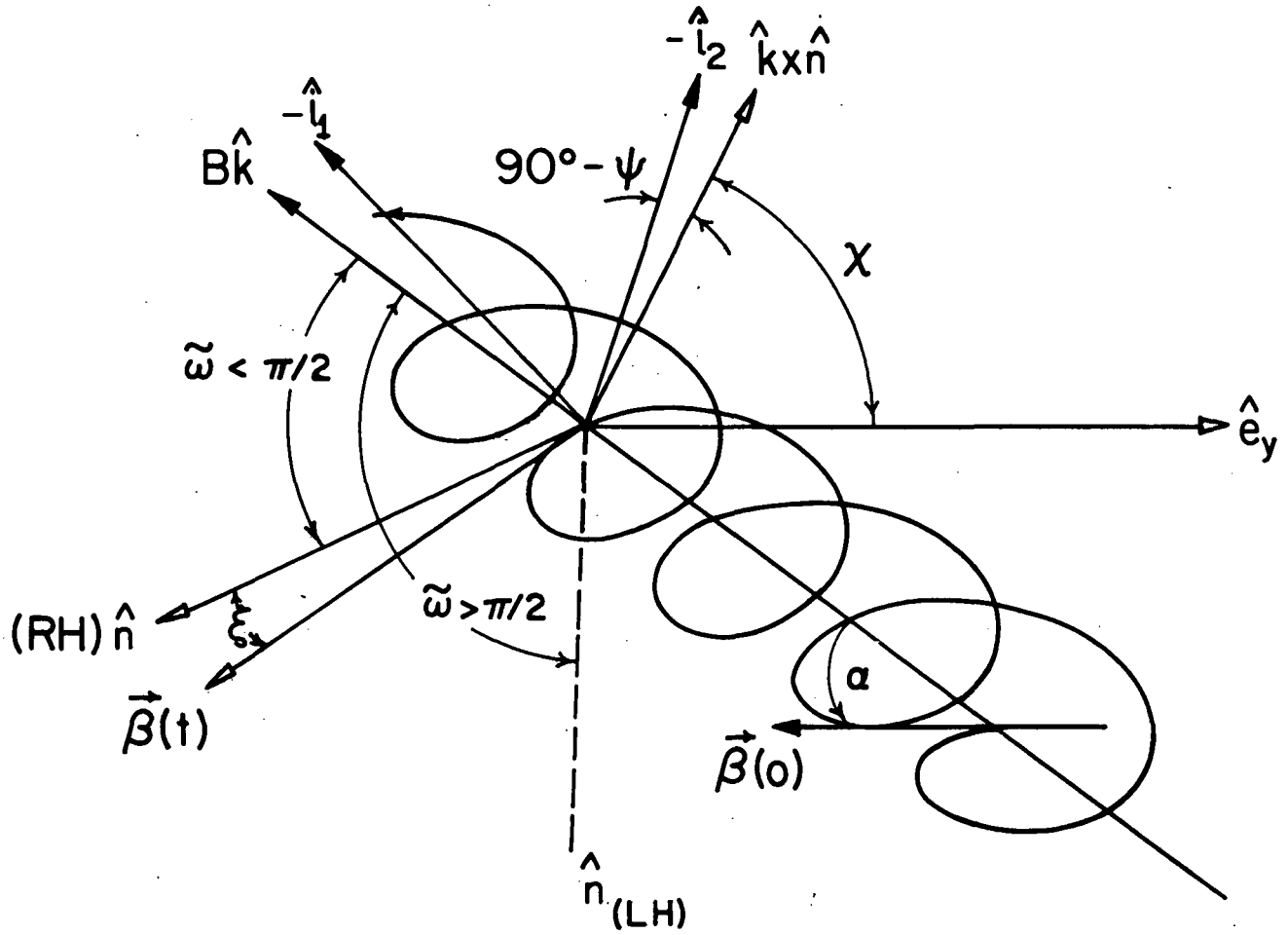

Figure 1. Right-handed helix formed by an electron injected with velocity $\vec{\beta}(0)$ ($\vec{\beta} = \vec{v}/c$) at an angle α to the magnetic field $B\hat{k}$. $\hat{n}$ is a unit vector in the direction of the observer and makes an angle ξ with the velocity of the electron $\vec{\beta}(t)$ at time t. $\tilde{\omega}$ is the angle between the field direction and $\hat{n}$. $\hat{i}_1$ and $\hat{i}_2$ are the two perpendicular components of the polarization ellipse (see the text). In the first and second orders of approximation for the radiation pattern described by Legg and Westfold (1968), the major axis of the polarization ellipse remains parallel to $\hat{i}_2 = -\hat{k} \times \hat{n}$, i.e., $\Psi = 90^o$. χ is the angle made by the major axis of the polarization ellipse with the reference axis $\hat{e}_y$.

electrons in a small enough volume dv. Thus by summing over the electrons with a given distribution in pitch angle and energy, we may obtain the Stokes parameters for the radiation from an elementary volume with respect to the reference direction $\hat{e}_y$.

In the first approximation the solution for an assembly of electrons is such that $V \equiv 0$ (Westfold, 1959). Subsequently, Legg and Westfold (1968) carry the solution to a second-order approximation in which they expand the angular distances of radiation detected to orders much less than $<\xi^2>^{1/2}$. Their results are such that the major axis of the polarization ellipse remain parallel to $\hat{i}_2$, i.e., $\Psi = 90^o$, so Equations (1) to (4) are still valid. However, now they obtain a non-zero solution for V which allows computation of the degree of circular polarization. Furthermore, their equations carry a correction which allows for the motion of the electron during the time interval of emission.

Using their results we find the Stokes parameters for a distribution of electrons radiating at a frequency f from an elemental volume dv at position $\vec{r}$:

$$I(f)dv = \eta_f(\vec{r})dv \ , \tag{5}$$

$$Q(f)dv = \eta_f^{(p)}(\vec{r}) \cos 2\lambda_f \cos 2\chi \ dv \ , \tag{6}$$

$$U(f)dv = \eta_f^{(p)}(\vec{r}) \cos 2\lambda_f \sin 2\chi \ dv \ , \tag{7}$$

and

$$V(f)dv = \eta_f^{(p)}(\vec{r}) \sin 2\lambda_f \ , \tag{8}$$

where $\eta_f^{(p)}$ is the polarized part of the total emission η_f per unit volume and λ_f, χ are defined as before. The properties of the radiation

field in terms of the Stokes parameters are as follows (Born and Wolf, 1965):

(i) The degree of polarization

$$P(f) = \frac{\sqrt{Q^2(f) + U^2(f) + V^2(f)}}{I(f)} \quad , \tag{9}$$

(ii) The degree of circular polarization

$$P_c(f) = \frac{V(f)}{I(f)} \quad , \tag{10}$$

(iii) The ellipticity (RH or LH)

$$\sin 2\lambda(f) = \frac{V(f)}{\sqrt{Q^2(f) + U^2(f) + V^2(f)}} \quad , \text{ and} \tag{11}$$

(iv) The angle χ which the major axis of the net polarization ellipse makes with the reference axis $\hat{e}_y$,

$$\tan 2\chi = \frac{U(f)}{Q(f)} \quad . \tag{12}$$

Equations (9) to (12) apply to the emission from the elemental volume dv but may be extended to the entire region of radiation if the Stokes parameters given in Equations (5) to (8) are integrated over that region.

The following results differ from Legg and Westfold's (1968) in that we compute the power <u>received</u> by the elemental source dv rather than the power <u>emitted</u> into the solid angle $d\Omega(\hat{n})$. Our expressions thus differ from Legg and Westfold's by the factor $\sin^{-2} \tilde{\omega}$ (Epstein and Feldman, 1967; Scheuer, 1968).

We have

$$\eta_f = \frac{\sqrt{3}}{2} \mu e^2 c \, \eta(\varepsilon/\varepsilon_0) \, \Gamma(\tilde{\omega}) \, f_B(\sin^{-1} \tilde{\omega}) \, F(f/f_c) \quad , \tag{13}$$

$$\eta_f^{(p)} \cos 2\lambda_f = \frac{\sqrt{3}}{2} \mu e^2 c \, \eta(\varepsilon/\varepsilon_0) \, \Gamma(\tilde{\omega}) \, f_B(\sin^{-1} \tilde{\omega}) \, F_p(f/f_c), \tag{14}$$

and $\eta_f^{(p)} \sin 2\lambda_f = \sqrt{2} \, \mu e^2 c \, \eta(\varepsilon/\varepsilon_0) \, \Gamma(\tilde{\omega}) \, f_B^{3/2}(\sin^{-1/2} \tilde{\omega}) \cot \theta \, f^{-1/2}$

$$\left\{ \left(\frac{f}{f_c}\right)^{1/2} F_s\left(\frac{f}{f_c}\right) + \left[2 + \frac{\Gamma'(\tilde{\omega})}{\Gamma(\tilde{\omega})} \tan \tilde{\omega}\right] \left(\frac{f}{f_c}\right)^{-1/2} \right.$$

$$\left. \left[F_p\left(\frac{f}{f_c}\right) - \frac{1}{2} F\left(\frac{f}{f_c}\right) \right] \right\} \quad , \tag{15}$$

where $\eta(\varepsilon/\varepsilon_0)$ is the number density of electrons with energy $\varepsilon/\varepsilon_0$ in the range $\varepsilon/\varepsilon_0$ to $\varepsilon/\varepsilon_0 + d(\varepsilon/\varepsilon_0)$, where ε_0 is the rest mass energy of the electron.

$\Gamma(\alpha)$ is the number density of electrons with pitch angle α in the range α to $\alpha + d\alpha$ (we assume axial symmetry about the direction of the magnetic field).

$\tilde{\omega}$ is the angle between the field direction and the direction to the observer $\hat{n}$ (See Figure 1).

f_B is the local gyrofrequency

$$f_B = \frac{eB}{2\pi m} \quad , \tag{16}$$

where B is the local magnetic field strength and e and m are the electron charge and mass, respectively.

f_c is the critical frequency, a characteristic of synchrotron

radiation defined by the local gyrofrequency and the energy of the electrons,

$$f_c = \frac{3}{2} f_B \sin \tilde{\omega} \, (\varepsilon/\varepsilon_0)^2 \quad , \tag{17}$$

where f is the frequency of emission and μ is the permeability of free space.

The functions F, F_p, F_s are the emissivity-polarization functions and are shown in Figure 2 as functions of $x = f/f_c$. They are also tabulated in Table 1. These functions can be expressed in terms of modified Bessel functions as follows (Legg and Westfold, 1968):

$$F(x) = x \int_x^\infty K_{5/3}(\eta) d\eta \quad , \tag{18}$$

$$F_p(x) = xK_{2/3}(x) \quad , \tag{19}$$

$$\text{and} \quad F_s(x) = xK_{1/3}(x) \quad . \tag{20}$$

The function F, which is a measure of the intensity of emission, shows a peak near x = 0.3, then falls rapidly with increasing argument and more slowly in the other direction. This behavior is characteristic of the synchrotron spectrum from a single electron for which the intensity falls proportionally to $\frac{f}{f_c} e^{-2f/f_c}$ for $f >> f_c$ and rises proportionally to $\left(\frac{f}{f_c}\right)^{2/3}$ for $f << f_c$ (Jackson, 1966).

C. Geometry for Determing the Stokes Parameters of Synchrotron Radiation by an Assembly of Electrons Trapped in a Dipolar Magnetic Field

In this development we shall use the guiding-center approximation in which the motion of a charged particle in a dipolar magnetic field is

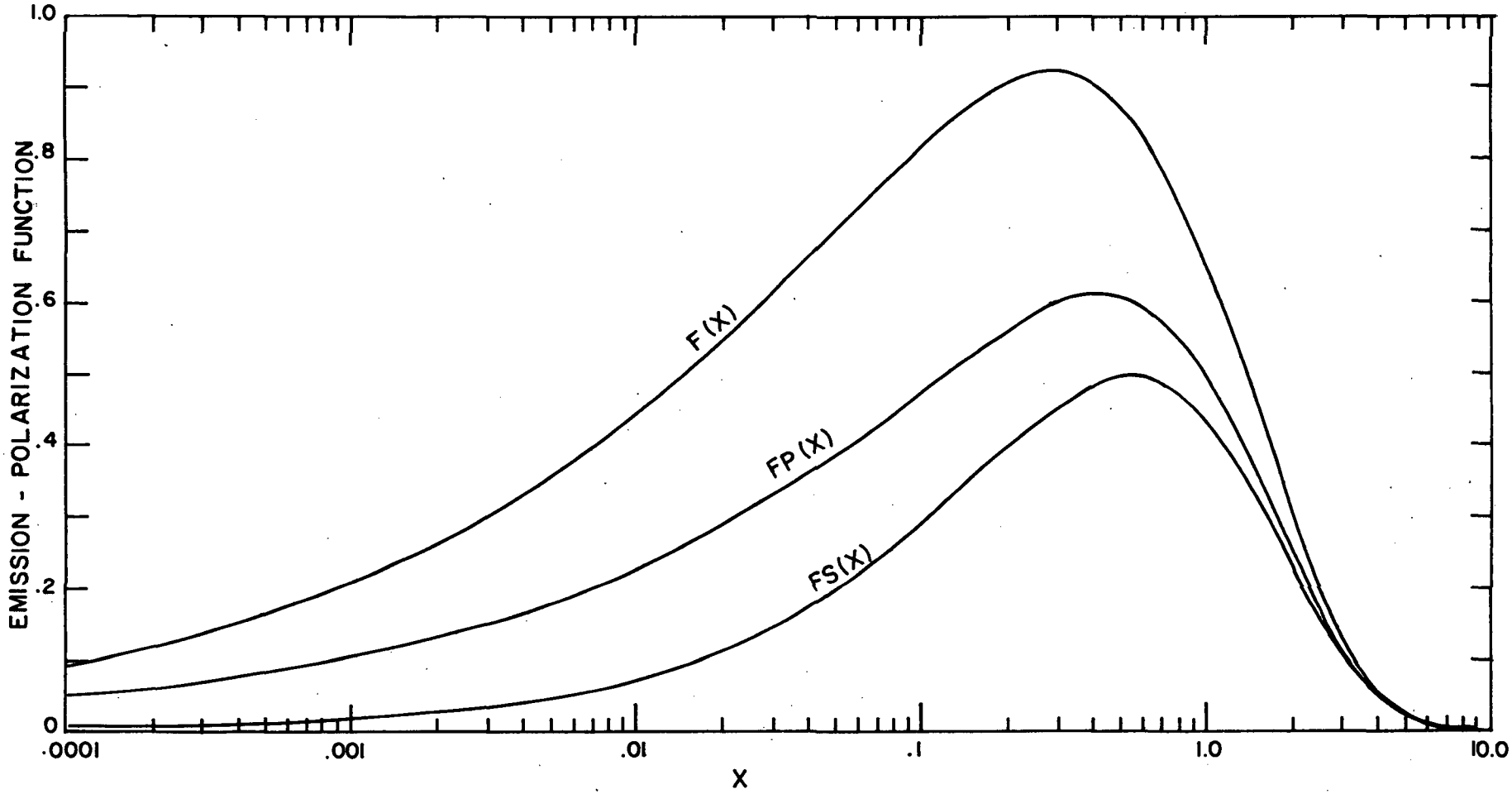

Figure 2. Emission-polarization functions F(x), $F_p(x)$, $F_s(x)$. The argument $x = f/f_c$ where f_c is the critical frequency, a characteristic of synchrotron radiation defined by the local gyrofrequency and the energy of the electrons [See Equation (17)].

TABLE 1

EMISSION-POLARIZATION FUNCTIONS $F(x)$, $F_p(x)$, $F_s(x)$

[See Equations (18) to (20) and discussion in the text.]

$x = f/f_c$	$F(x)$	$F_p(x)$	$F_s(x)$
0.0001	0.0995909	0.0498859	0.0036284
0.0002	0.1253424	0.0628517	0.0057527
0.0003	0.1433524	0.0719465	0.0075306
0.0004	0.1576531	0.0791866	0.0091143
0.0005	0.1697013	0.0853001	0.0105674
0.0006	0.1802100	0.0906437	0.0119238
0.0007	0.1895878	0.0954218	0.0132046
0.0008	0.1980935	0.0997636	0.0144238
0.0009	0.2059023	0.1037568	0.0155915
0.0010	0.2131390	0.1074638	0.0167150
0.0020	0.2671962	0.1353720	0.0263832
0.0030	0.3045747	0.1549299	0.0344066
0.0040	0.3339621	0.1704826	0.0415021
0.0050	0.3584969	0.1836005	0.0479686
0.0060	0.3797150	0.1950521	0.0539672
0.0070	0.3984971	0.2052783	0.0595977
0.0080	0.4154004	0.2145581	0.0649272
0.0090	0.4308024	0.2230806	0.0700034
0.0100	0.4449725	0.2309808	0.0748622
0.0200	0.5472394	0.2899581	0.1156112
0.0300	0.6136067	0.3305130	0.1479630
0.0400	0.6627958	0.3620823	0.1754438
0.0500	0.7015719	0.3880966	0.1995509
0.0600	0.7332474	0.4102468	0.2211043
0.0700	0.7597221	0.4295097	0.2406184
0.0800	0.7821986	0.4465081	0.2584440
0.0900	0.8014925	0.4616682	0.2748348
0.1000	0.8181855	0.4752962	0.2899828
0.2000	0.9033859	0.5603580	0.3958682
0.3000	0.9177054	0.5959857	0.4527338
0.4000	0.9019372	0.6068523	0.4823055
0.5000	0.8708190	0.6029652	0.4945155
0.6000	0.8314753	0.5896982	0.4950563
0.7000	0.7878751	0.5703488	0.4875710
0.8000	0.7424131	0.5470969	0.4745441
0.9000	0.6966028	0.5214492	0.4577372
1.0000	0.6514226	0.4944750	0.4384307
2.0000	0.3016351	0.2496773	0.2330897
3.0000	0.1285657	0.1111717	0.1059188
4.0000	0.0528253	0.0469216	0.0451991
5.0000	0.0212482	0.0192229	0.0186461
6.0000	0.0084285	0.0077283	0.0075276
7.0000	0.0032933	0.0030631	0.0029961
8.0000	0.0012845	0.0012028	0.0011796
9.0000	0.0004978	0.0004698	0.0004606
10.0000	0.0001919	0.0001816	0.0001788

broken down into three components: (i) the cyclotron motion -- a periodicity in the particle's motion perpendicular to the magnetic field; (ii) the bounce motion -- a periodic motion along a magnetic field line between mirror points; and (iii) the drift motion -- a periodic motion in longitude around the axis of the dipole.

The cyclotron motion has the highest frequency. Bounce frequencies are usually many orders of magnitude lower than cyclotron frequencies; drift frequencies, in turn, are several orders of magnitude lower than bounce frequencies. Typical values for the respective periods of a relativistic electron are 10^{-4} sec, 2×10^{-1} sec and 10^{6} sec (Hess, 1968). It is worth noting that an electron trapped in the dipolar field surrounding Jupiter will drift only a few degrees in longitude during a full rotation of the planet. Furthermore, it will drift about 40° in longitude during the characteristic time of energy decay by synchrotron emission (Wilkinson, 1970). For an electron, the sense of gyration of cyclotron motion is right-handed with respect to the direction of the magnetic field (See Figure 1). Thus if we neglect the azimuthal drift, the trajectory becomes a right-handed circular helix bound between mirror points located on opposite sides of the equatorial plane.

When considering an assembly of electrons, we will use Chang's approach (Chang, 1962) of applying Liouville's theorem to the electron motion. Let $n(\varepsilon/\varepsilon_0, \alpha, \vec{r})$ be the number of electrons at position $\vec{r}$ with energy $\varepsilon/\varepsilon_0$ in the range $\varepsilon/\varepsilon_0$ to $\varepsilon/\varepsilon_0 + d(\varepsilon/\varepsilon_0)$, where ε_0 is the rest mass energy of the electron, and pitch angle α in range α to $\alpha + d\alpha$. Thus $dN = n(\varepsilon/\varepsilon_0,\alpha,\vec{r})\, dV$ is the number of electrons that lie in the elemental volume of phase space $dV = dx\, dy\, dz\, dp_x\, dp_y\, dp_z$ where (x,y,z) and (p_x,p_y,p_z) are the position and momentum coordinates of the particles

comprising dN. Transforming into spherical coordinates we get $dV = dv(\vec{r})\ 2\pi \sin\alpha\ d\alpha p^2 dp$ where $dv(\vec{r})$ is the elemental volume in position space. If we move this small assembly of electrons dN along a field line from position $\vec{r}$ to the corresponding equatorial position $\vec{r}_e$ in a time short enough that energy losses may be neglected, it will occupy a new volume $dV' = dv(\vec{r}_e)2\pi \sin\alpha_e\ d\alpha_e p^2 dp$. According to Liouville's theorem, the density of such an assembly is a constant with respect to time. It follows that for a given dN the volume occupied in position-momentum space is an invariant and we may set

$$dv(\vec{r})2\pi \sin\alpha\ d\alpha p^2 dp = dv(\vec{r}_e)2\pi \sin\alpha_e\ d\alpha_e p^2 dp \quad . \quad (21)$$

But the number of electrons in our sample is

$$dN = n(\varepsilon/\varepsilon_0,\alpha,\vec{r})d\alpha\ d(\varepsilon/\varepsilon_0)dv(\vec{r}) = n(\varepsilon/\varepsilon_0,\alpha_e,\vec{r}_e)d\alpha\ d(\varepsilon/\varepsilon_0)dv(\vec{r}_e) \quad . \quad (22)$$

Combination of these equations yields

$$n(\varepsilon/\varepsilon_0,\alpha,\vec{r}) = \left|\frac{\sin\alpha}{\sin\alpha_e}\right| n(\varepsilon/\varepsilon_0,\alpha_e,\vec{r}_e) \quad . \quad (23)$$

We may relate the pitch angle α to the equatorial pitch angle α_e in terms of the field strength at the corresponding points of a field line. In order to achieve this, we neglect the curvature of the field lines, i.e., the azimuthal component of motion, and use the fact that a static magnetic field does no work on a particle. This means that the magnetic flux contained in the orbit of a particle rotating about a field line is a constant; for if $\partial B/\partial t \neq 0$, the electric field produced would accelerate the particles and their energy would change (Betatron mechanism).

Therefore, for a near-parallel and static magnetic field, it may be shown that the magnetic moment μ of the particle's gyration around the field line is an invariant of motion (if we neglect radiation losses). Thus we may set

$$\mu = \frac{1}{2B}(m\gamma c^2\beta^2 \sin^2 \alpha) = \frac{1}{2B_e}(m\gamma c^2\beta^2 \sin^2 \alpha_e) \quad , \tag{24}$$

where m is the rest mass of the electron, γ is the relativistic mass increase $(1 - \beta^2)^{-1/2}$, and $v = \beta c$ is the speed. B and B_e are the magnetic field strengths at position $\vec{r}$ and $\vec{r}_e$, respectively.

From Equation (24) we derive the relation,

$$\frac{\sin \alpha}{\sin \alpha_e} = \left(\frac{B}{B_e}\right)^{1/2} \quad . \tag{25}$$

Combination of Equations (23) and (25) yields

$$n(\varepsilon/\varepsilon_0,\alpha,\vec{r}) = \left(\frac{B}{B_e}\right)^{1/2} n(\varepsilon/\varepsilon_0,\alpha_e,\vec{r}_e) \quad . \tag{26}$$

In order to solve Equations (13) to (15) for a dipolar field geometry, we will use the geometrical expressions derived by Thorne (1963) (See Figure 3). Here, however, the direction of $\vec{B}$ will be opposite from that of his stellar model since Jupiter is known to possess a positive magnetic moment (Warwick, 1963). Also, we locate the observer at $\hat{n}$, in the x-z plane, making an angle θ_0 with the magnetic axis $\hat{e}_z$. In spherical coordinates, the magnetic field at $\vec{r} = (r,\theta,\phi)$ is $\vec{B}(\vec{r})$, and $\vec{r}_e = (r_e,\pi/2,\phi)$ is the point at which the field line crosses the equatorial plane. χ is the local angle between $\vec{B}(\vec{r}) \times \hat{n}$ and $\hat{e}_y$ (the polarization axis) and $\tilde{\omega}$ is the angle between $\vec{B}(\vec{r})$ and $\hat{n}$.

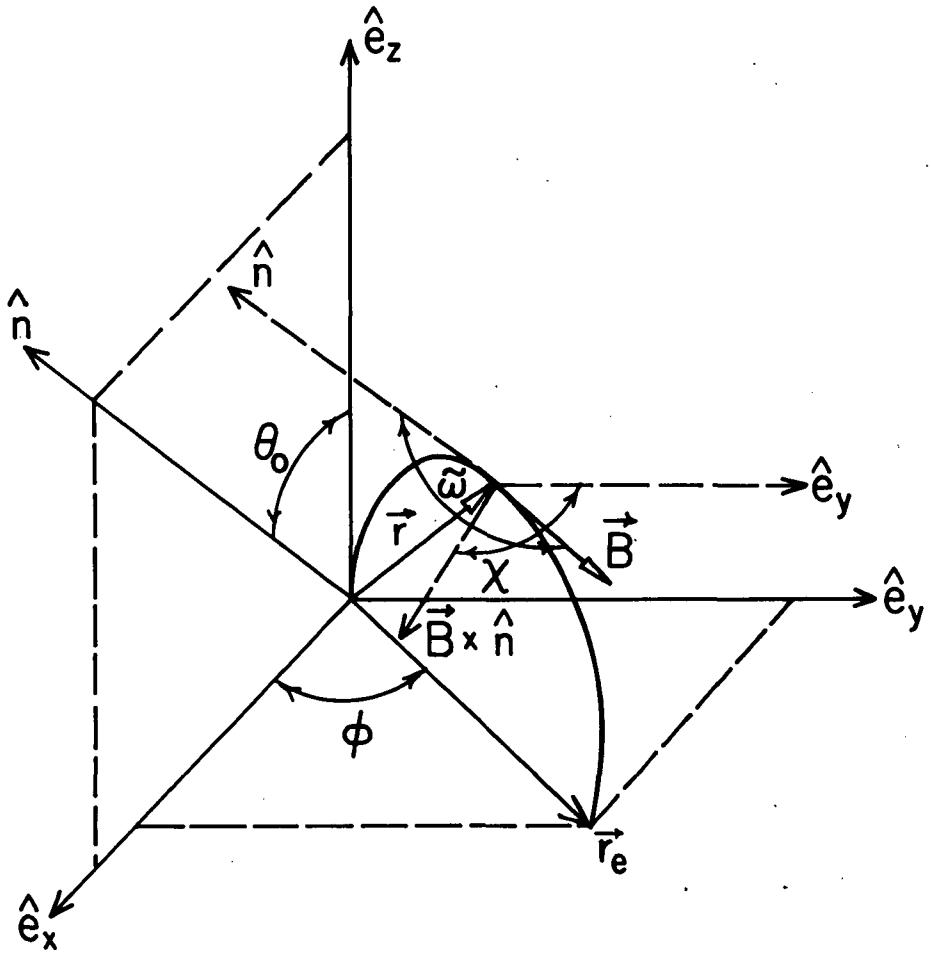

Figure 3. Dipolar field geometry with a positive magnetic moment for our Jovian model. $\hat{n}$ is a unit vector in the direction to the observer located in the x-z plane and θ_o is the magnetic co-latitude of the observer. $\vec{B} \times \hat{n}$ is in the direction of the linearly polarized electric vector (See discussion in Section 1). $\tilde{\omega}$ and χ are defined as in Figure 1. The fixed reference axis $\hat{e}_y$ is taken in the plane of the magnetic equator. ϕ is the magnetic longitude of the plane containing the field line $|\vec{r}| = |\vec{r}_e| \sin^2 \theta$ (Thorne, 1963).

The dipole field is given by

$$\vec{B} = + \frac{B_e}{\sin^6 \theta}(2 \cos \theta \hat{e}_r + \sin \theta \hat{e}_\theta) \ , \tag{27}$$

$$\text{and} \quad |\vec{B}| = \frac{B_e(1 + 3 \cos^2 \theta)^{1/2}}{\sin^6 \theta} \ , \tag{28}$$

where B_e is the equatorial magnetic field. It can be expressed in terms of the equatorial field of the planetary surface B_s by the relation $B_e = B_s(R_E/r_e)^3$ where R_E is the equatorial radius of the planet, and r_e is the equatorial distance from the center of the dipole.

The equation of the field lines is $r = r_e \sin^2 \theta$.

The equations for cos $\tilde{\omega}$, sin $\tilde{\omega}$, cos 2χ and sin 2χ are as derived by Thorne (1963) and are listed below:

$$\cos \tilde{\omega} = \frac{\rho}{\sqrt{h}} \qquad 0 \leq \tilde{\omega} \leq \pi \ , \tag{29}$$

where $\rho = a \cos \theta_0 + b \sin \theta_0$,

$a = 3 \cos^2 \theta - 1$,

$b = 3 \cos \theta \sin \theta \cos \phi$,

$h = 3 \cos^2 \theta + 1$,

$$\sin \tilde{\omega} = \sqrt{\frac{\sigma}{h}} \ , \tag{30}$$

where $\sigma = h - \rho^2$,

$$\cos\chi = \frac{b\cos\theta_0 - a\sin\theta_0}{\sigma^{1/2}} \quad , \tag{31}$$

$$\sin\chi = -\frac{b\tan\phi}{\sigma^{1/2}} \quad , \tag{32}$$

$$\cos 2\chi = 2\frac{(a\sin\theta_0 - b\cos\theta_0)^2}{\sigma} - 1 \quad , \tag{33}$$

$$\text{and} \quad \sin 2\chi = 2\frac{(a\sin\theta_0 - b\cos\theta_0)\, b\tan\phi}{\sigma} \quad . \tag{34}$$

In integrating the synchrotron emission over the entire dipole field, we shall use Chang's (1962) and Thorne's (1963) approach and take our differential volume along a tube of flux so that dv = dsdA where ds is a differential length along the field line and dA is the differential area crossed by a magnetic flux $B(\vec{r}_e)r_e d\phi dr_e$. As derived by these previous authors, we have the elemental volume,

$$dv = r_e^2 \sin^7\theta \, d\theta d\phi dr_e \quad . \tag{35}$$

D. Geometry of the Dipole Field as a Function of Planetary Rotation

The magnetic axis of Jupiter is inclined 10^o to the rotational axis. Thus, as the planet rotates the magnetic colatitude of the observer varies sinusoidally with an amplitude of 10^o (See Figure 4). In addition the amount of occultation of the radiating zone changes with rotation due to both the variation in the magnetic colatitude and the changing geometrical eclipse produced by the planet. Calculation of the latter effect requires a knowledge of the time or longitudinal dependence of a point $\vec{r}$ located in the magnetosphere. It is simpler to approach the problem by considering a planetocentric (PC system) which precesses clockwise

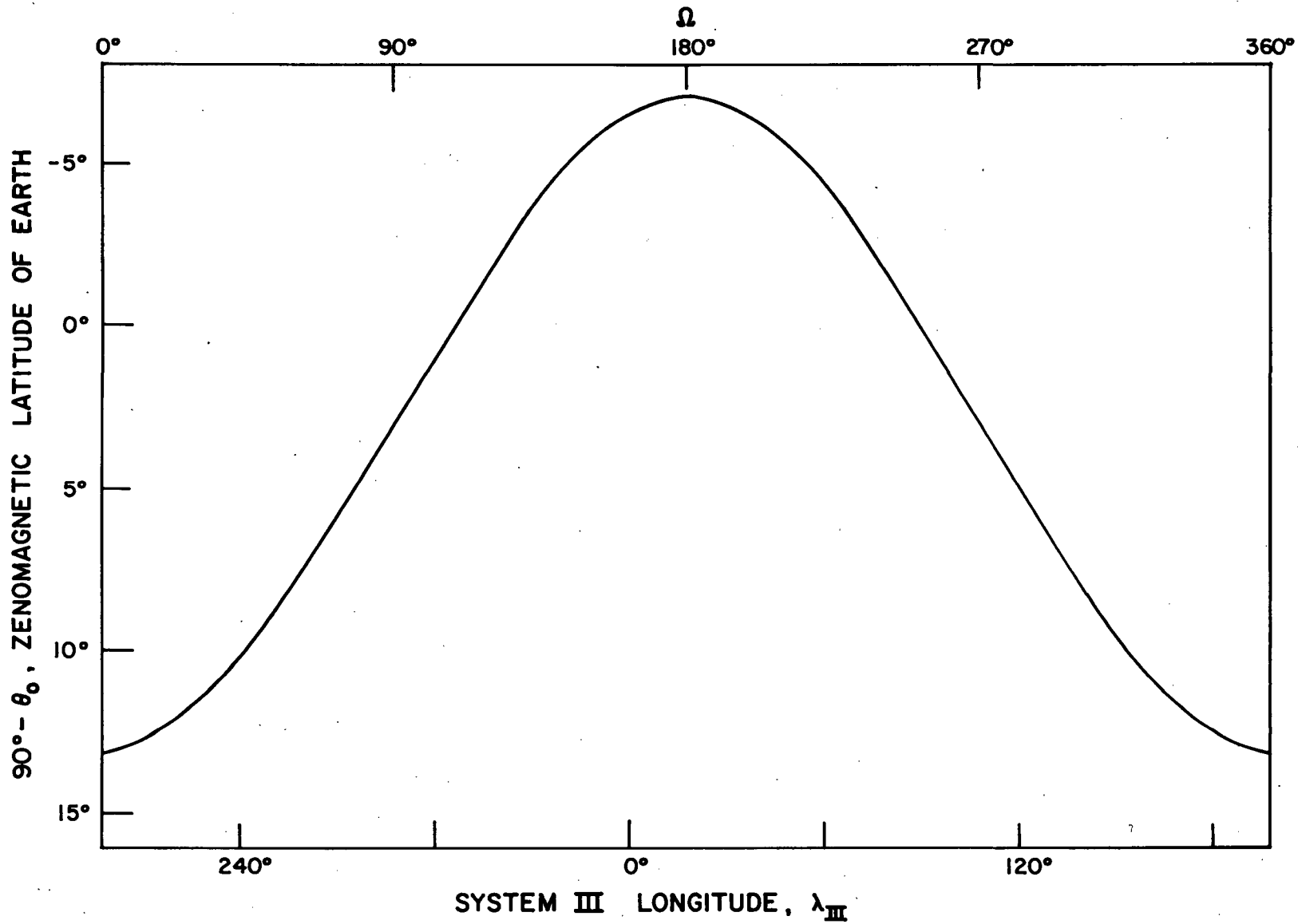

Figure 4. Zenomagnetic latitude ($90^{\circ} - \theta_0$) of the observer as a function of the planetary rotation. The planetocentric latitude of the Earth is assumed to be $+3^{\circ}$.

about a fixed magnetocentric (MC) system. The planetocentric colatitude of the observer is held constant at θ_0' but his magnetic colatitude oscillates with the planetary precession.

The system is examined in Figure 5 at time t. The positional coordinates of the planet's center in the magnetic system (MC) are $(x_p,y_p,z_p)_t$. We define $t = t_0$ as that time coinciding with the System III Central Meridian Longitude (CML) of $\lambda_{III}(t_0)$. At time t, the planet's new CML is $\lambda_{III}(t)$ where

$$\lambda_{III}(t) = \lambda_{III}(t_0) - \Omega(t) ,$$

in which $\Omega(t)$ is the angle of rotation of the planet's center measured in the magnetic equatorial plane with respect to a reference axis at time t_0.

In the general solution, the orientation of the planetary axis (z') with respect to the magnetic axis (z) is described in terms of the three Eulerian angles α, Ψ, and Ω_t (See Figure 5) (Goldstein, 1959).

Consider a point $(x,y,z)_t$ located in the MC system at time t. A transformation of this point into the PC system first involves three successive rotations represented by the following transformation matrices:

1. A clockwise rotation by Ω_t about z

$$A = \begin{pmatrix} \cos \Omega_t & -\sin \Omega_t & 0 \\ \sin \Omega_t & \cos \Omega_t & 0 \\ 0 & 0 & 1 \end{pmatrix} , \qquad (36)$$

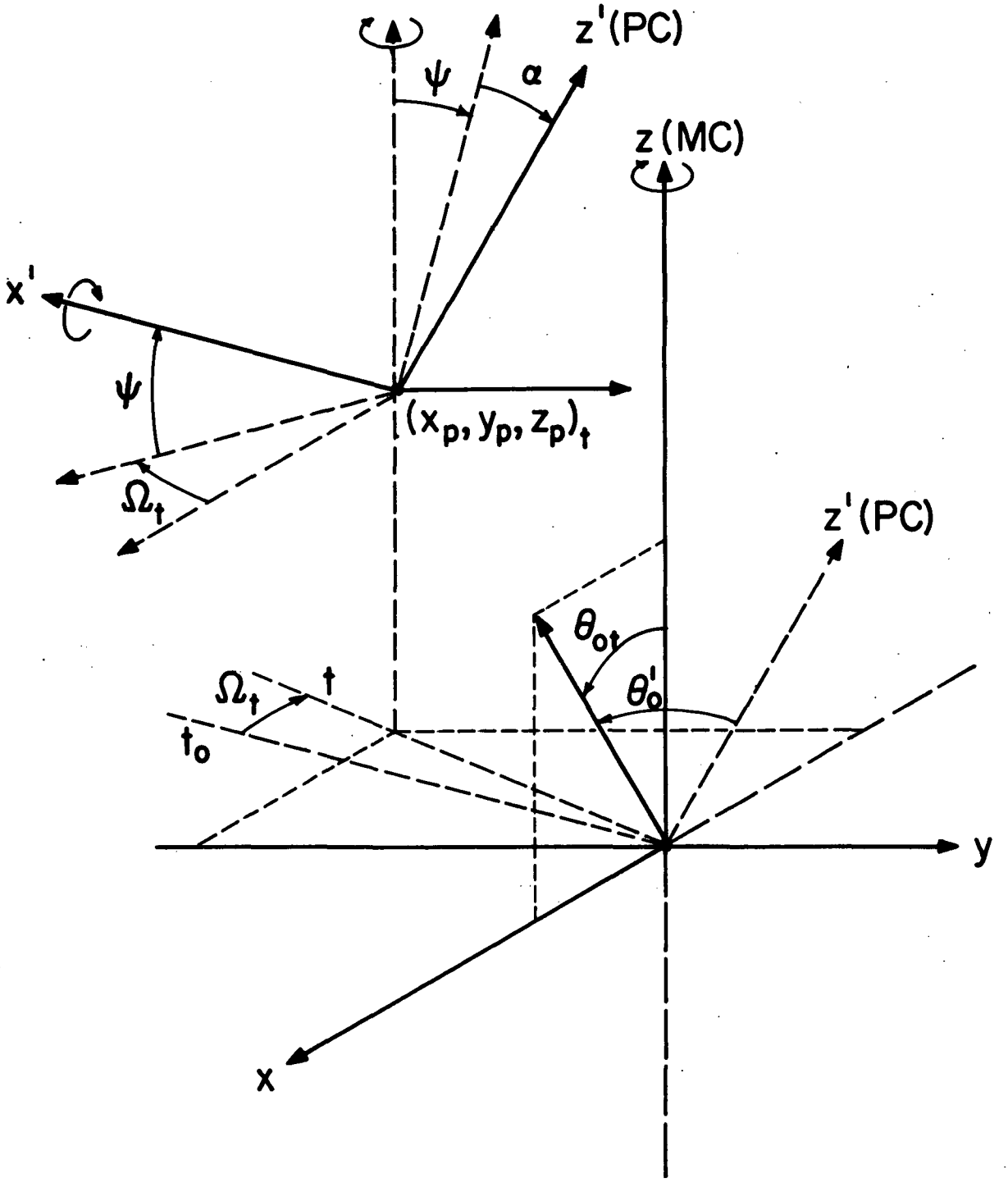

Figure 5. Geometry to calculate the longitudinal dependence of a point $\vec{r}$ located in the magnetosphere (MC) system and transformed into the planetocentric (PC) system. The observer is kept in the x-z plane of the MC system and the planet is allowed to precess clockwise about the MC system. The planetocentric colatitude of the observer θ'_0 is fixed at 87^o but the zenomagnetic colatitude varies from 77^o to 97^o as the planet rotates. In our model, $x_p = y_p = z_p = 0$ (planet-centered magnetosphere).

2. A counterclockwise rotation by Ψ about y

$$B = \begin{pmatrix} \cos\Psi & 0 & \sin\Psi \\ 0 & 1 & 0 \\ -\sin\Psi & 0 & \cos\Psi \end{pmatrix}, \text{ and} \tag{37}$$

3. A clockwise rotation by α about x

$$C = \begin{pmatrix} 1 & 0 & 0 \\ 0 & \cos\alpha & -\sin\alpha \\ 0 & \sin\alpha & \cos\alpha \end{pmatrix} . \tag{38}$$

The product matrix for the net transformation is T = CBA:

$$T = \begin{pmatrix} \cos\Psi\cos\Omega_t & -\cos\Psi\sin\Omega_t & \sin\Psi \\ \cos\alpha\sin\Omega_t + \sin\alpha\sin\Psi\cos\Omega_t & \cos\alpha\cos\Omega_t - \sin\alpha\sin\Psi\sin\Omega_t & -\sin\alpha\cos\Psi \\ \sin\alpha\sin\Omega_t - \cos\alpha\sin\Psi\cos\Omega_t & \sin\alpha\cos\Omega_t + \cos\alpha\sin\Psi\sin\Omega_t & \cos\alpha\cos\Psi \end{pmatrix} . \tag{39}$$

Now, let $\vec{V}'$ be a unit vector in the direction of the planetary pole. This vector when expressed in the MC system becomes

$$\vec{V} = \tilde{T}\vec{V}' ,$$

where $\tilde{T}$ is the inverse of the matrix T.

Then,

$$\vec{V} = \begin{pmatrix} -\cos \Omega_t \sin \Psi \cos \alpha + \sin \Omega_t \sin \alpha \\ \sin \Omega_t \sin \Psi \cos \alpha + \cos \Omega_t \sin \alpha \\ \cos \Psi \cos \alpha \end{pmatrix} . \quad (40)$$

As a result, we see that in the MC system, this vector becomes a function of time [through $\Omega(t)$] due to the planetary precession. We may represent the unit vector to the observer in the MC system as follows,

$$\hat{n}(t) = \begin{pmatrix} \sin \theta_{0t} \\ 0 \\ \cos \theta_{0t} \end{pmatrix} . \quad (41)$$

The angle θ_0' between $\vec{V}$ and $\hat{n}(t)$ is constant and given by the expression

$$\cos \theta_0' = \frac{\vec{V} \cdot \hat{n}(t)}{|\vec{V}|}$$

$$= \frac{(\sin \Omega_t \sin \alpha - \cos \Omega_t \sin \Psi \cos \alpha) \sin \theta_{0t} + \cos \Psi \cos \alpha \cos \theta_{0t}}{|\vec{V}|}, \quad (42)$$

which may be solved for $\theta_0(t)$ as a function of $\Omega(t)$ for a given planetary colatitude of the observer (θ_0'). These results are shown in Figure 4 for $\theta_0' = 87^\circ$.

Then, if $\vec{P}$ is an arbitrary vector located in the MC system with coordinates (x,y,z), the corresponding vector $\vec{P}'$ in the PC system is given by the transformation,

$$\vec{P}' = \begin{pmatrix} x' \\ y' \\ z' \end{pmatrix}_{PC} = TS \begin{pmatrix} x - x_p \\ y - y_p \\ z - z_p \end{pmatrix} \quad , \tag{43}$$

where the transformation

$$S = \begin{pmatrix} \cos \Omega_t & \sin \Omega_t & 0 \\ -\sin \Omega_t & \cos \Omega_t & 0 \\ 0 & 0 & 1 \end{pmatrix} \tag{44}$$

is required to keep the line of sight to the observer $\hat{n}_t$ in the x-z plane of the MC system.

Now we consider a position with coordinates (x,y,z) in the MC system and project it onto the ℓ-w plane in Figure 6 which is perpendicular to the instantaneous line of sight $\hat{n}(t)$. Simple geometry (Chang, 1962) can be used to show that the distance from the position (x,y,z) to the ℓ-w plane is

$$D = x \sin \theta_{0_t} + z \cos \theta_{0_t} \quad . \tag{45}$$

When the origin is taken at the center of the PC system, i.e., if we measure the quantity

$$D = (x - x_p) \sin \theta_{0_t} + (z - z_p) \cos \theta_{0_t} \quad , \tag{46}$$

then a negative D places the position (x,y,z) below the ℓ-w plane whereas a positive D places it above the ℓ-w plane, i.e., beyond and before a plane that cuts across the center of the planet perpendicular

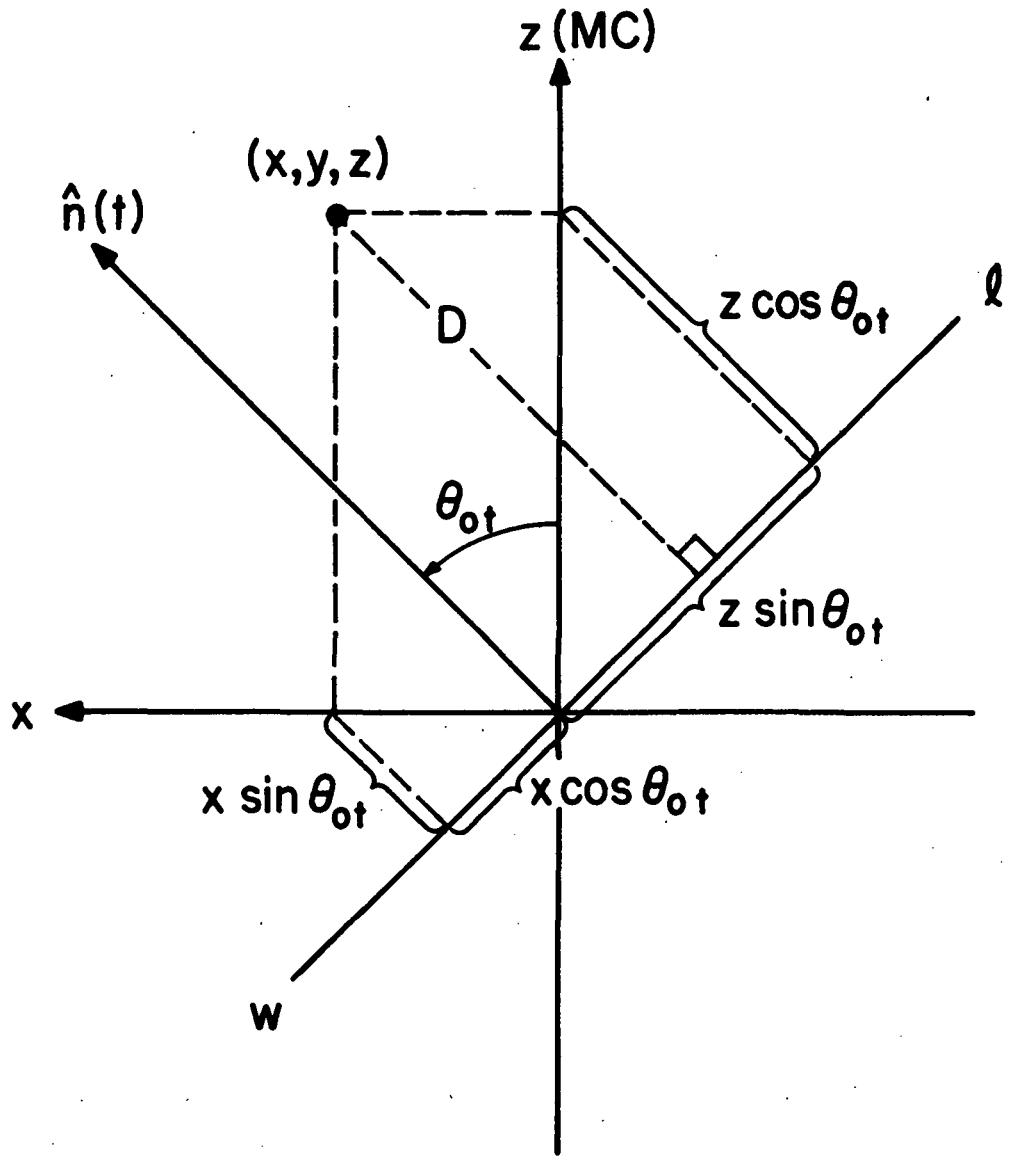

Figure 6. Projection of point (x,y,z) in the MC system onto a plane perpendicular (ℓ-w plane) to the line of sight $\hat{n}$ to the observer. The observer is located in the x-z plane of the MC system.

to the line of sight $\hat{n}(t)$. If we are concerned only with positions in the MC system associated with trapped electrons, we are assured by definition that all these points lie in the magnetosphere outside the surface of the planet. This leaves us with the problem of determining whether a point with negative D lies inside or outside the geometrical shadow of the planet. For this purpose we refer to Figure 6 and obtain the projection coordinates of (x,y,z) on the ℓ-w plane,

$$\ell = y \quad , \tag{47}$$

$$w = z \sin \theta_{0_t} - x \cos \theta_{0_t} \quad . \tag{48}$$

Substitution of the transformed coordinates (x',y',z') in Equations (47) and (48) allows computation of the corresponding projected point (ℓ',w') the PC system. If the projected point lies in the geometrical shadow of the planet system, the coordinates will, in turn, satisfy the equation

$$\frac{\ell'^2}{a_p^2} + \frac{w'^2}{b_p^2} \leq 1 \quad , \tag{49}$$

where a_p, b_p are the major and minor semiaxes (equatorial and polar radii, respectively) of the planet projected onto the plane perpendicular to the line of sight (defined by the planetocentric colatitude of the Earth θ_0').

We have calculated the Stokes parameters in Equations (5) to (8) for the particular case of a uniform dipolar field centered at the origin of Jupiter and inclined 10° to the rotational axis (Conway and Kronburg, 1968). We locate the North Magnetic Pole at CML = 198° (Warwick, 1963).

TABLE 2

CONVERSION OF THE SYSTEM III CENTRAL MERIDIAN LONGITUDE λ_{III} INTO THE ROTATIONAL ANGLE Ω INTRODUCED IN CHAPTER II, SECTION D

λ_{III} (degrees)	Ω (degrees)
0	162
20	182
40	202
60	222
80	242
100	262
120	282
140	302
160	322
180	342
200	2
220	22
240	42
260	62
280	82
300	102
320	122
340	142
360	162

By setting $\lambda(t_0) = 198^o$ and $\Omega(t_0) = 0$ we locate the North Magnetic Pole in the same plane as the observer at time t_0. We also have $x_p = y_p = z_p = 0$, $\alpha = 0$ and $\Psi = 0.175$ radians. Now, Equations (47) and (48) can be transformed into the PC system accordingly. We will use these expressions at five longitudes corresponding to $\Omega(t) = 0^o$, 45^o, 90^o, 135^o, 180^o. These expressions are, in order,

0^o) $\quad \ell' = Y \quad$ and

$$w' = -0.224951X + 0.974371Y \ , \tag{50}$$

45^o) $\quad \ell' = +0.712499X + 0.691014Y - 0.121845Z \quad$ and

$$w' = -0.036722X + 0.210134Y + 0.976984Z \ , \tag{51}$$

90^o) $\quad \ell' = +0.984808X - 0.173648Z \quad$ and

$$w' = +0.173410X + 0.052336Y + 0.983459Z \ , \tag{52}$$

135^o) $\quad \ell' = +0.712499X - 0.691014Y - 0.121845Z \quad$ and

$$w' = +0.036724X - 0.136688Y + 0.989934Z \ , \tag{53}$$

180^o) $\quad \ell' = -Y \quad$ and

$$w' = -0.121869X + 0.992547Z \ , \tag{54}$$

where

$$X = x \cos \Omega_t + y \sin \Omega_t \ ,$$

$$Y = -x \sin \Omega_t + y \cos \Omega_t \ ,$$

$$Z = z \ . \tag{55}$$

As before, (x,y,z) are the coordinates of a point located in the MC system.

It can be shown that the semiaxes of the elliptical shape of the planet projected onto the plane perpendicular to the line of sight (ℓ'-w' plane) are as follows,

$$a_p = R_E \quad \text{and} \tag{56}$$

$$b_p = R_p \cos \theta_0' \left(\frac{R_E}{R_p} + \tan^2 \theta_0' \right)^{1/2} , \tag{57}$$

where θ_0' is the planetocentric colatitude of the Earth and R_E, R_P are respectively the equatorial and polar radii of Jupiter.

We adopt the planetocentric declination of the Earth of $+3^o$, i.e., $\theta_0' = 87^o$. If we set $R_E = 1$, then $R_p = 0.939$, according to Dollfus (1970).

E. Limiting Equatorial Pitch Angle as Produced by the Planetary Surface

As described previously, electrons trapped in the radiation belts oscillate between mirror points symmetrically located above and below the magnetic equatorial plane. The latitude of these points is a function of the equatorial pitch angle of the electron. An absolute limit exists such that for equatorial pitch angles below a certain minimum [α_e(MIN)] the electron collides with the surface of the planet. This minimum decreases with increasing r_e as the electron can move into higher latitudes. Combining Equations (25) and (28) we have

$$\sin \alpha_e = \frac{\sin^3 \theta}{(1 + 3 \cos^2 \theta)^{1/4}} (\sin \alpha) \quad . \tag{58}$$

If we set $\alpha = 90^o$, then $\alpha_e = \alpha_e$(MIN) when $\theta = \theta_m$ is the polar angle at the point of intersection between the field line $r = r_e \sin^2 \theta$ and the surface of the planet.

α_e(MIN) was computed for Jupiter (with $R_p = 0.939$) as a function of the equatorial distance r_e. These results are shown in Figure 7. It is worth noting that for $\alpha = 90^o$ we obtain a relation between the equatorial pitch angle α_e and the magnetic colatitude of the mirror point (θ_M) as plotted in Figure 8.

F. The Stokes Parameters as a Function of the Energy-Dependent Variable $u' = \sqrt{B_s}\ \varepsilon/\varepsilon_0$

We consider the emission from a shell in the dipolar field which intersects the equatorial plane at the distance r_e from the center of the field. The purpose of this section is to express the Stokes parameters as functions of the equatorial number density of electrons with energy $\varepsilon/\varepsilon_0$.

It is assumed that the number density of electrons with energy $\varepsilon/\varepsilon_0$ in the range $\varepsilon/\varepsilon_0$ to $\varepsilon/\varepsilon_0 + d\ \varepsilon/\varepsilon_0$ and pitch angle α in range α to $\alpha + d\alpha$ at position $\vec{r}$ is a function of the number density at position $\vec{r}_e$ through Equation (23). Thus, combining Equations (23) and (58) we get

$$n(\varepsilon/\varepsilon_0,\alpha,\vec{r}) = \frac{(1 + 3\cos^2\theta)^{1/4}}{\sin^3\theta}\, n(\varepsilon/\varepsilon_0,\alpha,\vec{r}_e) \quad . \tag{59}$$

The equatorial density n may be expressed, in the manner of Chang (1962) and Thorne (1963), as follows

$$n(\varepsilon/\varepsilon_0,\alpha_e,\vec{r}_e) = 2\pi\Gamma(\alpha_e)\ \sin\alpha_e\ A(\varepsilon/\varepsilon_0)\ N(r_e) \quad , \tag{60}$$

where $\Gamma(\alpha_e)$ is the pitch angle density-function as described by Legg and Westfold (1968), $A(\varepsilon/\varepsilon_0)$ is the energy density function and $N(r_e)$ is the number density, all determined in the equatorial plane at distance r_e.

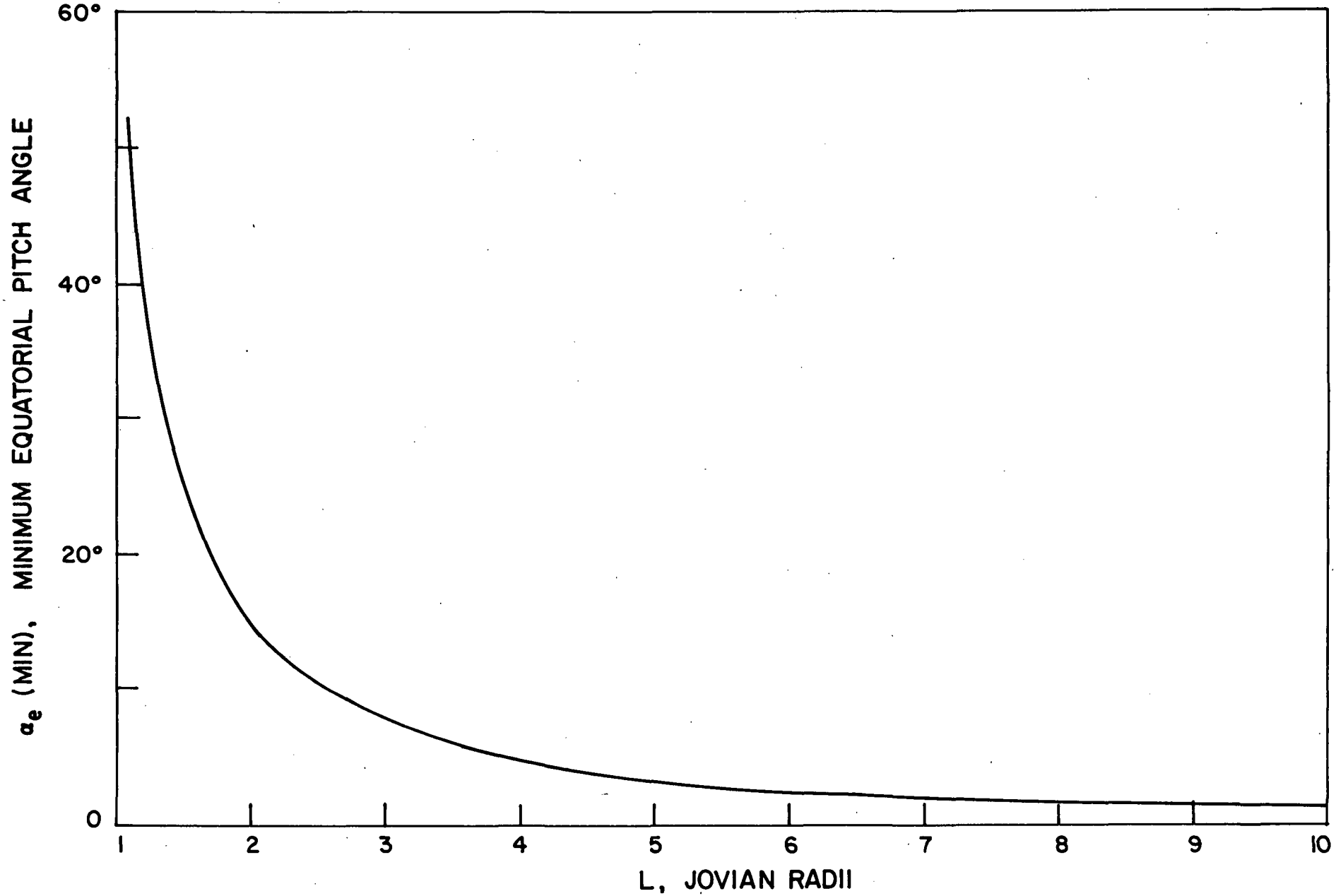

Figure 7. Minimum equatorial pitch angle [α_e (MIN)] as a function of the equatorial distance $L = r_e/R_E$. For $\alpha < \alpha_e$(MIN) the electrons are lost in collision with the planet.

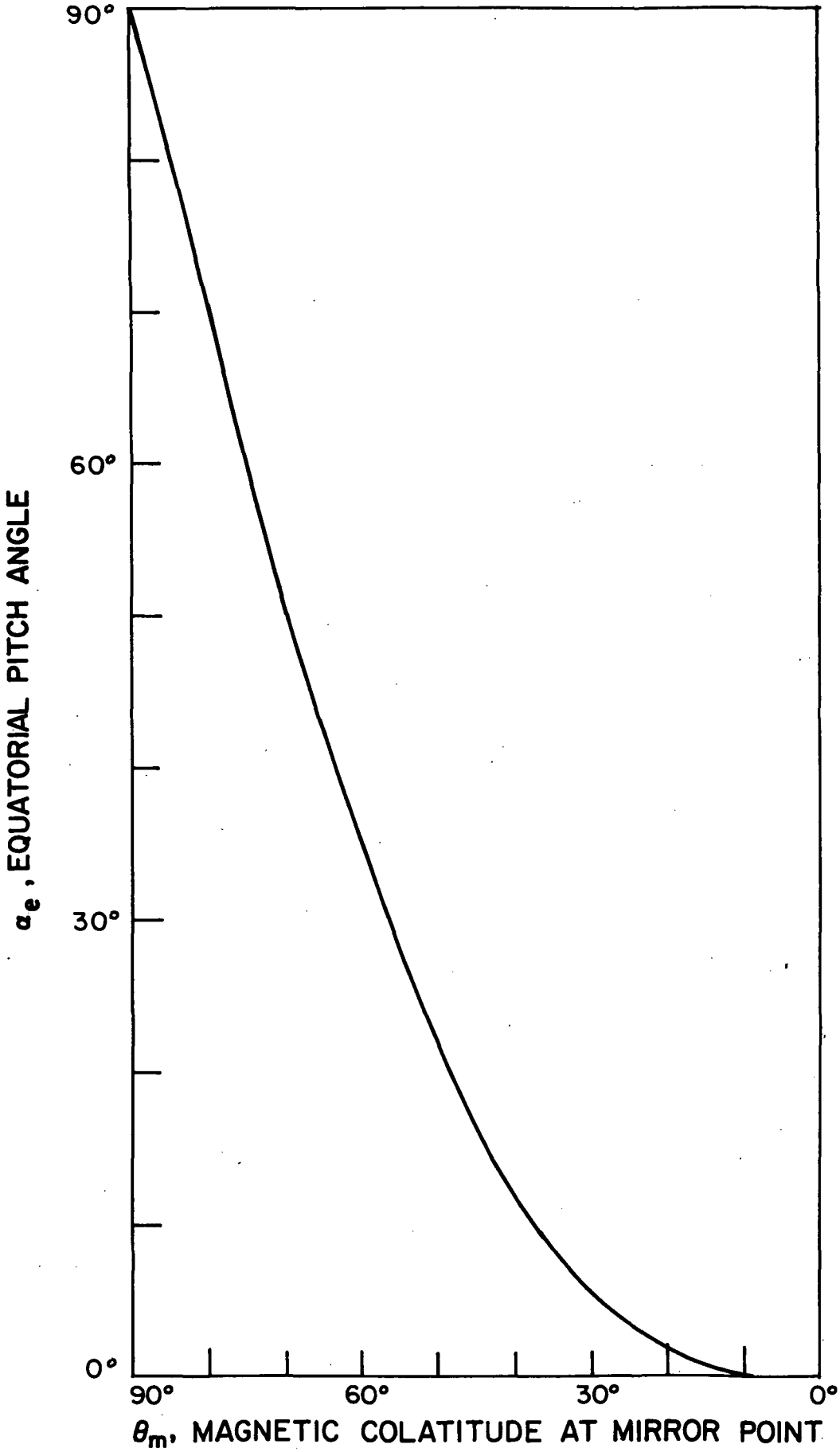

Figure 8. Equatorial pitch angle of the electrons and the corresponding magnetic colatitude (θ_M) of the mirror point.

In order to express the energy dependence of the Stokes parameters, we define the new variable $u' = \sqrt{B_s}\ \varepsilon/\varepsilon_0$, where B_s is the equatorial, surface magnetic field. Making this change of variable in Equation (60) we get

$$n'(u',\alpha_e,\vec{r}_e) = 2\pi\Gamma(\alpha_e)\ \sin\alpha_e\ A'(u')\ N(r_e)\ , \tag{61}$$

where Γ, N are the distribution functions defined above; and A', n' become the corresponding density functions for electrons with energy $u'/\sqrt{B_s}$ in the range $u'/\sqrt{B_s}$ to $u'/\sqrt{B_s} + 1/\sqrt{B_s}\ du'$.

Making the change of variable described in Equation (61), we substitute Equation (59) into (13) to obtain the expression for the intensity from the elemental volume dv [See Equation (35)]:

$$I_{f_{\theta,\phi}}(u',r_e) = \left[\frac{\sqrt{3}}{2}\,\mu e^2 c\left(\frac{eB_s R_E^3}{2\pi m}\right) A'(u')\ \frac{N(r_e)}{r_e}\,dr_e\right] \left[\frac{(1+3\cos^2\theta)^{3/4}}{\sin^2\theta}\ x\ \Gamma(\tilde{\omega}_e)(\sin^{-1}\tilde{\omega})\ F(f/f_c)\right] d\theta d\phi\ . \tag{62}$$

Similarly, the other Stokes parameters can be derived by combining Equations (14) and (15) with Equations (6) to (8):

$$Q_{f_{\theta,\phi}}(u',r_e) = \left[\frac{\sqrt{3}}{2}\,\mu e^2 c\left(\frac{eB_s R_E^3}{2\pi m}\right) A'(u')\ \frac{N(r_e)}{r_e}\,dr_e\right] \left[\frac{(1+3\cos^2\theta)^{3/4}}{\sin^2\theta}\ x\ \Gamma(\tilde{\omega}_e)(\sin^{-1}\tilde{\omega})\ F_p(f/f_c)\cos 2\chi\right] d\theta d\phi\ , \tag{63}$$

$$U_{f_{\theta,\phi}}(u',r_e) = \left[\frac{\sqrt{3}}{2}\,\mu e^2 c\left(\frac{eB_s R_E^3}{2\pi m}\right) A'(u')\,\frac{N(r_e)}{r_e}\,dr_e\right]$$

$$\left[\frac{(1+3\cos^2\theta)^{3/4}}{\sin^2\theta} \times \Gamma(\tilde{\omega}_e)(\sin^{-1}\tilde{\omega})\,F_p(f/f_c)\,\sin 2\chi\right] d\theta d\phi\ , \tag{64}$$

and

$$V_{f_{\theta,\phi}}(u',r_e) = \left[\sqrt{2}\,\mu e^2 c\,\left(\frac{eB_s R_E^3}{2\pi m}\right)^{3/2} A'(u')\,\frac{N(r_e)}{r_e^{5/2}}\,dr_e\right]$$

$$\left\{\frac{(1+3\cos^2\theta)^{3/4}}{\sin^2\theta} \times \Gamma(\tilde{\omega}_e)\cot\tilde{\omega}\,(\sin^{-1/2}\tilde{\omega})\,f^{-1/2}\right\}$$

$$\left\{(f/f_c)^{1/2}\,F_s(f/f_c) + \left(2 + \frac{\Gamma'(\tilde{\omega})}{\Gamma(\tilde{\omega})}\tan\tilde{\omega}\right)(f/f_c)^{-1/2}\right.$$

$$\left.\times\,[F_p(f/f_c) - \tfrac{1}{2}F(f/f_c)]\right\}\ . \tag{65}$$

where in M.K.S. units

$e = 1.60207 \times 10^{-19}$,

$m = 9.1084 \times 10^{-31}$,

$\mu = 4\pi \times 10^{-7}$

$R_E = 7.085 \times 10^7$ m (Dollfus, 1970) is the Jovian equatorial radius,

r_e is the equatorial distance of the dipolar shell,

$N(r_e)$ is the equatorial number density of electrons at r_e,

$A'(u')$ and $\Gamma(\tilde{\omega})$ are normalized density functions in the equatorial plane at r_e,

$\sin\tilde{\omega}$, $\cos 2\chi$, $\sin 2\chi$ are given by Equations (30), (33)and (34),

F, F_p, F_s are the emissivity-polarization functions defined in Equations (18) to (20) and plotted in Figure 2.

TABLE 3

CONVERSION OF THE VARIABLE $x = f/f_c$ INTO THE ENERGY-DEPENDENT VARIABLE u FOR THE CASE $\theta = \tilde{\omega}_e = 90^\circ$

$$u = \frac{1}{3/2\ \frac{e}{2\pi m}} * \frac{1}{x} \quad \text{[See Equation (67)]}$$

x	u
0.0010	15.432
0.0015	12.600
0.0020	10.912
0.0030	8.910
0.0040	7.716
0.0050	6.901
0.0060	6.300
0.0070	5.833
0.0080	5.456
0.0090	5.144
0.0100	4.880
0.0150	3.985
0.0200	3.451
0.0300	2.818
0.0400	2.440
0.0500	2.182
0.0600	1.992
0.0700	1.844
0.0800	1.725
0.0900	1.627
0.1000	1.543
0.1500	1.260
0.2000	1.091
0.3000	0.891
0.4000	0.772
0.5000	0.690
0.6000	0.630
0.7000	0.583
0.8000	0.546
0.9000	0.514
1.0000	0.488
1.5000	0.398
2.0000	0.345
3.0000	0.282
4.0000	0.244
5.0000	0.218
6.0000	0.199
7.0000	0.184
8.0000	0.173
9.0000	0.163
10.0000	0.154
20.0000	0.109
30.0000	0.089
40.0000	0.077
50.0000	0.069
60.0000	0.063
70.0000	0.058
80.0000	0.055
90.0000	0.051

We also need the expression for the critical frequency, f_c, which we get by combining Equations (16), (17), (28), and (58).

$$f_c = \frac{3}{2}\left(\frac{e}{2\pi m}\right) u'^2 \left(\frac{R_E}{r_e}\right)^3 \left[\frac{(1 + 3\cos^2\theta)^{3/4}}{\sin^9\theta} \sin\tilde{\omega}_e\right] , \qquad (66)$$

where $\tilde{\omega}_e$ is the equatorial angle between the field direction and the line of sight $\hat{n}$.

From Equation (66) we obtain the following expression for the argument of the emissivity-polarization functions $x = f/f_c$ computed at the volume element dv,

$$x_{f_{\theta,\phi}}(u) = \left[\frac{1}{3/2\ \frac{e}{2\pi m}}\right] \frac{1}{u^2} \left[\frac{\sin^9\theta}{(1 + 3\cos^2\theta)^{3/4} \sin\tilde{\omega}_e}\right] , \qquad (67)$$

where we define $u = \frac{1}{f^{1/2}} \left(\frac{R_E}{r_e}\right)^{3/2} u'$.

G. Equatorial Pitch Angle Distributions

The distribution of electrons in pitch angle at the equator can be written in the form

$$\Gamma(\alpha_e) = K_q \sin^q \alpha_e , \qquad (68)$$

where K_q is a normalization constant such that

$$K_q \int_{\alpha_e(MIN)}^{\pi} (\sin^q \alpha_e) 2\pi \sin\alpha_e \, d\alpha_e = 1 , \qquad (69)$$

and q measures the degree of anisotropy.

A realistic model of the radiation belts of Jupiter must take into account the variation in pitch-angle distribution with shell distance r_e. Such a variation is needed on the basis of theoretical considerations of the Jovian field and experimental observations of the Earth's radiation belts, both of which are elaborated later.

The Stokes parameters in Equations (62) to (65) have been computed for two types of distributions of electron pitch angles. One is isotropic given by q = 0, with a cutoff at α_e(MIN); the other is sharply confined to the equatorial plane with q = 60.(*)

From Equation (69) the normalization constants for such distributions are $K_{q=0} = 1/(4\pi \cos \alpha_e \text{ (MIN)})$ and $K_{q=60} = 0.498$. Then we may substitute Equation (68) into Equations (62) to (65) and compute the Stokes parameters separately for these two distributions. In order to represent the number density of the particles in these equations, we define a quantity NQ, which is a measure of the ratio of the number of particles with q = 60 to that number for which q = 0. The densities for the isotropic and non-isotropic cases, respectively, can then be written as follows:

$$N(r_e)m_0 = N(r_e)\left[\frac{1}{1 + NQ}\right] , \tag{70}$$

and

$$N(r_e)m_{60} = N(r_e)\left[\frac{NQ}{1 + NQ}\right] . \tag{71}$$

H. The Integrated Stokes Parameters for a Shell at Distance $L = r_e/R_E$

By combining Equations (29) to (34) and (68) with Equations (62) to (65) we write the expression for the Stokes parameters as a function of u

(*) This particular value is chosen since, as shown in Chapter III, Section B, it provides for a sufficient range in the variability of the intensity with rotation of the planet to account for the observations.

from a cell 2^o x 2^o in longitude and latitude (ϕ - θ coordinates in Figure 3) located in a shell with equatorial distance L. They are expressed in flux units received from Jupiter at a frequency f(MHz). The distance to Jupiter is normalized to 4.04 A.U. such that the planet subtends a polar semi-diameter of 22.75".

$$I_{f_{\theta,\phi}}(u,L) = K_1 K_q \sin^{-2}\theta\, h^{5/4}\sigma^{-1/2} \sin^q \tilde{\omega}_e\, F(x) \ , \tag{72}$$

$$Q_{f_{\theta,\phi}}(u,L) = K_1 K_q \sin^{-2}\theta\, h^{5/4}\sigma^{-1/2} \sin^q \tilde{\omega}_e\, F_p(x) \cos 2\chi \ , \tag{73}$$

$$U_{f_{\theta,\phi}}(u,L) = K_1 K_q \sin^{-2}\theta\, h^{5/4}\sigma^{-1/2} \sin^q \tilde{\omega}_e\, F_p(x) \sin 2\chi \ , \tag{74}$$

and $$V_{f_{\theta,\phi}}(u,L) = K_2 K_q \sin^{-5}\theta\, h^{5/4}\sigma^{-3/4}\rho_f^{-1/2}$$

$$\left\{ x^{1/2} F_s(x) + \left(2 + \frac{\Gamma'(\tilde{\omega})}{\Gamma(\tilde{\omega})} \tan \tilde{\omega} \right) x^{-1/2} \left[F_p(x) - \frac{1}{2} F(x) \right] \right\} . \tag{75}$$

where $L = r_e/R_E$,

$K_1 = 0.72768 \times 10^{-4} B_s A'(u') N(r_e) dr_e/r_e$,

$K_2 = 0.11883 \times 10^{-3} f^{-1/2} B_s^{3/2} A'(u') N(r_e) dr_e/r_e^{5/2}$,

B_s is the surface magnetic field at the equator in Gauss,

N is the number density at the equator in cm^{-3} ,

A' is the normalized function of $u' = \sqrt{B_s}\, \varepsilon/\varepsilon_0$,

$K_0(L) = 1/[4\pi \cos \alpha\ (MIN)]$ for an isotropic distribution,

$K_{60} = 0.49794$ for a distribution confined to the magnetic equator,

h, ρ, σ, $\sin \tilde{\omega}_e$, $\cos 2\chi$, $\sin 2\chi$ are given by Equations (29) to (34),

F, F_p, F_s are the emissivity-polarization functions given by Equations (18) to (20), and

$x = x_{f_{\theta,\phi}}(u)$ as defined in Equation (67).

The IBM 360/75 computer at the University of Illinois was used to calculate the Stokes parameters integrated over a shell at L as a function of the energy-dependent argument u. The integration was performed by subdividing each shell into 2^o x 2^o cells hereafter called "source points". The position of the planet in the magnetosphere (MC system) was accounted for through Equation (49). It may be shown that the Stokes parameters are symmetric in the ϕ-plane, i.e., $I(\phi) = I(-\phi)$ and similarly for Q, U, and V. In the θ-plane we obtain the following relations: $I(\theta) = I(-\theta)$, $Q(\theta) = Q(-\theta)$, $U(\theta) = -U(\theta)$ and $V(\theta) = -V(\theta)$. Also, at the rotational angles $\Omega = 0^o$ and $\Omega = 180^o$ (in the system defined in Section D), we have complete symmetry in the ϕ-plane and integration need be performed only in the range $0^o \leq \phi \leq 180^o$. However, when $\Omega = 45^o$, 90^o, and 135^o the integration must be performed in the full range of $0^o \leq \phi \leq 360^o$ because of the asymmetric position of the planet in the magnetosphere at these rotation angles.

In calculating the Stokes parameters for an isotropic distribution of electrons, the emission from all points in a shell requiring particles with an equatorial pitch angle $\alpha_e < \alpha_e(MIN)$ were rejected. The equatorial

pitch angle α_e of a particle at position θ,ϕ, whose radiation is detected by the observer at $\hat{n}$, can be obtained by combining Equations (30) and (58),

$$\sin \alpha_e = \frac{\sin^3 \theta}{h^{1/4}} \sqrt{\frac{\sigma}{h}} \quad . \tag{76}$$

α_e(MIN) is determined by the surface of the planet which falls at a different position along the field line for each shell distance L as shown in Figure 7.

For the distribution of electrons limited to the equatorial plane ($K_{60} \sin^{60} \alpha_e$), the emission is strongly confined to that plane and the integration is complete within 30° of the magnetic equator. These solutions are denoted by the subscript 60.

In the absence of the planet, integration over a shell yields $U = V = 0$ (as can be seen from the symmetry relations described above). In the presence of an eclipse of the source by the planet we get $U \neq 0$. It becomes immediately obvious that V is much smaller than U or Q and will be neglected.

For rotational angles $\Omega = 45^\circ$, 90°, and 135° the integration was performed separately for the quadrants $0 \leq \phi \leq 180^\circ$ (component 1) and $180^\circ \leq \phi \leq 360^\circ$ (component 2). These correspond to the west and east components, respectively, of projected maps of the radiation belts (Berge, 1966; Branson, 1968; Gulkis, 1970).

Table 4 shows the effect of the planetary rotation on the eclipse of the source. Evidently it increases gradually from $\Omega = 0^\circ$ (when the zenomagnetic colatitude of the Earth, $\theta_0 = 77^\circ$) to $\Omega = 180^\circ$ (when $\theta_0 = 97^\circ$). The eclipse by the planet was included for shells up to a distance of L = 3.0. Beyond this point it was neglected and the error involved is

TABLE 4

NUMBER OF $2^{\circ} \times 2^{\circ}$ CELLS ECLIPSED BY THE PLANET AS FUNCTION OF THE ROTATIONAL ANGLE Ω AND SHELL DISTANCE L

L	$\Omega = 0^{\circ}$	$\Omega = 45^{\circ}$	$\Omega = 90^{\circ}$	$\Omega = 135^{\circ}$	$\Omega = 180^{\circ}$
1.1	648	736	865	973	1048
1.3	410	477	572	650	708
1.5	316	375	460	513	566
1.7	258	312	384	430	476
1.9	214	267	334	370	410
2.1	186	234	297	325	362
2.3	160	207	265	286	324
2.5	136	182	239	254	292
2.7	120	163	218	229	262
2.9	102	153	199	208	234

less than 10 percent as can be seen by comparison of the results in Tables 5 and 6 for the integrated Stokes parameters without and with the planet. These were computed for an isotropic distribution of electrons and $\Omega = 0^{o}$.

1. The isotropic case

The Stokes parameters shown in Tables 5 and 6 are computed for representative values of u. As mentioned previously, U = 0 in the absence of the planet (Table 5) but in the presence of the planet (Table 6) $U \neq 0$ and in fact it is comparable to and larger than Q at some particular values of L (See Figure 13). It can be seen that at L = 3 the uneclipsed values are within 10 percent of the eclipsed ones and that the eclipse effect decreases with increasing L. Therefore the values for the Stokes parameters have been taken from Table 6 out to L = 3 and from Table 5 beyond. As will be seen later, the best-fitting distribution of electrons in the radiation belts falls rapidly for L > 3, so that the overall approximation is better than 10 percent.

The function I(u,L) is shown in Figure 9. The behavior is smooth with a peak near u = 0.7, which corresponds to x = 0.5 (See Table 3), and thus, is similar in shape to the emissivity-polarization function F(x). The function $\sqrt{Q^2(u,L) + U^2(u,L)}$ was computed and is shown in Figure 10. There is a transition phase in the range L = 1.1 to 1.6 in which the polarized intensity gradually diminishes and its maximum is displaced towards a smaller u. At L > 1.6 the polarized intensity rises again with increasing L and peaks at a nearly constant value of u.

According to Equation (9) the quantity $\sqrt{Q^2(u,L) + U^2(u,L)}/I(u,L)$ is the degree of polarization for a given u at the shell distance L. Thus for a given u we may plot the degree of polarization of the synchrotron

TABLE 5. STOKES PARAMETERS AS FUNCTION OF u AND L FOR THE NON-ECLIPSED CASE (U = 0). PITCH ANGLE DISTRIBUTION IS ISOTROPIC. $\Omega = 0^{o}$

L \ u	.1		.5		1.0		1.5		2.0	
	I	Q	I	Q	I	Q	I	Q	I	Q
1.1	0.0	0.0	0.14131E 00	0.75445E-01	0.18323E 00	-0.84584E-01	0.16440E 00	0.70515E-01	0.14476E 00	0.59628E-01
1.2	0.0	0.0	0.21936E 00	0.81025E-01	0.27298E 00	0.93658E-01	0.24302E 00	0.78393E-01	0.21370E 00	0.66426E-01
1.3	0.12391E-04	-0.10209E-04	0.29334E 00	0.69851E-01	0.35138E 00	0.87852E-01	0.31064E 00	0.74333E-01	0.27265E 00	0.63111E-01
1.4	0.97191E-04	-0.84943E-04	0.36286E 00	0.50678E-01	0.42162E 00	0.75644E-01	0.37052E 00	0.65256E-01	0.32494E 00	0.55489E-01
1.5	0.63032E-03	-0.56363E-03	0.43512E 00	0.22849E-01	0.49113E 00	0.56974E-01	0.42899E 00	0.51241E-01	0.37461E 00	0.44353E-01
1.6	0.18318E-02	-0.16111E-02	0.50357E 00	-0.56428E-02	0.55398E 00	0.37104E-01	0.48193E 00	0.35733E-01	0.41974E 00	0.31769E-01
1.7	0.44072E-02	-0.37432E-02	0.57326E 00	-0.31694E-01	0.61775E 00	0.20953E-01	0.53493E 00	0.23901E-01	0.46563E 00	0.21983E-01
1.8	0.90858E-02	-0.73449E-02	0.63960E 00	-0.62172E-01	0.67601E 00	-0.95717E-03	0.58291E 00	0.70399E-02	0.50673E 00	0.79789E-02
1.9	0.17128E-01	-0.12956E-01	0.70927E 00	-0.88037E-01	0.73642E 00	-0.17613E-01	0.63263E 00	-0.54074E-02	0.54946E 00	-0.23226E-02
2.0	0.26987E-01	-0.19239E-01	0.77311E 00	-0.11371E 00	0.79144E 00	-0.34652E-01	0.67778E 00	-0.18171E-01	0.58843E 00	-0.12957E-01
2.1	0.38199E-01	-0.25787E-01	0.83800E 00	-0.13954E 00	0.84636E 00	-0.53151E-01	0.72308E 00	-0.32566E-01	0.62662E 00	-0.24761E-01
2.2	0.59266E-01	-0.36548E-01	0.91057E 00	-0.16167E 00	0.90659E 00	-0.67866E-01	0.77334E 00	-0.44135E-01	0.66942E 00	-0.34247E-01
2.3	0.71614E-01	-0.42063E-01	0.96719E 00	-0.17990E 00	0.95350E 00	-0.79545E-01	0.81233E 00	-0.52987E-01	0.70304E 00	-0.41613E-01
2.4	0.10392E 00	-0.54918E-01	0.10445E 01	-0.20006E 00	0.10164E 01	-0.93124E-01	0.86414E 00	-0.63464E-01	0.74734E 00	-0.50342E-01
2.5	0.12065E 00	-0.59544E-01	0.11054E 01	-0.21337E 00	0.10680E 01	-0.10345E 00	0.90681E 00	-0.71618E-01	0.78429E 00	-0.57260E-01
2.6	0.16589E 00	-0.72742E-01	0.11774E 01	-0.22641E 00	0.11236E 01	-0.11165E 00	0.95126E 00	-0.77773E-01	0.82195E 00	-0.62350E-01
2.7	0.19058E 00	-0.76801E-01	0.12355E 01	-0.23487E 00	0.11718E 01	-0.11850E 00	0.99108E 00	-0.83266E-01	0.85588E 00	-0.66916E-01
2.8	0.24085E 00	-0.84493E-01	0.13064E 01	-0.24185E 00	0.12273E 01	-0.12365E 00	0.10368E 01	-0.87354E-01	0.89272E 00	-0.69953E-01
2.9	0.27742E 00	-0.87435E-01	0.13547E 01	-0.24832E 00	0.12666E 01	-0.12851E 00	0.10699E 01	-0.91103E-01	0.92083E 00	-0.72973E-01
3.0	0.30623E 00	-0.87718E-01	0.14126E 01	-0.25127E 00	0.13154E 01	-0.13016E 00	0.11109E 01	-0.92080E-01	0.95638E 00	-0.73764E-01
3.1	0.36986E 00	-0.90701E-01	0.14727E 01	-0.25327E 00	0.13596E 01	-0.13072E 00	0.11472E 01	-0.92492E-01	0.98704E 00	-0.74042E-01
3.2	0.40754E 00	-0.92116E-01	0.15151E 01	-0.26111E 00	0.13916E 01	-0.13729E 00	0.11733E 01	-0.97831E-01	0.10089E 01	-0.78400E-01
3.3	0.45004E 00	-0.85724E-01	0.15778E 01	-0.25977E 00	0.14418E 01	-0.13789E 00	0.12136E 01	-0.98658E-01	0.10434E 01	-0.79053E-01
3.4	0.50394E 00	-0.87094E-01	0.16187E 01	-0.26520E 00	0.14725E 01	-0.14199E 00	0.12373E 01	-0.10180E 00	0.10640E 01	-0.81825E-01
3.5	0.56347E 00	-0.85067E-01	0.16682E 01	-0.26901E 00	0.15086E 01	-0.14463E 00	0.12651E 01	-0.10392E 00	0.10878E 01	-0.83527E-01
3.6	0.60165E 00	-0.81196E-01	0.16964E 01	-0.27042E 00	0.15306E 01	-0.14710E 00	0.12825E 01	-0.10622E 00	0.11030E 01	-0.85538E-01
3.7	0.64173E 00	-0.74579E-01	0.17605E 01	-0.26902E 00	0.15873E 01	-0.14731E 00	0.13301E 01	-0.10680E 00	0.11443E 01	-0.86061E-01
3.8	0.70033E 00	-0.68530E-01	0.18002E 01	-0.26766E 00	0.16161E 01	-0.14567E 00	0.13535E 01	-0.10528E 00	0.11633E 01	-0.84854E-01
3.9	0.76847E 00	-0.60999E-01	0.18504E 01	-0.26968E 00	0.16540E 01	-0.14680E 00	0.13838E 01	-0.10603E 00	0.11885E 01	-0.85496E-01
4.0	0.81030E 00	-0.57988E-01	0.18840E 01	-0.26915E 00	0.16806E 01	-0.14530E 00	0.14067E 01	-0.10451E 00	0.12083E 01	-0.84091E-01
4.1	0.84639E 00	-0.53096E-01	0.19128E 01	-0.26953E 00	0.17026E 01	-0.14723E 00	0.14248E 01	-0.10638E 00	0.12240E 01	-0.85748E-01
4.2	0.89658E 00	-0.35003E-01	0.19700E 01	-0.25801E 00	0.17501E 01	-0.14140E 00	0.14647E 01	-0.10223E 00	0.12581E 01	-0.82524E-01
4.3	0.95103E 00	-0.26893E-01	0.20185E 01	-0.26060E 00	0.17884E 01	-0.14263E 00	0.14974E 01	-0.10262E 00	0.12861E 01	-0.82574E-01
4.4	0.10195E 01	-0.19559E-01	0.20585E 01	-0.25777E 00	0.18144E 01	-0.14002E 00	0.15192E 01	-0.10010E 00	0.13051E 01	-0.80282E-01
4.5	0.10657E 01	-0.11754E-01	0.20900E 01	-0.25672E 00	0.18355E 01	-0.13978E 00	0.15359E 01	-0.99865E-01	0.13192E 01	-0.80031E-01
4.6	0.11142E 01	0.40092E-03	0.21279E 01	-0.25272E 00	0.18621E 01	-0.13715E 00	0.15564E 01	-0.98019E-01	0.13363E 01	-0.78548E-01
4.7	0.11681E 01	0.18979E-01	0.21737E 01	-0.24874E 00	0.18991E 01	-0.13535E 00	0.15855E 01	-0.97018E-01	0.13610E 01	-0.77627E-01
4.8	0.11914E 01	0.23504E-01	0.21892E 01	-0.24640E 00	0.19127E 01	-0.13563E 00	0.15975E 01	-0.97904E-01	0.13718E 01	-0.78602E-01
4.9	0.12134E 01	0.29019E-01	0.22250E 01	-0.24508E 00	0.19390E 01	-0.13536E 00	0.16181E 01	-0.97678E-01	0.13896E 01	-0.78545E-01
5.0	0.13234E 01	0.57932E-01	0.23005E 01	-0.22261E 00	0.20016E 01	-0.12083E 00	0.16705E 01	-0.86952E-01	0.14340E 01	-0.69968E-01
5.1	0.13850E 01	0.73795E-01	0.23295E 01	-0.21597E 00	0.20204E 01	-0.11661E 00	0.16846E 01	-0.83795E-01	0.14454E 01	-0.67449E-01
5.2	0.14273E 01	0.87604E-01	0.23482E 01	-0.21073E 00	0.20327E 01	-0.11324E 00	0.16937E 01	-0.81291E-01	0.14527E 01	-0.65472E-01
5.3	0.14935E 01	0.11468E 00	0.23911E 01	-0.20343E 00	0.20686E 01	-0.10870E 00	0.17237E 01	-0.77669E-01	0.14784E 01	-0.62465E-01
5.4	0.15171E 01	0.11983E 00	0.24033E 01	-0.20010E 00	0.20783E 01	-0.10555E 00	0.17318E 01	-0.75061E-01	0.14852E 01	-0.60306E-01
5.5	0.15449E 01	0.13081E 00	0.24443E 01	-0.19471E 00	0.21090E 01	-0.10267E 00	0.17570E 01	-0.72688E-01	0.15061E 01	-0.58421E-01
5.6	0.15707E 01	0.13966E 00	0.24565E 01	-0.19114E 00	0.21170E 01	-0.10038E 00	0.17633E 01	-0.70884E-01	0.15112E 01	-0.56993E-01
5.7	0.15928E 01	0.14834E 00	0.24678E 01	-0.18728E 00	0.21238E 01	-0.98100E-01	0.17688E 01	-0.69074E-01	0.15156E 01	-0.55544E-01
5.8	0.16938E 01	0.17247E 00	0.25062E 01	-0.17901E 00	0.21492E 01	-0.92717E-01	0.17889E 01	-0.64802E-01	0.15302E 01	-0.52444E-01
5.9	0.17407E 01	0.18718E 00	0.25243E 01	-0.17410E 00	0.21651E 01	-0.91008E-01	0.18044E 01	-0.64249E-01	0.15440E 01	-0.52392E-01
6.0	0.18052E 01	0.21220E 00	0.25494E 01	-0.16547E 00	0.21815E 01	-0.85422E-01	0.18175E 01	-0.59802E-01	0.15553E 01	-0.48558E-01

TABLE 5. (Continued)

L/u	3.0		4.0		5.0		7.0		10.0	
	I	Q	I	Q	I	Q	I	Q	I	Q
1.1	0.11772E 00	0.46909E-01	0.94315E-01	0.37591E-01	0.86411E-01	0.33167E-01	0.69940E-01	0.26518E-01	0.54692E-01	0.20321E-01
1.2	0.17264E 00	0.52161E-01	0.14231E 00	0.41990E-01	0.12686E 00	0.36850E-01	0.10271E 00	0.29564E-01	0.80520E-01	0.22909E-01
1.3	0.21990E 00	0.49874E-01	0.18150E 00	0.39937E-01	0.16120E 00	0.34999E-01	0.13059E 00	0.28162E-01	0.10248E 00	0.21927E-01
1.4	0.25975E 00	0.44286E-01	0.21593E 00	0.35314E-01	0.19126E 00	0.30861E-01	0.15492E 00	0.24990E-01	0.12181E 00	0.19448E-01
1.5	0.29975E 00	0.35581E-01	0.24968E 00	0.27975E-01	0.22022E 00	0.24507E-01	0.17830E 00	0.20108E-01	0.14051E 00	0.15490E-01
1.6	0.33513E 00	0.26026E-01	0.27924E 00	0.20077E-01	0.24642E 00	0.17374E-01	0.19919E 00	0.14648E-01	0.15718E 00	0.11173E-01
1.7	0.37205E 00	0.18266E-01	0.30998E 00	0.13582E-01	0.27265E 00	0.11868E-01	0.22077E 00	0.10317E-01	0.17414E 00	0.78309E-02
1.8	0.40419E 00	0.77429E-02	0.33708E 00	0.47345E-02	0.29552E 00	0.44500E-02	0.23955E 00	0.42886E-02	0.18919E 00	0.30134E-02
1.9	0.43762E 00	-0.42822E-04	0.36486E 00	-0.17679E-02	0.32000E 00	-0.13688E-02	0.25918E 00	-0.10668E-03	0.20483E 00	-0.47466E-03
2.0	0.46849E 00	-0.82596E-02	0.39029E 00	-0.84915E-02	0.34243E 00	-0.70715E-02	0.27730E 00	-0.48041E-02	0.21913E 00	-0.41004E-02
2.1	0.49866E 00	-0.17338E-01	0.41543E 00	-0.16001E-01	0.36401E 00	-0.13421E-01	0.29485E 00	-0.99366E-02	0.23315E 00	-0.81788E-02
2.2	0.53188E 00	-0.24467E-01	0.44314E 00	-0.21994E-01	0.38838E 00	-0.18609E-01	0.31464E 00	-0.14092E-01	0.24850E 00	-0.11339E-01
2.3	0.55849E 00	-0.30080E-01	0.46525E 00	-0.26532E-01	0.40786E 00	-0.22594E-01	0.33016E 00	-0.17277E-01	0.26057E 00	-0.13807E-01
2.4	0.59281E 00	-0.36550E-01	0.49404E 00	-0.31949E-01	0.43269E 00	-0.27150E-01	0.35025E 00	-0.20989E-01	0.27649E 00	-0.16709E-01
2.5	0.62161E 00	-0.41814E-01	0.51777E 00	-0.36227E-01	0.45335E 00	-0.30828E-01	0.36686E 00	-0.23943E-01	0.28963E 00	-0.19025E-01
2.6	0.65089E 00	-0.45736E-01	0.54233E 00	-0.39560E-01	0.47444E 00	-0.33566E-01	0.38412E 00	-0.26186E-01	0.30348E 00	-0.20804E-01
2.7	0.67715E 00	-0.49218E-01	0.56451E 00	-0.42417E-01	0.49376E 00	-0.36079E-01	0.39996E 00	-0.28258E-01	0.31597E 00	-0.22390E-01
2.8	0.70664E 00	-0.51654E-01	0.58946E 00	-0.44587E-01	0.51525E 00	-0.37811E-01	0.41728E 00	-0.29669E-01	0.33030E 00	-0.23610E-01
2.9	0.72906E 00	-0.53937E-01	0.60803E 00	-0.46542E-01	0.53116E 00	-0.39410E-01	0.43018E 00	-0.31010E-01	0.34079E 00	-0.24712E-01
3.0	0.75705E 00	-0.54552E-01	0.63128E 00	-0.46963E-01	0.55127E 00	-0.39691E-01	0.44618E 00	-0.31317E-01	0.35392E 00	-0.24935E-01
3.1	0.78049E 00	-0.54853E-01	0.65091E 00	-0.47232E-01	0.56868E 00	-0.39881E-01	0.45979E 00	-0.31437E-01	0.36166E 00	-0.24702E-01
3.2	0.79770E 00	-0.54255E-01	0.66541E 00	-0.50129E-01	0.58135E 00	-0.42366E-01	0.46969E 00	-0.33443E-01	0.36784E 00	-0.26128E-01
3.3	0.82457E 00	-0.58849E-01	0.68792E 00	-0.50568E-01	0.60093E 00	-0.42727E-01	0.48557E 00	-0.33706E-01	0.37889E 00	-0.26389E-01
3.4	0.84055E 00	-0.60870E-01	0.70166E 00	-0.52282E-01	0.61243E 00	-0.44162E-01	0.49556E 00	-0.34933E-01	0.38272E 00	-0.27390E-01
3.5	0.85896E 00	-0.62162E-01	0.71717E 00	-0.53417E-01	0.62556E 00	-0.45082E-01	0.50689E 00	-0.35681E-01	0.38896E 00	-0.27841E-01
3.6	0.87117E 00	-0.63646E-01	0.72710E 00	-0.54570E-01	0.63408E 00	-0.46207E-01	0.51418E 00	-0.36529E-01	0.39312E 00	-0.28544E-01
3.7	0.90412E 00	-0.64106E-01	0.75453E 00	-0.55042E-01	0.65786E 00	-0.46547E-01	0.53365E 00	-0.36735E-01	0.40716E 00	-0.28871E-01
3.8	0.91878E 00	-0.63296E-01	0.76638E 00	-0.54424E-01	0.66832E 00	-0.45979E-01	0.54039E 00	-0.36183E-01	0.41044E 00	-0.28923E-01
3.9	0.93810E 00	-0.63686E-01	0.78188E 00	-0.54977E-01	0.68249E 00	-0.46426E-01	0.54820E 00	-0.36551E-01	0.41519E 00	-0.29637E-01
4.0	0.95337E 00	-0.62564E-01	0.79425E 00	-0.54070E-01	0.69396E 00	-0.45571E-01	0.55522E 00	-0.36103E-01	0.42023E 00	-0.29333E-01
4.1	0.96591E 00	-0.63921E-01	0.80435E 00	-0.55292E-01	0.70293E 00	-0.46488E-01	0.56036E 00	-0.37202E-01	0.42403E 00	-0.30236E-01
4.2	0.99306E 00	-0.61452E-01	0.82677E 00	-0.53226E-01	0.72246E 00	-0.44732E-01	0.57360E 00	-0.36580E-01	0.43423E 00	-0.29786E-01
4.3	0.10157E 01	-0.61336E-01	0.84579E 00	-0.53106E-01	0.73922E 00	-0.44609E-01	0.58450E 00	-0.36759E-01	0.44172E 00	-0.30178E-01
4.4	0.10308E 01	-0.59481E-01	0.85824E 00	-0.51607E-01	0.75080E 00	-0.43243E-01	0.59311E 00	-0.35084E-01	0.44461E 00	-0.29674E-01
4.5	0.10418E 01	-0.59311E-01	0.86739E 00	-0.51446E-01	0.75899E 00	-0.43014E-01	0.59320E 00	-0.34413E-01	0.44695E 00	-0.29964E-01
4.6	0.10549E 01	-0.58123E-01	0.87830E 00	-0.50487E-01	0.76895E 00	-0.42093E-01	0.59860E 00	-0.34263E-01	0.45029E 00	-0.29950E-01
4.7	0.10742E 01	-0.57312E-01	0.89415E 00	-0.49981E-01	0.78340E 00	-0.41457E-01	0.60742E 00	-0.34993E-01	0.45607E 00	-0.30496E-01
4.8	0.10833E 01	-0.58124E-01	0.90175E 00	-0.50697E-01	0.78999E 00	-0.42074E-01	0.61260E 00	-0.35472E-01	0.45948E 00	-0.30974E-01
4.9	0.10970E 01	-0.57941E-01	0.91298E 00	-0.50604E-01	0.79998E 00	-0.41985E-01	0.61994E 00	-0.35393E-01	0.46507E 00	-0.30988E-01
5.0	0.11329E 01	-0.51381E-01	0.94486E 00	-0.44926E-01	0.82006E 00	-0.38252E-01	0.63505E 00	-0.34391E-01	0.47687E 00	-0.28884E-01
5.1	0.11420E 01	-0.49371E-01	0.95317E 00	-0.42989E-01	0.82312E 00	-0.37526E-01	0.63700E 00	-0.33854E-01	0.47782E 00	-0.28569E-01
5.2	0.11478E 01	-0.47790E-01	0.95860E 00	-0.41496E-01	0.82461E 00	-0.37159E-01	0.63793E 00	-0.33586E-01	0.47829E 00	-0.28409E-01
5.3	0.11675E 01	-0.45686E-01	0.97586E 00	-0.39275E-01	0.83509E 00	-0.37043E-01	0.64594E 00	-0.33492E-01	0.48429E 00	-0.28537E-01
5.4	0.11727E 01	-0.44051E-01	0.98040E 00	-0.37864E-01	0.83788E 00	-0.35987E-01	0.64762E 00	-0.32727E-01	0.48524E 00	-0.28053E-01
5.5	0.11886E 01	-0.42558E-01	0.99373E 00	-0.36740E-01	0.84871E 00	-0.35136E-01	0.65612E 00	-0.32039E-01	0.49148E 00	-0.27637E-01
5.6	0.11924E 01	-0.41492E-01	0.99690E 00	-0.35868E-01	0.85083E 00	-0.34440E-01	0.65714E 00	-0.31646E-01	0.49148E 00	-0.27637E-01
5.7	0.11956E 01	-0.40434E-01	0.99967E 00	-0.34996E-01	0.85265E 00	-0.33721E-01	0.65819E 00	-0.31190E-01	0.49148E 00	-0.27637E-01
5.8	0.12092E 01	-0.37583E-01	0.10017E 01	-0.34481E-01	0.85368E 00	-0.33388E-01	0.65819E 00	-0.31190E-01	0.49148E 00	-0.27637E-01
5.9	0.12215E 01	-0.37503E-01	0.10080E 01	-0.35648E-01	0.85884E 00	-0.34430E-01	0.66202E 00	-0.32175E-01	0.49459E 00	-0.28422E-01
6.0	0.12303E 01	-0.34495E-01	0.10101E 01	-0.34987E-01	0.85992E 00	-0.34007E-01	0.66202E 00	-0.32175E-01	0.49459E 00	-0.28422E-01

TABLE 6. STOKES PARAMETERS AS FUNCTION OF u AND L FOR THE ECLIPSED CASE ($U \neq 0$). PITCH ANGLE DISTRIBUTION IS ISOTROPIC. $\Omega = 0^{\circ}$

I

L \ u	.1	.5	1.0	1.5	2.0
1.10	0.0	0.10618E 00	0.13464E 00	0.12027E 00	0.10583E 00
1.20	0.0	0.17046E 00	0.20581E 00	0.18210E 00	0.15981E 00
1.30	0.90158E-05	0.23626E 00	0.27405E 00	0.24063E 00	0.21073E 00
1.40	0.86423E-04	0.30096E 00	0.33784E 00	0.29464E 00	0.25778E 00
1.50	0.50594E-03	0.36534E 00	0.39845E 00	0.34528E 00	0.30076E 00
1.60	0.15505E-02	0.43271E 00	0.46114E 00	0.39810E 00	0.34571E 00
1.70	0.37838E-02	0.49872E 00	0.52096E 00	0.44769E 00	0.39850E 00
1.80	0.78258E-02	0.56367E 00	0.57899E 00	0.49559E 00	0.42973E 00
1.90	0.14285E-01	0.63024E 00	0.63683E 00	0.54542E 00	0.47257E 00
2.00	0.21938E-01	0.69060E 00	0.69279E 00	0.59012E 00	0.51122E 00
2.10	0.33400E-01	0.75750E 00	0.75120E 00	0.63853E 00	0.55220E 00
2.20	0.50500E-01	0.82570E 00	0.80940E 00	0.68710E 00	0.59380E 00
2.30	0.63200E-01	0.88130E 00	0.85550E 00	0.72540E 00	0.62660E 00
2.40	0.89800E-01	0.95200E 00	0.91370E 00	0.77344E 00	0.66760E 00
2.50	0.10640E-00	0.10105E 01	0.96320E 00	0.81444E 00	0.70310E 00
2.60	0.14218E 00	0.10786E 01	0.10175E 01	0.34182E-02	0.74047E 00
2.70	0.16755E 00	0.11377E 01	0.10659E 01	0.36203E-02	0.77427E 00
2.80	0.20392E 00	0.11980E 01	0.11146E 01	0.83588E-02	0.80727E 00
2.90	0.24105E 00	0.12536E 01	0.11590E 01	0.45981E-02	0.83800E 00
3.00	0.27012E 00	0.13131E 01	0.12099E 01	0.60632E-02	0.87377E 00

Q

L \ u	.1	.5	1.0	1.5	2.0
1.10	0.0	0.53494E-01	0.58766E-01	0.48843E-01	0.41338E-01
1.20	0.0	0.56048E-01	0.63310E-01	0.52796E-01	0.44721E-01
1.30	-0.84373E-05	0.46701E-01	0.58781E-01	0.49025E-01	0.41612E-01
1.40	-0.76227E-04	0.29228E-01	0.46461E-01	0.40283E-01	0.34221E-01
1.50	-0.45270E-03	0.51667E-02	0.29791E-01	0.27644E-01	0.24067E-01
1.60	-0.13699E-02	-0.19675E-01	0.12056E-01	0.14737E-01	0.13705E-01
1.70	-0.32431E-02	-0.43443E-01	-0.21005E-02	0.34108E-02	0.43169E-02
1.80	-0.64186E-02	-0.70484E-01	-0.20556E-01	-0.10584E-01	-0.73527E-02
1.90	-0.11076E-01	-0.92688E-01	-0.33330E-01	-0.19936E-01	-0.15003E-01
2.00	-0.16238E-01	-0.11395E 00	-0.46642E-01	-0.29660E-01	-0.23088E-01
2.10	-0.23361E-01	-0.13831E 00	-0.62269E-01	-0.41476E-01	-0.32666E-01
2.20	-0.32672E-01	-0.15820E 00	-0.74381E-01	-0.50739E-01	-0.40265E-01
2.30	-0.39101E-01	-0.17722E 00	-0.86406E-01	-0.59887E-01	-0.47768E-01
2.40	-0.50727E-01	-0.19760E 00	-0.99800E-01	-0.70173E-01	-0.56310E-01
2.50	-0.56832E-01	-0.21232E 00	-0.10992E 00	-0.78004F-01	-0.62896E-01
2.60	-0.68927E-01	-0.22763E 00	-0.11954E 00	-0.85264E-01	-0.68866E-01
2.70	-0.75730E-01	-0.24048E 00	-0.12888E 00	-0.92546E-01	-0.74917E-01
2.80	-0.83240E-01	-0.25064E 00	-0.13618E 00	-0.98277E-01	-0.79426E-01
2.90	-0.89581E-01	-0.26096E 00	-0.14346E 00	-0.10395E 00	-0.83981E-01
3.00	-0.93620E-01	-0.26771E 00	-0.14776E 00	-0.10711E 00	-0.86604E-01

U

L \ u	.1	.5	1.0	1.5	2.0
1.10	0.0	-0.18055E-02	-0.18412E-02	-0.15108E-02	-0.12703E-02
1.20	0.0	-0.43779E-02	-0.42549E-02	-0.34651E-02	-0.29108E-02
1.30	-0.12136E-05	-0.67438E-02	-0.64567E-02	-0.52518E-02	-0.44176E-02
1.40	-0.15575E-05	-0.73608E-02	-0.72101E-02	-0.58811E-02	-0.49549E-02
1.50	0.93522E-05	-0.82690E-02	-0.85237E-02	-0.70026E-02	-0.59114E-02
1.60	0.65429E-04	-0.82403E-02	-0.92421E-02	-0.76808E-02	-0.64863E-02
1.70	0.22277E-03	-0.74361E-02	-0.94814E-02	-0.80293E-02	-0.68382E-02
1.80	0.57270E-03	-0.64344E-02	-0.97086E-02	-0.83748E-02	-0.71612E-02
1.90	0.15036E-02	-0.40775E-02	-0.93327E-02	-0.83562E-02	-0.72205E-02
2.00	0.26341E-02	-0.12696E-02	-0.82363E-02	-0.77348E-02	-0.67344E-02
2.10	0.31402E-02	0.11274E-02	-0.71053E-02	-0.69235E-02	-0.61398E-02
2.20	0.59157E-02	0.54844E-02	-0.47375E-02	-0.50929E-02	-0.46877E-02
2.30	0.61804E-02	0.90125E-02	-0.24386E-02	-0.33889E-02	-0.32227E-02
2.40	0.13320E-01	0.14993E-01	0.15828E-02	-0.33480E-03	-0.66334E-03
2.50	0.10905E-01	0.18661E-01	0.41110E-02	0.15787E-02	0.93358E-03
2.60	0.17595E-01	0.22569E-01	0.66952E-02	0.85840E 00	0.24370E-02
2.70	0.17455E-01	0.23427E-01	0.70340E-02	0.89805E 00	0.25093E-02
2.80	0.26761E-01	0.31233E-01	0.12655E-01	0.93823E 00	0.60678E-02
2.90	0.26318E-01	0.26054E-01	0.81919E-02	0.97496E 00	0.30243E-02
3.00	0.25589E-01	0.27067E-01	0.98867E-02	0.10165E 01	0.43495E-02

TABLE 6. (Continued)

I

L \ u	3.0	4.0	5.0	7.0	10.0
1.10	0.85462E-01	0.68230E-01	0.62960E-01	0.51006E-01	0.39668E-01
1.20	0.12836E 00	0.10381E 00	0.94638E-01	0.76544E-01	0.59530E-01
1.30	0.16830E 00	0.13736E 00	0.12434E 00	0.10048E 00	0.79227E-01
1.40	0.20512E 00	0.16820E 00	0.15148E 00	0.12234E 00	0.95449E-01
1.50	0.23962E 00	0.19720E 00	0.17663E 00	0.14241E 00	0.11151E 00
1.60	0.27524E 00	0.22708E 00	0.20291E 00	0.16334E 00	0.12824E 00
1.70	0.30951E 00	0.25578E 00	0.22760E 00	0.18337E 00	0.14406E 00
1.80	0.34188E 00	0.28321E 00	0.25079E 00	0.20231E 00	0.15925E 00
1.90	0.37562E 00	0.31151E 00	0.27544E 00	0.22216E 00	0.17505E 00
2.00	0.40626E 00	0.33693E 00	0.29757E 00	0.24023E 00	0.18935E 00
2.10	0.43871E 00	0.36400E 00	0.32080E 00	0.25919E 00	0.20450E 00
2.20	0.47111E 00	0.39110E 00	0.34450E 00	0.27841E 00	0.21999E 00
2.30	0.49705E 00	0.41280E 00	0.36340E 00	0.29358E 00	0.23144E 00
2.40	0.52891E 00	0.43960E 00	0.38650E 00	0.31232E 00	0.24620E 00
2.50	0.55648E 00	0.46250E 00	0.40630E 00	0.32829E 00	0.25886E 00
2.60	0.58555E 00	0.48682E 00	0.42724E 00	0.34535E 00	0.27258E 00
2.70	0.61176E 00	0.50884E 00	0.44641E 00	0.36100E 00	0.28493E 00
2.80	0.63804E 00	0.53112E 00	0.46555E 00	0.37651E 00	0.29759E 00
2.90	0.66246E 00	0.55143E 00	0.48291E 00	0.39056E 00	0.30908E 00
3.00	0.69057E 00	0.57480E 00	0.50303E 00	0.40670E 00	0.32232E 00

Q

L \ u	3.0	4.0	5.0	7.0	10.0
1.10	-0.98100E-03	0.24948E-01	0.22943E-01	0.18381E-01	0.13909E-01
1.20	-0.22484E-02	0.26991E-01	0.24823E-01	0.19911E-01	0.15182E-01
1.30	-0.33786E-02	0.24995E-01	0.23134E-01	0.18593E-01	0.14180E-01
1.40	-0.38144E-02	0.20478E-01	0.19197E-01	0.15485E-01	0.11724E-01
1.50	-0.45877E-02	0.13905E-01	0.13547E-01	0.11060E-01	0.81448E-02
1.60	0.11758E-01	0.74010E-02	0.76692E-02	0.65351E-02	0.45841E-02
1.70	0.43943E-02	0.13197E-02	0.24766E-02	0.23949E-02	0.13942E-02
1.80	-0.43830E-02	-0.59540E-02	-0.36861E-02	-0.26106E-02	-0.25678E-02
1.90	-0.10139E-01	-0.10748E-01	-0.79973E-02	-0.58533E-02	-0.51547E-02
2.00	-0.16923E-01	-0.15756E-01	-0.12377E-01	-0.94131E-02	-0.78912E-02
2.10	-0.23579E-01	-0.20233E-01	-0.16888E-01	-0.13542E-01	-0.11168E-01
2.20	-0.29263E-01	-0.25113E-01	-0.20964E-01	-0.16814E-01	-0.13680E-01
2.30	-0.35040E-01	-0.30062E-01	-0.25085E-01	-0.20107E-01	-0.16214E-01
2.40	-0.41402E-01	-0.35532E-01	-0.29663E-01	-0.23793E-01	-0.19042E-01
2.50	-0.46361E-01	-0.39766E-01	-0.33170E-01	-0.26575E-01	-0.21221E-01
2.60	-0.50934E-01	-0.44230E-01	-0.37130E-01	-0.29165E-01	-0.23280E-01
2.70	-0.55526E-01	-0.47976E-01	-0.40448E-01	-0.31870E-01	-0.25349E-01
2.80	-0.59041E-01	-0.50985E-01	-0.42985E-01	-0.33919E-01	-0.27009E-01
2.90	-0.62552E-01	-0.53907E-01	-0.45460E-01	-0.35930E-01	-0.28647E-01
3.00	-0.64552E-01	-0.55464E-01	-0.46771E-01	-0.37020E-01	-0.29513E-01

U

L \ u	3.0	4.0	5.0	7.0	10.0
1.10	0.32186E-01	-0.77451E-03	-0.70209E-03	-0.56529E-03	-0.44662E-03
1.20	0.34931E-01	-0.17942E-02	-0.16134E-02	-0.12864E-02	-0.10065E-02
1.30	0.32814E-01	-0.27345E-02	-0.24359E-02	-0.19561E-02	-0.15205E-02
1.40	0.27486E-01	-0.30629E-02	-0.27362E-02	-0.21906E-02	-0.17039E-02
1.50	0.19628E-01	-0.36795E-02	-0.32751E-02	-0.26218E-02	-0.20387E-02
1.60	-0.50790E-02	-0.41342E-02	-0.35975E-02	-0.28861E-02	-0.22815E-02
1.70	-0.53060E-02	-0.43983E-02	-0.37678E-02	-0.30296E-02	-0.24176E-02
1.80	-0.56181E-02	-0.46943E-02	-0.39633E-02	-0.32149E-02	-0.25570E-02
1.90	-0.56934E-02	-0.48032E-02	-0.38837E-02	-0.32519E-02	-0.25870E-02
2.00	-0.52797E-02	-0.45194E-02	-0.35673E-02	-0.30534E-02	-0.24140E-02
2.10	-0.47926E-02	-0.41289E-02	-0.34649E-02	-0.28009E-02	-0.22335E-02
2.20	-0.37266E-02	-0.32053E-02	-0.26839E-02	-0.21626E-02	-0.17626E-02
2.30	-0.26140E-02	-0.22621E-02	-0.19103E-02	-0.15584E-02	-0.12658E-02
2.40	-0.69957E-03	-0.63223E-03	-0.56488E-02	-0.49754E-03	-0.41177E-03
2.50	0.61448E-03	0.39671E-03	0.27895E-03	0.16118E-03	0.11950E-03
2.60	0.16796E-02	0.12061E-02	0.13062E-02	0.88249E-03	0.72678E-03
2.70	0.17017E-02	0.13766E-02	0.12988E-02	0.93031E-03	0.75589E-03
2.80	0.45282E-02	0.37056E-02	0.33353E-02	0.25448E-02	0.21615E-02
2.90	0.21252E-02	0.16894E-02	0.16143E-02	0.11500E-02	0.10414E-02
3.00	0.31521E-02	0.25564E-02	0.23588E-02	0.17159E-02	0.14841E-02

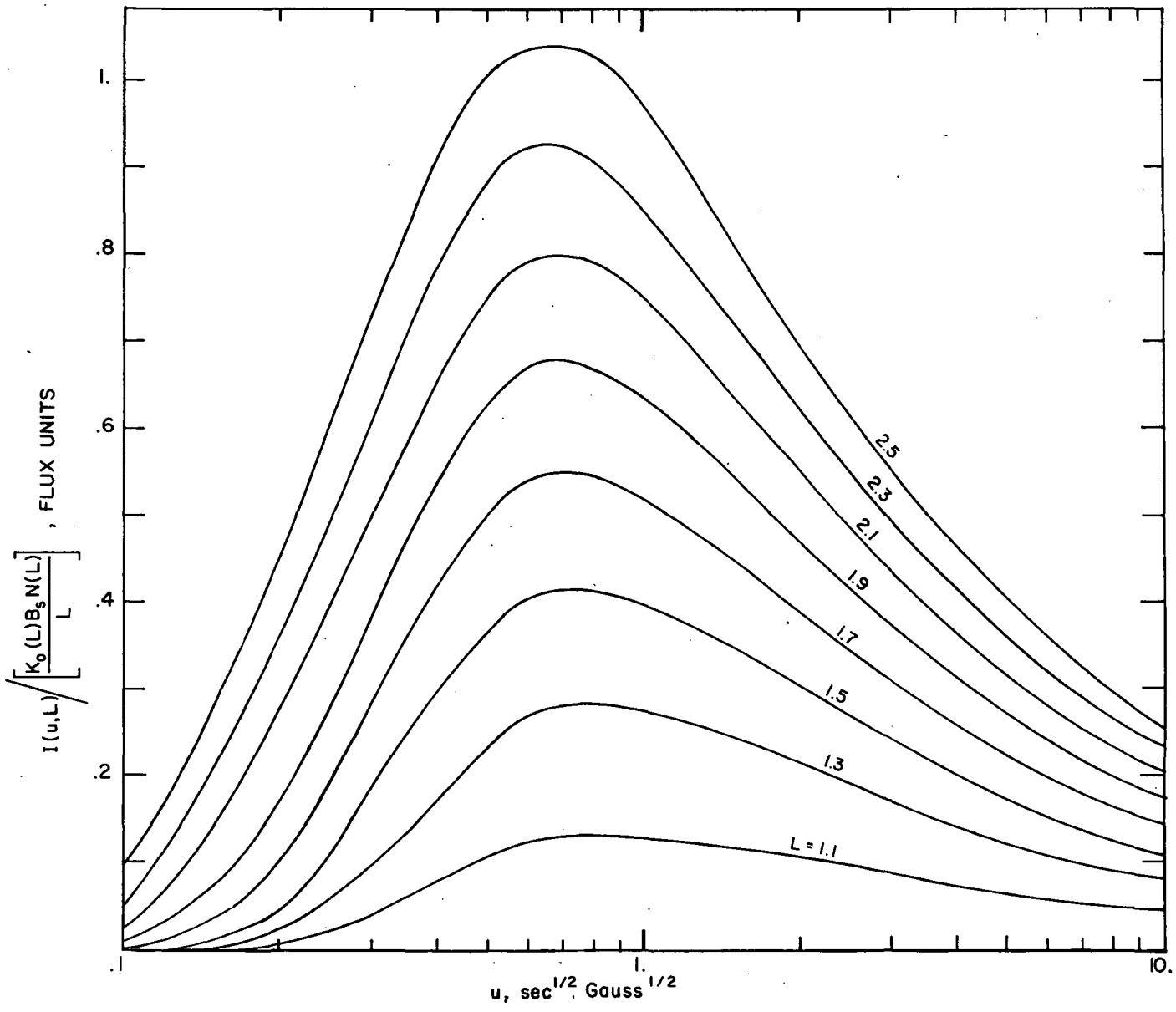

Figure 9. The function I(u,L) in units of the surface magnetic field B_S, the equatorial number density N(L) and the normalization constant $K_0(L)$ for an isotropic pitch angle distribution. $\Omega = 0^o$.

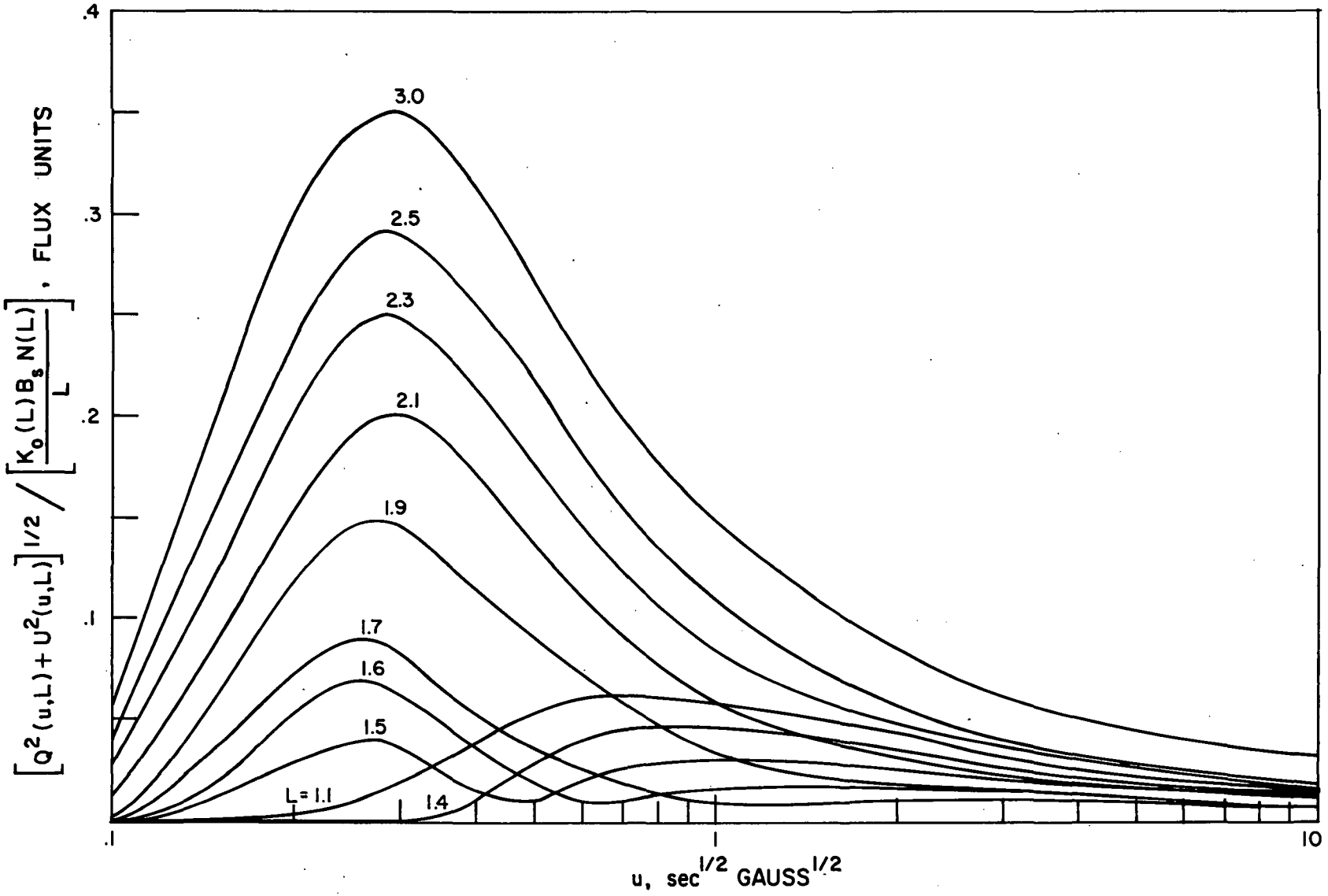

Figure 10. The function $[Q^2(u,L) + U^2(u,L)]^{1/2}$ in units of the surface magnetic field B_S, the equatorial number density N(L) and the normalization constant $K_0(L)$ for an isotropic pitch angle distribution. $\Omega = 0^o$.

emission as a function of L (Figure 11). Again we see a sharp drop in the degree of polarization near L = 1.6 with a rise to a peak near 2.0 and then a gradual decline with increasing L. In order to clarify this behavior we must refer to Figure 12. This shows the relationship between the equatorial pitch angle α_e and the corresponding range of positions, $\theta - \phi$ for the source points. Thus, if we set a limiting equatorial pitch angle $\alpha_e(\text{MIN}) = 15^\circ$, we can integrate only up to the colatitude $\theta = 67.5^\circ$ in the plane $\phi = 0^\circ$ as opposed to the colatitude $\theta = 60^\circ$ in the plane $\phi = 30^\circ$, or colatitude $\theta = 45^\circ$ in the plane $\phi = 90^\circ$ and so on. This situation repeats itself in reverse for $90^\circ < \phi \leq 180^\circ$. Thus for any limiting equatorial pitch angle such as described in Section E there will be a different range of source points for different ϕ-planes. Interference among those different planes will produce the curve obtained in Figure 11 with a minimum at the point of greatest interference. In the absence of the planet the minimum is exactly zero near L = 1.6. Thus, the effect observed is purely a consequence of the dipole geometry in its three-dimensional context. It should be noted that the degree of polarization generally increases with decreasing u at any given shell L (Figure 11).

The quantity $U(u,L)/Q(u,L)$ measures the angle between the plane of linear polarization and the magnetic equator (represented by $\hat{e}_y$ in Figure 3). By combining Equations (73) and (74) we see that this is simply a measure of tan 2χ where χ is the angle between the plane of polarization of the emission and the magnetic equator (or reference axis $\hat{e}_y$ in Figure 3). The results plotted in Figure 13 show a persistent anomalous behavior in the region of the minimal degree of polarization, i.e., when the electric vectors from different ϕ-planes nearly all cancel each other.

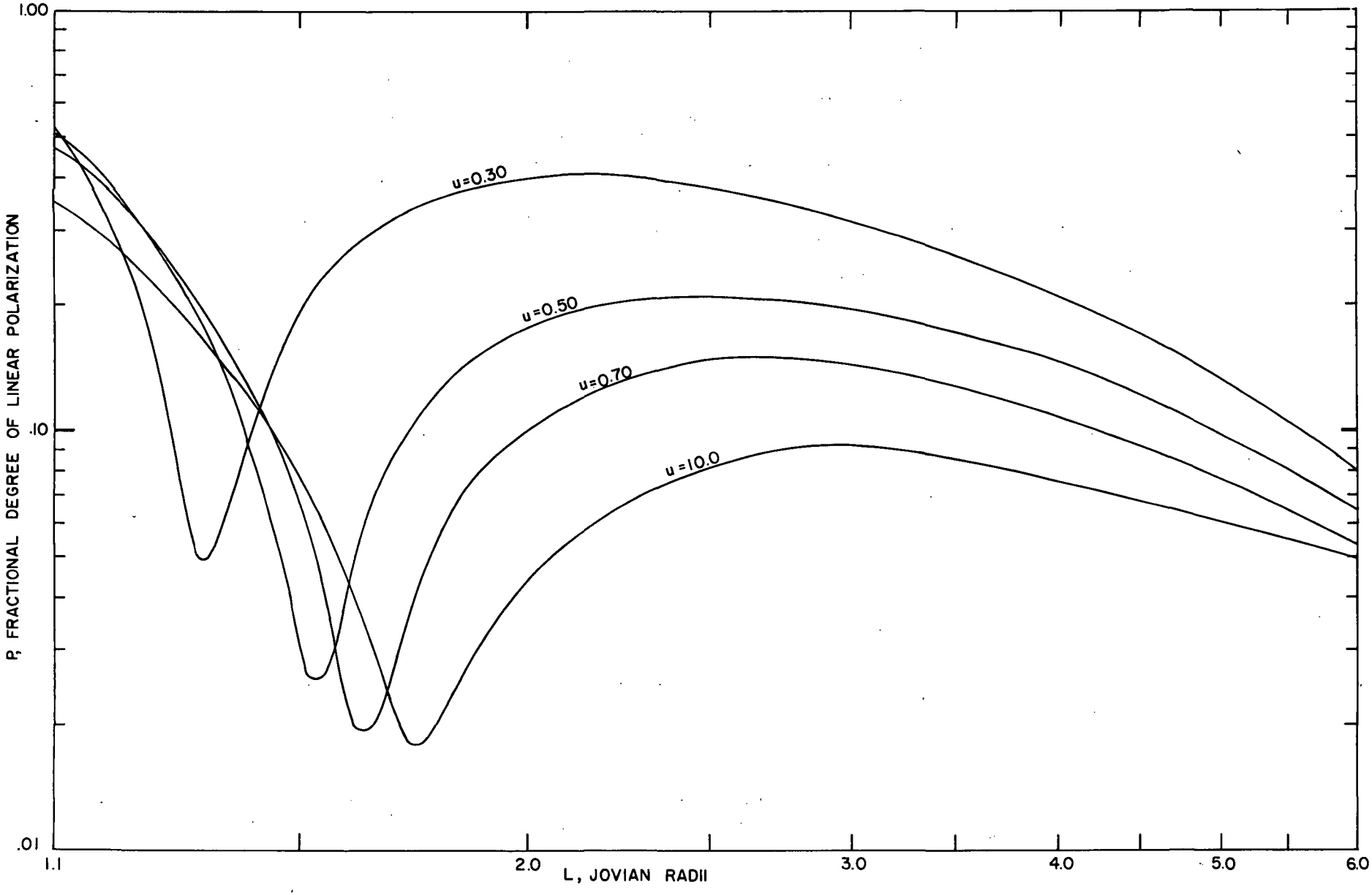

Figure 11. Fractional degree of polarization as a function of u and L. Note the sharp drop to less than 2 percent in the range L = 1.5 to L = 1.8. $\Omega = 0^{o}$.

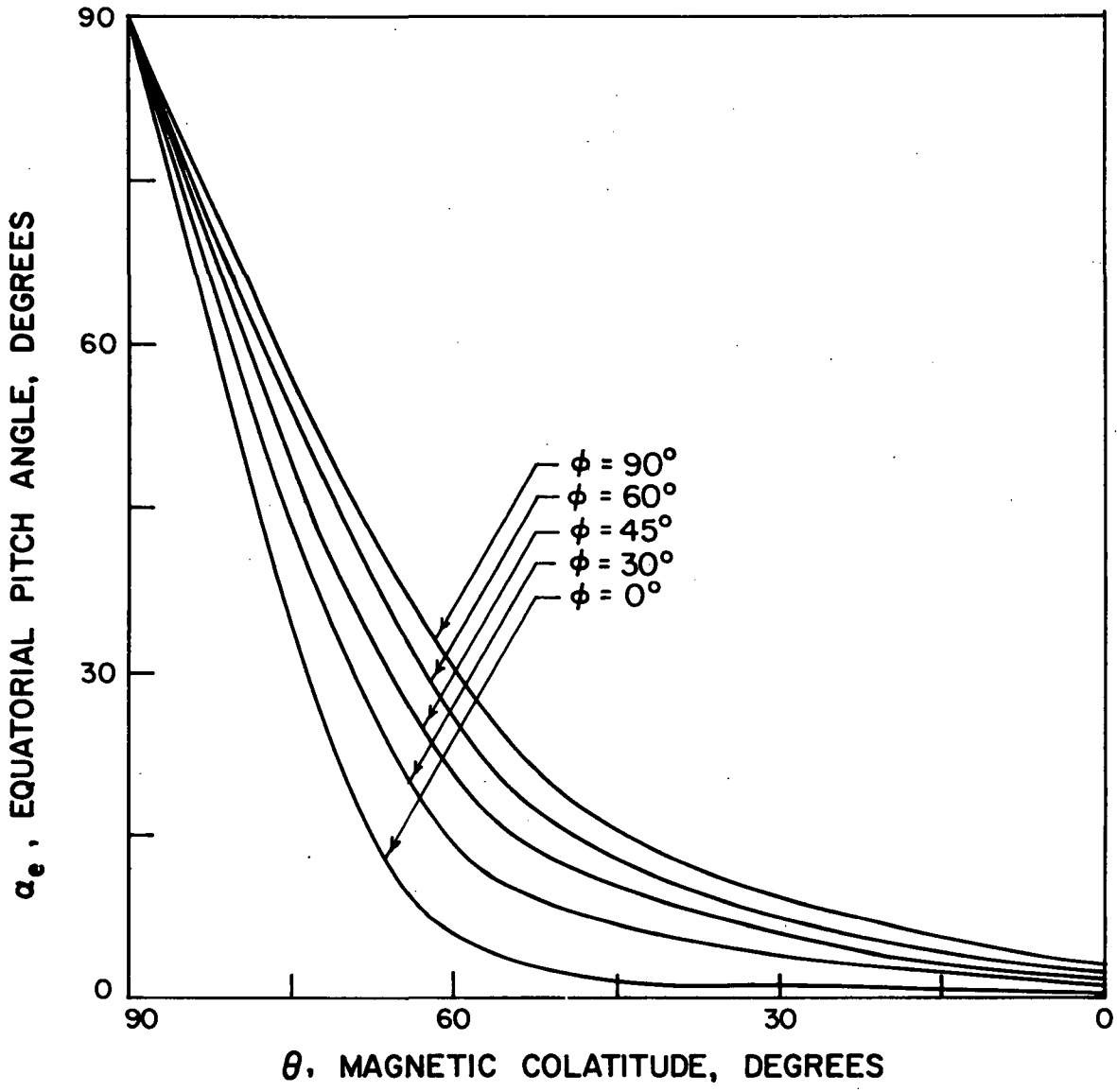

Figure 12. Magnetic colatitude (θ) of source points at various longitudes (ϕ) corresponding to electrons whose equatorial pitch angles are α_e. The electric vector of a source point at (θ,ϕ) is polarized in the direction $\vec{B} \times \hat{n}$ (See Figure 3). Interference among different ϕ-planes results in a minimum in the net polarization of the emission integrated over the entire source.

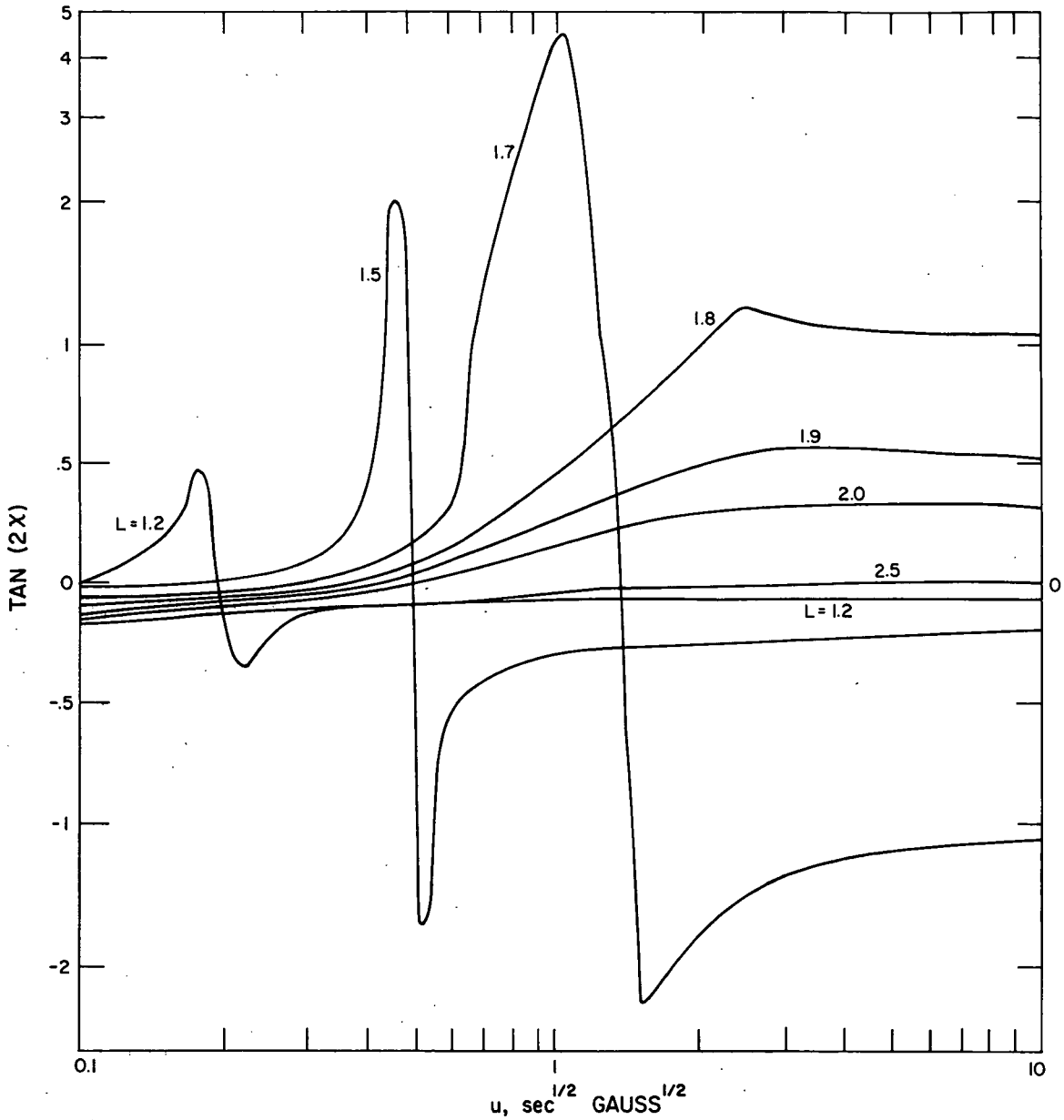

Figure 13. Tan $2\chi = U/Q$ as a function of u and L. χ is the angle between the plane of polarization and the magnetic equator (or reference axis $\hat{e}_y$ in Figure 3).

2. The anisotropic case

In the case of a distribution of electrons sharply confined to the magnetic equator, we immediately have $U_{60} \sim 0$. Thus, we have $\sqrt{Q_{60}^2(u,L) + U_{60}^2(u,L)} \simeq Q_{60}(u,L)$. The values for u = 1.5 are shown as functions of L in Table 7. The values at $\Omega = 0$ are designated with the superscript 0 and for $\Omega > 0^o$ the parameters are expressed as a ratio to the corresponding values at $\Omega = 0^o$. Furthermore the two components (1) and (2) (See Page 43) of the emission at $\Omega = 45^o$, 90^o, and 135^o are shown for comparison. We see that for $\Omega = 0^o$ both I_{60} and Q_{60} vary so slowly with shell distance that a single curve shown in Figure 14 may be used to represent both parameters for all shells with an accuracy far better than 10 percent. It is immediately apparent that the degree of polarization at $\Omega = 0^o$ is nearly constant with a value of 0.56 as L varies. In turn, the intensity at $\Omega = 90^o$ (when the colatitude of the observer θ_0 is 87^o) is increased by a factor of 2 over that at 0^o ($\theta_0 = 77^o$). This is to be compared with the isotropic case where an increase in the occultation of the source points with rotation (See Table 4) results in an actual decrease in the intensity at $\Omega = 90^o$ for shell distances $L \leq 2$.

The change in the intensity (or degree of polarization) with shell distance is more marked with increasing rotation angle Ω. This is due to the fact that at these larger angles the occultation of source points close to the equatorial plane rapidly decreases with increasing L. Comparison of the two longitudinal components of the intensity shows that component (2) (east component) is consistently less than component (1) (west component) by 2 to 3 percent, the difference being greatest for shells closer to the planet, i.e., when the occultation effects are a maximum).

TABLE 7

STOKES PARAMETERS AS FUNCTION OF u AND L FOR THE ECLIPSED CASE ($U \neq 0$). (The pitch angle distribution is of the form $\sin^{60} \alpha_e$. For $\Omega > 0^o$ the quantities are expressed as a ratio to the corresponding value at $\Omega = 0$, $u = 1.5$.)

$\Omega = 0^o$

L	$I^o = I_{60}(u,L)$	$P^o = \sqrt{Q_{60}^2(u,L) + U_{60}^2(u,L)}$
1.1	0.01375	0.00770
1.3	0.01415	0.00793
1.5	0.01436	0.00805
1.7	0.01447	0.00812
1.9	0.01456	0.00817
2.1	0.01463	0.00821
2.3	0.01469	0.00825
2.5	0.01473	0.00827
2.7	0.01477	0.00829
2.9	0.01480	0.00831

$\Omega = 45^o$

L	$I_{60}^{(1)}(u,L)/I^o$	$I_{60}^{(2)}(u,L)/I^o$	$\sqrt{Q_{60}^2(u,L) + U_{60}^2(u,L)}/P^o$
1.1	0.62759	0.61313	1.24429
1.3	0.65591	0.64222	1.30321
1.5	0.66892	0.65531	1.33024
1.7	0.67749	0.66403	1.34822
1.9	0.68472	0.67006	1.36204
2.1	0.69005	0.67493	1.37268
2.3	0.69349	0.67807	1.37954
2.5	0.69611	0.68236	1.38675
2.7	0.69866	0.68493	1.39211
2.9	0.70120	0.68749	1.39742

TABLE 7 (cont.)

$\Omega = 90^{o}$

L	$I_{60}^{(1)}(u,L)/I^{o}$	$I_{60}^{(2)}(u,L)/I^{o}$	$\sqrt{Q_{60}^{2}(u,L) + U_{60}^{2}(u,L)}/P^{o}$
1.1	0.85099	0.83574	1.69777
1.3	0.93968	0.91810	1.87130
1.5	0.97904	0.95779	1.95302
1.7	1.00662	0.98547	2.00985
1.9	1.02410	1.00554	2.04883
2.1	1.04054	1.02031	2.08132
2.3	1.04935	1.03098	2.10157
2.5	1.05794	1.04300	2.12306
2.7	1.06607	1.04743	2.13615
2.9	1.07378	1.05376	2.15080

$\Omega = 135^{o}$

L	$I_{60}^{(1)}(u,L)/I^{o}$	$I_{60}^{(2)}(u,L)/I^{o}$	$\sqrt{Q_{60}^{2}(u,L) + U_{60}^{2}(u,L)}/P^{o}$
1.1	0.63314	0.62402	1.26250
1.3	0.76025	0.74050	1.50584
1.5	0.82227	0.81042	1.64006
1.7	0.86559	0.85038	1.72543
1.9	0.89407	0.88211	1.78751
2.1	0.91649	0.90624	1.83562
2.3	0.93541	0.92364	1.87323
2.5	0.95020	0.94053	1.90609
2.7	0.96355	0.95393	1.93387
2.9	0.97552	0.96388	1.95666

TABLE 7 (cont.)

$\Omega = 180^{o}$

L	$I_{60}(u,L)/I^{o}$	$\sqrt{Q_{60}^{2}(u,L) + U_{60}^{2}(u,L)}/P^{o}$
1.1	0.89823	0.89928
1.3	1.13496	1.13346
1.5	1.26095	1.26083
1.7	1.34946	1.35111
1.9	1.41435	1.41761
2.1	1.45664	1.46125
2.3	1.49881	1.50476
2.5	1.53502	1.54225
2.7	1.56189	1.57013
2.9	1.58586	1.59504

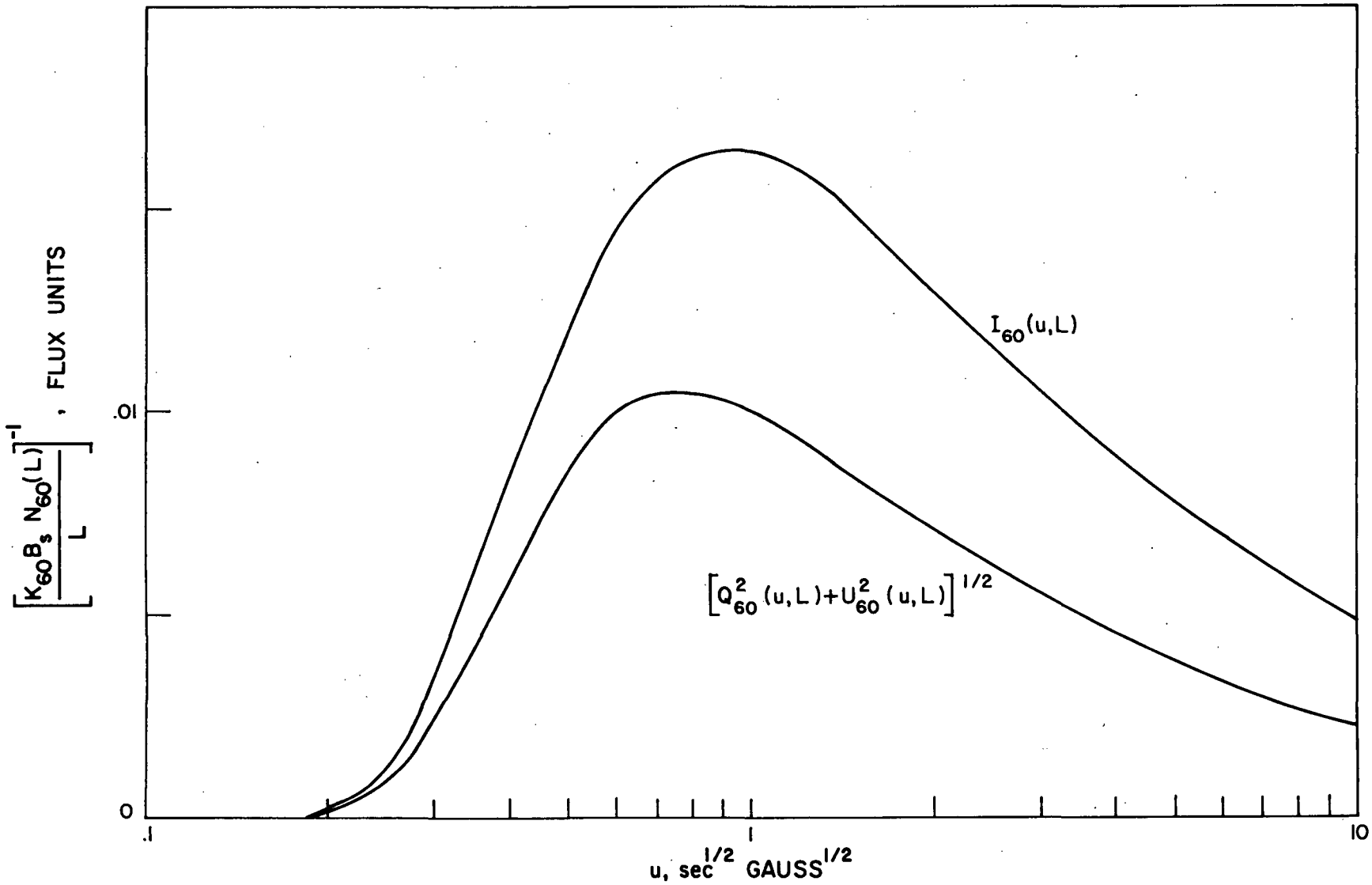

Figure 14. The functions $I_{60}(u,L)$ and $[Q_{60}^2(u,L) + U_{60}^2(u,L)]^{1/2}$ in units of the surface magnetic field B_S, the equatorial number density $N_{60}(L)$ and the normalization constant K_{60} for a pitch angle distribution of the form $\sin^{60}\alpha_{eo}$. A single set of curves is accurate within 10 percent for all shells at $\Omega = 0$ (See Table 7).

3. The intensity as a function of the energy-dependent variable u' for a shell at distance L.

The Stokes parameters given by Equations (72) to (75) were computed as a function of the variable u for a given shell at distance L. The results for the isotropic and non-isotropic cases are shown in Figures 9, 10, and 14, and Tables 6 and 7. To calculate the Stokes parameters as functions of the energy variable $u' = \sqrt{B_s}\ \varepsilon/\varepsilon_0$ at a frequency f, we make the transformation $u' = (fL^3)^{1/2} u$ [See Equation (67)]. The results for the intensity function are shown in Figure 15 for the shells L = 2 and L = 4. It is clear that the intensity peak moves to higher values of u', i.e., towards increasing energy, with increasing frequency of emission. Also comparison between the two shells shows that the intensity peak at a given frequency moves to higher values of u' in going from an inner to an outer shell. It is also obvious that for low values of the energy (say $u' < 100$) the integrated intensity from the outer shell at 100 MHz is greater than at 1000 MHz. On the other hand the intensities are of similar magnitude in the inner shell. This pattern is a direct reflection of the behavior of the emissivity-polarization functions for synchrotron radiation. These functions show a peak near x = 0.3, then fall rapidly with increasing argument and more slowly in the other direction as shown in Figure 14 above. Here we express this argument x as an inverse function of energy for a given frequency and a magnetic field strength which falls as $1/L^3$ in the equatorial plane [See Equation (67)]. This pattern partly accounts for the observational evidence (Gulkis, 1970) that the Jovian radiation belts appear to broaden with decreasing frequency. This effect will be elaborated upon later.

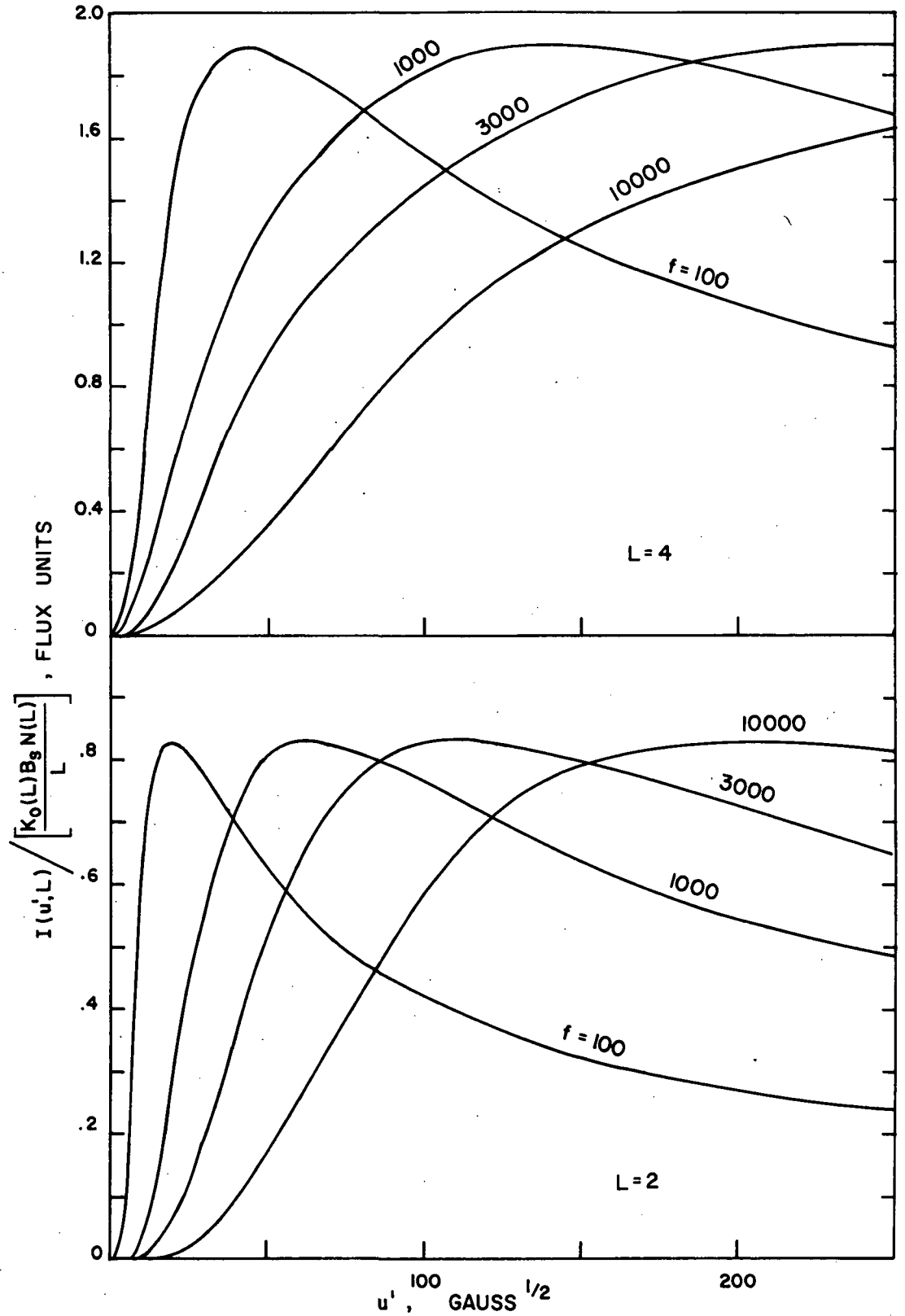

Figure 15. The function I(u',L) in units of the surface magnetic field B_S, the equatorial number density N(L) and the normalization constant $K_0(L)$ for an isotropic pitch angle distribution. Results are shown for different frequencies at the shell distances L = 2 and L_o = 4. $u' = \sqrt{B_S}\ \varepsilon/\varepsilon_0$ is the energy-dependent variable. $\Omega = 0^o$. The frequencies f are in MHz.

CHAPTER III. APPLICATION TO JUPITER

A. Observations of the Radiation Belts of Jupiter

The collected results (Dickel, Degioanni, and Goodman, 1970) of a large number of observations of Jupiter in the decimeter range are shown in Figures 16a, 17, and 18. The non-thermal spectrum derived in Figure 16a was obtained assuming the thermal models of Berge (1966) and Branson (1968). The resultant spectrum shows a peak near 800 MHz and falls very slowly on either side of this frequency. The approximate ratio of the intensity at 1430 MHz to those at 100 MHz and 3000 MHz is about 1.5. The fractional polarization of synchrotron emission reaches a peak of about 30 percent near a frequency of 3000 MHz and falls on either side of this frequency.

It has been well established (Roberts and Ekers, 1968) that the total intensity shows a variation with longitude of the central meridian of the disk as shown in Figure 33a. This variation has an amplitude of 10 to 20 percent between at least 600 MHz and 3000 MHz and probably to much lower and higher frequency limits. The variation has a minimum at about $\lambda_{III} = 20^{o}$ which is greater than the minimum at $\lambda_{III} = 200^{o}$. When these data are replotted as a function of the zenomagnetic latitude of the Earth $(90^{o} - \theta_{0})$ they show an asymmetry such that the radiation from southern latitudes falls more rapidly with increasing latitude than the radiation from the northern latitudes. Warwick (1967) has shown that if the radiation is assumed to be strongly beamed at an angle of 1.2^{o} above the equatorial plane of the dipole, then the intensity of the radiation measured with respect to a new equatorial plane, defined as $\theta_{0}' = \theta_{0} - 1.2^{o}$, becomes symmetric as a function of the zenomagnetic angle. To produce a

minimum field strength 1.2^{o} above the dipolar equator requires that a small linear quadrupole (3 Gauss) be superimposed on a pure dipole.

Several high resolution observations of the radiation belts of Jupiter have established that the source can be approximated by a planet-centered uniform ellipse with major and minor axes of 3 and 1 diameters of Jupiter. Furthermore, it has been demonstrated (Gulkis, 1970) that the belts are broader at the lower frequencies. Specifically at least 90 percent of the emission at 100 cm originates within 5.5 Jovian radii from the ephemeris position of the planet. On the other hand, at least 90 percent of the emission at 21 cm originates within 3 Jovian radii from the ephemeris position. Branson (1968) has also observed an asymmetry in the intensities of the peaks of radio brightness on either side of the planet. This small asymmetry was described by him as due to some anomaly in either electron density or more probably in the magnetic field at a longitude close to 200^{o}. The anomaly was seen to move from west to east as the maps at different increasing longitudes were compared.

Because of the 10^{o} inclination of the magnetic axis relative to the rotational axis, the plane of polarization of the synchrotron emission is observed to oscillate with an amplitude of 10^{o} as a function of the central meridian longitude. The observed curve for this oscillation has been shown to depart significantly from the simple sinusoidal form predicted for a dipolar field (Roberts and Komesaroff, 1965). Conway and Stannard (1972) attempted to explain this effect as well as Branson's (1968) hot spot near $\lambda_{III} = 200^{o}$ in terms of a magnetic anomaly similar to the Atlantic anomaly around the equator of the Earth (this anomaly results from a localized tilting of the magnetic lines of force such

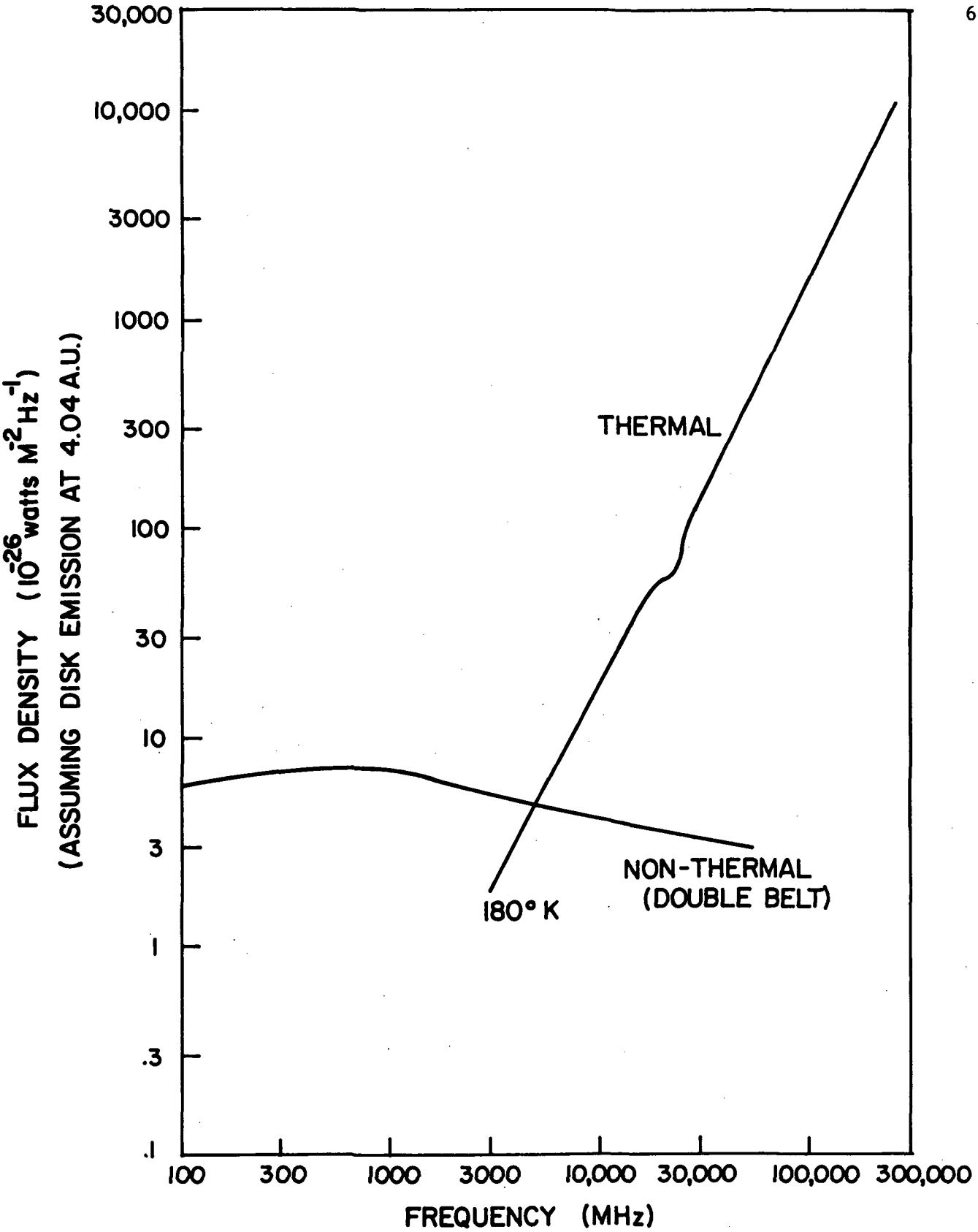

Figure 16b. (Overlay) Present non-thermal model with a double belt system (See discussion in Section 10). The thermal model is derived by subtracting the present non-thermal spectrum from the observed spectrum in (a).

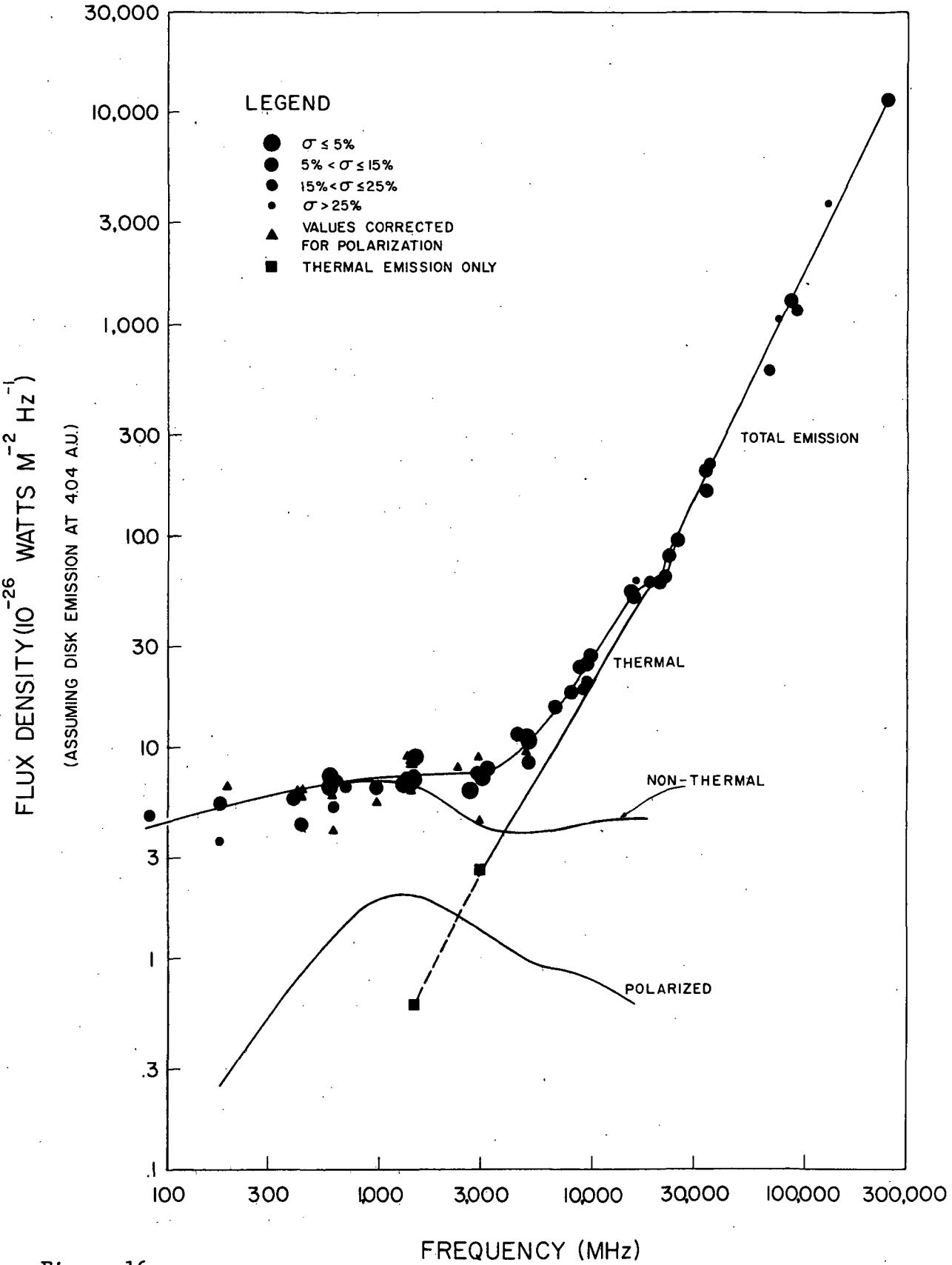

Figure 16a.
The radio spectrum of Jupiter showing all published measurements and their error (Dickel, Degioanni and Goodman, 1970)

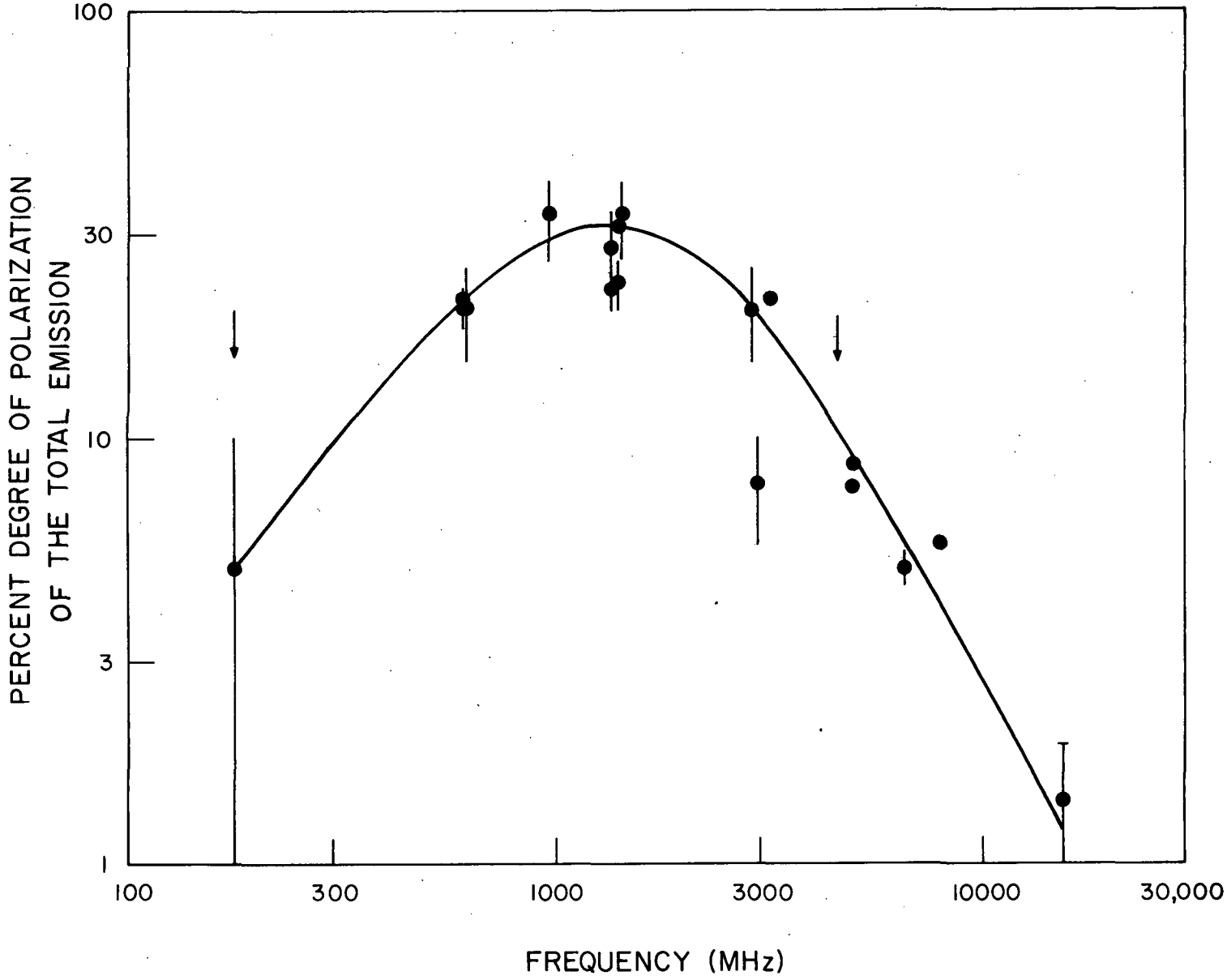

Figure 17. Polarization of the total emission from Jupiter (Dickel, Degioanni and Goodman, 1970).

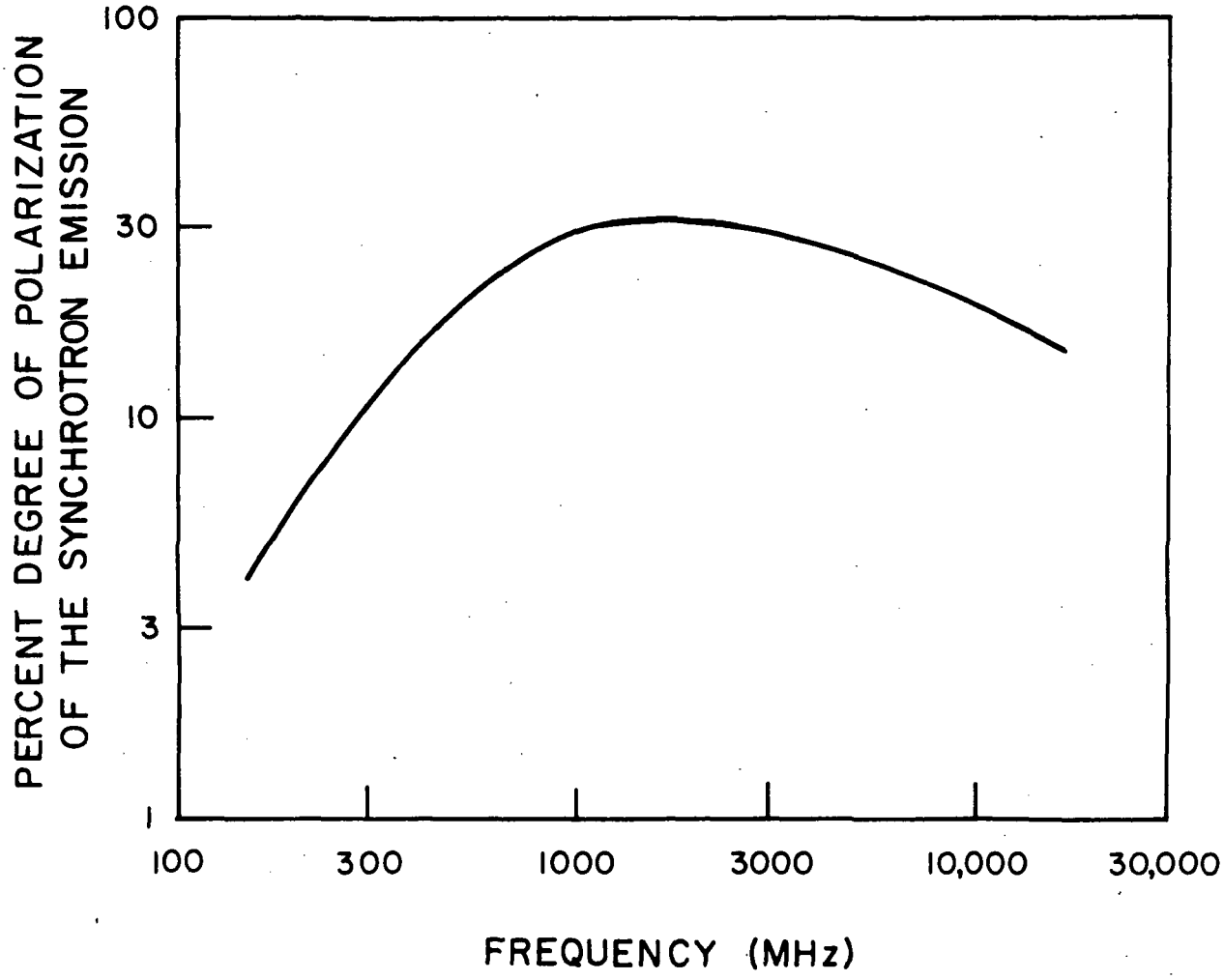

Figure 18. Polarization of the non-thermal emission from Jupiter (Dickel, Degioanni and Goodman, 1970).

that the normal to the field lines no longer lies in the plane of the magnetic equator).

B. The Theoretical Model of the Radiation Belts in a Planet-Centered Corotating Dipolar Field

1. General considerations

As we will see it is convenient to subdivide the radiation belts of Jupiter into two zones, the inner zone located between the surface and L = 2 and the outer zone extending beyond L = 2. This division is similar to that employed by Melrose (1967) in describing the rotational effects on the distribution of thermal plasma in the magnetosphere of Jupiter. He describes an inner region where the net acceleration is towards the planet and the particles satisfy a Maxwellian velocity distribution. At about L = 2, the field-aligned components of centrifugal and gravitational force are equal. Beyond this point the centrifugal predominance results in a density distribution that is flattened in the equatorial plane and falls as BL^{-1} with increasing L. Also the velocity distribution of the plasma in this outer region becomes increasingly anisotropic with increasing distance. The corotating magnetosphere breaks up as a result of electrostatic microinstabilities at L = 7,well inside the boundary with the solar wind (L = 53).

The density and velocity distributions of the high-energy particles that form the radiation belts are probably quite distinct from the corresponding values of the thermal plasmasphere as the origin and dynamics of these relativistic particles are not as clearly understood. Nonetheless, a great number of observations have been accumulated on the Earth's Van Allen radiation belts. Results from one of the early satellite experiments (July 1963) are reproduced from Radiation Trapped in the Earth's Magnetic Field, ed. B. M. McCormac, 1966, in Figure 19. They show

that the energy spectrum of electrons in the inner belt is significantly softer than in the outer belt. The electron intensities fall with increasing latitude in both belts (the satellite orbit was such that the minimum latitude reached in the outer belt was 50^{o}). Figures 19 (E) and (F) show the electron pitch-angle distribution in the belts. The solid curves indicate the distributions expected on the basis of the perpendicular intensities of Figures 19 (C) and (D) and are consistent with the measured distributions within the limits of accuracy determined by the instrumental aperture and the uncertainty in aspect determination. The pitch angle distribution appears narrower in the inner regions as compared to the outer regions. However, the cutoffs established by the dashed curves are what one would expect were the distributions isotropic with only the surface of the Earth as a limiting factor.

For a corotating terrestrial magnetosphere, centrifugal and gravitational forces balance at about 6.5 R_E (Ioannidis and Brice, 1971). However, at this distance the magnetosphere is not simply corotating and the plasma is not in diffusive equilibrium with the ionosphere. Inside the plasmapause where the magnetospheric motion approximates corotation, the centrifugal force is less than the gravitational force and does not play a major role in determining the plasma density. Similarly, the centrifugal force does not affect the Earth's radiation belts described above. Thus the effect of the centrifugal force on the distribution of particles in the Jovian radiation belts has no terrestrial counterpart and it can be inferred only from observations and a theoretical model.

For $L < 2$ the interferometric and lunar occultation observations do not provide fine resolution of the intensity of the emission. Thus,

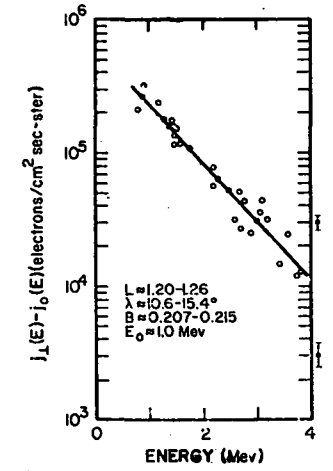

A) Inner belt electron integral energy spectrum.

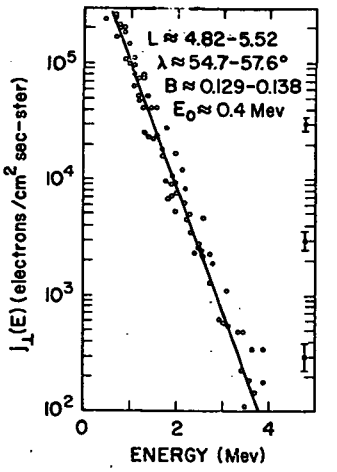

B) Outer belt electron integral energy spectrum.

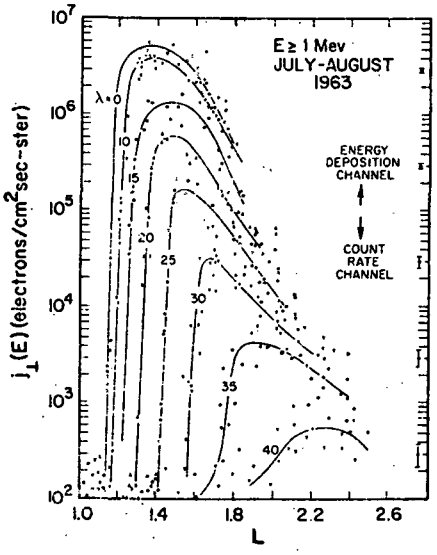

C) Electron intensities in the inner belt at various λ.

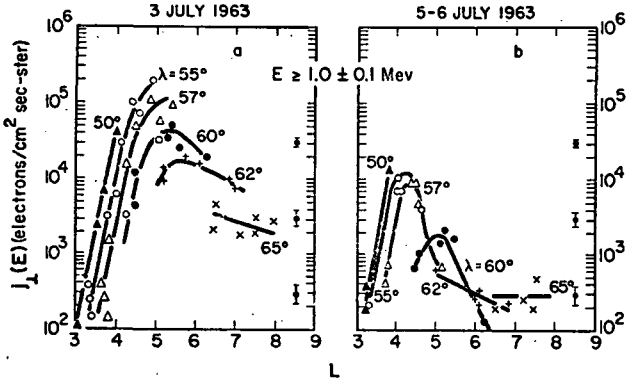

D) Electron intensities in the outer belt at various λ.

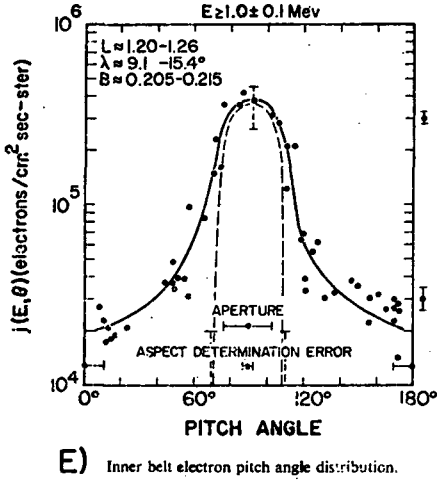

E) Inner belt electron pitch angle distribution.

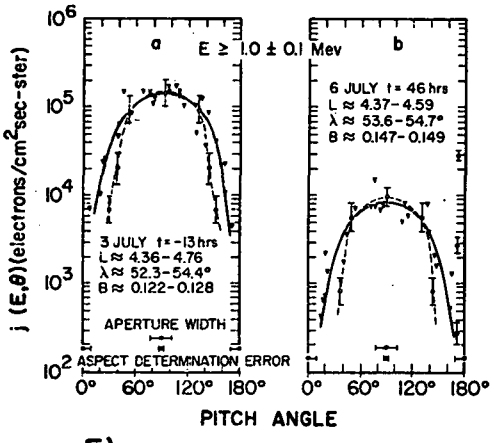

F) Outer belt electron pitch angle distribution.

Figure 19. Results from early satellite observations (July 1963) of the terrestrial radiation belts. The lowest latitude (represented by λ) attained by the satellite in the outer belt was $\lambda \doteq 50^{0}$. Reproduced from Radiation Trapped in the Earth's Magnetic Field, ed. B. M. McCormac, 1966.

in order to allow for the possibility that the properties (number density, energy and pitch-angle distributions) in the outer zone (L > 2) are quite different from those in the inner zone (L < 2), we have arbitrarily divided the intensity distribution into the same two zones. This requires a rapid decline of the intensity from the outer region with decreasing L for L < 2 so we may treat the intensity function in the inner zone as a separate distribution.

2. The outer zone

The observations by Branson (1968) have shown that approximately 90 percent of the emission at 21 cm occurs within 3 Jovian radii of the ephemeris position. Observations by Berge (1966) at 10.4 cm support this result. The emission pattern in both cases shows a peak near L = 2 and then falls gradually with increasing distance from the planet.

A practical and reasonable approximation to the intensity of the emission at 21 cm as a function of shell distance for $L \geq 2$ is given by the Poisson distribution of order 6,

$$F(L) = 6.7^{y} e^{-6.7}/\Gamma(Y + 1) , \qquad \text{for } L \geq 2 \tag{77a}$$

where Y = 6*L/1.8.

The representation for the decrease in intensity from the outer zone inside L = 2 is taken as the Gaussian of halfwidth $\Delta L = 0.1$,

$$F(L) = Ae^{-25(L-2)} , \text{ for } L < 2 \tag{77b}$$

where $A = 6.7^{y_0} e^{-6.7}/\Gamma(Y_0 + 1)$

$$Y_0 = 6*2/1.8.$$

We also anticipate that the pitch-angle distribution in the outer zone is confined in a plane close to the magnetic equator, particularly for $L \geq 2$. If indeed the distribution is anisotropic, i.e., is significantly affected by the centrifugal force of the corotating magnetosphere, it probably becomes increasingly so with increasing distance in analogy with the effect of this force on the thermal plasma (Melrose, 1967). We do not know what this function might be and an approximation is made by using a constant anisotropy factor NQ in the outer zone.

We also assume, at this point, that the energy distribution in a given zone is independent of both L and the magnetic latitude. From the results obtained in terrestrial satellite experiments, this appears to be valid.

From Equations (72) to (74) we get the expressions for the net flux and degree of polarization received at a frequency f from a shell at distance L and for a particular energy-dependent variable u',

$$I_f(u',L) = D(L)[m_{60}I_{f_{60}}(u',L) + m_0 I_{f_0}(u',L)] \quad , \tag{78}$$

and $$P_f(u',L) = D(L)[m_{60}P_{f_{60}}(u',L) + m_0 P_{f_0}(u',L)]/I_f(u',L) \quad , \tag{79}$$

where m_0, m_{60} are given by Equations (70) and (71),

$$P_f(u',L) = [Q_f^2(u',L) + U_f^2(u',L)]^{1/2} \quad ,$$

and $D(L) = B_s N(L)$, the equatorial density profile.

Now, if we combine Equation (78) evaluated at 1430 MHz with the intensity profile at this frequency given by Equations (77a) and (77b), and a profile in the anisotropy factor NQ defined in Equation (80), we can

solve for the equatorial density profile D(L). The solution is unique for a particular distribution in the energy-dependent variable u'. The solution for D(L) is given in Section B-4 below. Once D(L) is available, we can solve for the expected intensities at the other frequencies. To obtain the longitudinal variations we set the intensity and polarization profiles of Equations (77a) and (77b) to be the observable distributions at 1430 MHz for $\Omega = 0^{o}$. This approach is justified since the observed intensity distributions show very little change with rotation (Branson, 1968).

The Stokes parameters of Equations (72) through (74) were integrated for values of u' ranging from 0 to 250. For a surface field of 10 Gauss this imposes a maximum energy of 40 Mev; in our energy spectra u' was subdivided into increments of 10 units ($\Delta u' = \sqrt{B}_s \, \Delta(\varepsilon/\varepsilon_0) = 10$) and the energy spectra were represented as histograms in the variable $\sqrt{B}_s \, \varepsilon/\varepsilon_0$ with this resolution ($\Delta u' = 10$ or 1.6 Mev for a surface field of 10 Gauss).

Centrifugation of the electrons in the equatorial plane affects primarily the degree of polarization of the emission and the degree of beaming of the radiation into a cone sharply confined to the magnetic equator. The latter, in turn, is observed as a variation in the received intensity as the planet rotates and as an oscillation of the plane of the magnetic equator with an amplitude of 10^{o} above and below the line of sight to the Earth. Such variation at 1430 MHz is displayed in Figure 20 for several different values of the anisotropy factor NQ. The curves are drawn for the particular case of a uniform distribution of particle energy in the outer zone. The shape and trend of the variation of the curves with NQ is similar for whatever energy distribution is chosen in the outer zone. As discussed on Page 73 we use the following

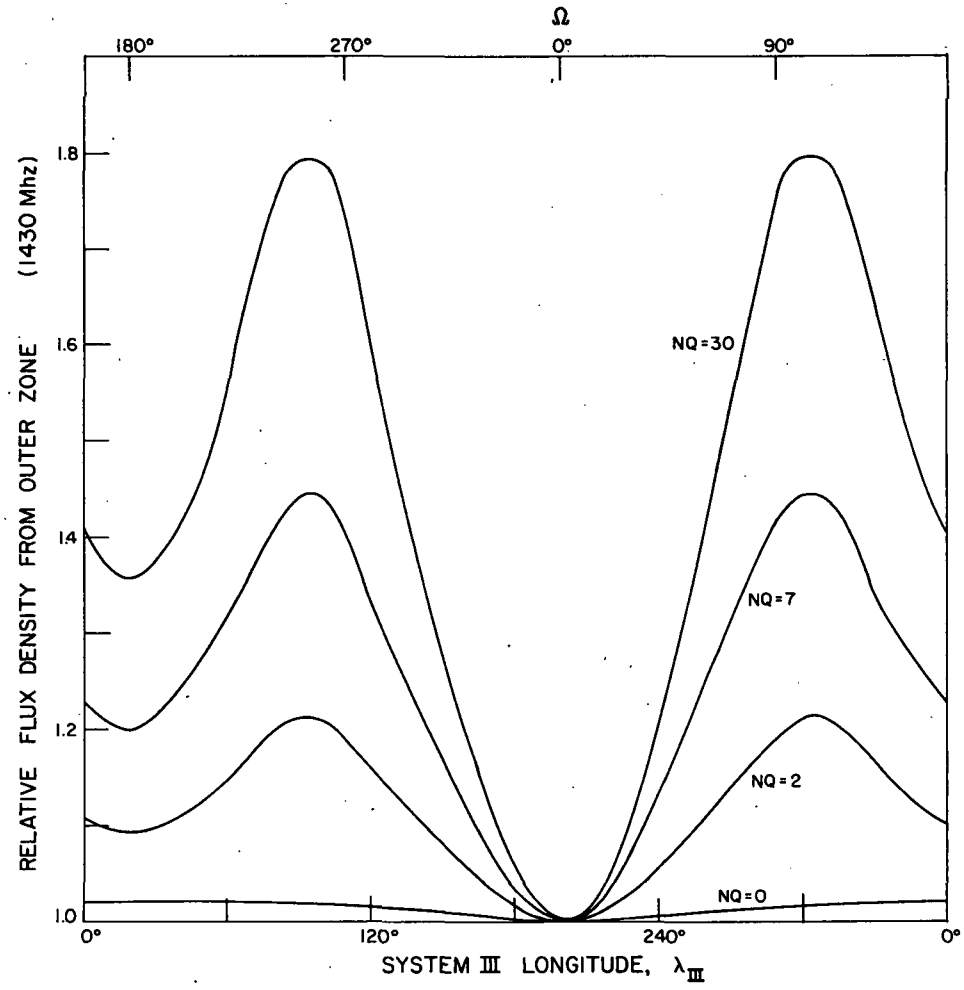

Figure 20. Variation in the flux density with Jovian rotation recieved from the outer zone at f = 1430 MHz. NQ = 0 for L < 1.8. NQ = 2 for 1.8 ≤ L < 2.0, and for L ≥ 2.0 the values for NQ are labeled on the different curves. The amplitude of the oscillations is extremely sensitive to the degree of anisotropy in the outer zone indicating that not all the particles are necessarily confined to the magnetic equator in the outer zone (see the text).

step-up function for the anisotropy factor NQ:

$$\begin{aligned} &NQ(L < 1.8) = 0, \\ &NQ(1.8 \leq L < 2) = a, \text{ and} \\ &NQ(L \geq 2) = b, \text{ such that } b \geq a. \end{aligned} \tag{80}$$

The curves plotted in Figure 20 show the oscillation in the intensity at 1430 MHz for $NQ(L \geq 2) = 0$ (with $a = 0$) and $NQ(L \geq 2) = 2, 7, 30$ (with $a \approx 2$). These curves represent the cases where 0, 67 percent, 87.5 percent, and 97 percent, respectively, of the particles beyond $L = 2$ belong to a population of electrons whose pitch angles are very near 90°, i.e., with a distribution of the form $\sin^{60} \alpha_e$. It is significant that not all the particles, and, in fact, no more than 90 percent can be confined to the equatorial plane if the observed oscillations are to show an amplitude in the 10 to 20 percent range.

The curves clearly show a minimum at $\lambda_{III} = 198^{\circ}$ which is deeper than the minimum at $\lambda_{III} = 18^{\circ}$. The minimum at $\lambda_{III} = 18^{\circ}$ is higher because the Earth lies within 7° of the magnetic equator at this longitude as opposed to 13° when $\lambda_{III} = 198^{\circ}$.(*) However, the amount of occultation of the radiation belts is largest when $\lambda_{III} = 18^{\circ}$ and least when $\lambda_{III} = 198^{\circ}$ (See Table 4). Since occultation and beaming are in the opposite direction, the total range of the longitudinal variation is reduced from what would be obtained in a non-eclipsed model. Also, the gradual increase in occultation with increasing longitude produces an apparent asymmetry which is best shown in a plot of intensity as a function of the absolute zenomagnetic latitude of the Earth. Figure 21(a) shows this apparent

---

(*) These results apply to the epochs when the Joviocentric declination of the Earth is $+3^{\circ}$.

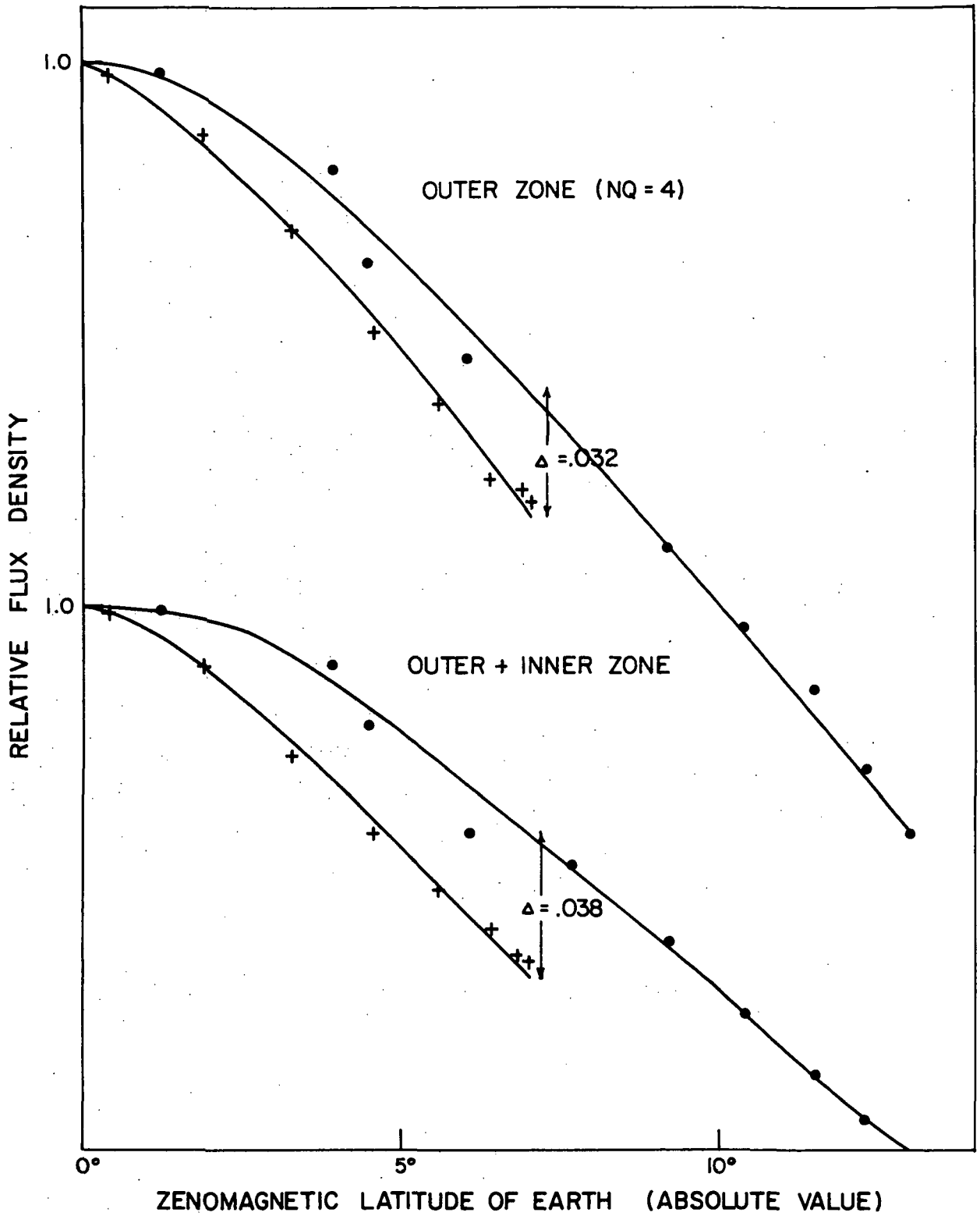

Figure 21. (a) Top graph. This is obtained by replotting the intensities shown in Figure 20 for NQ = 4 as a function of the zenomagnetic latitude of the Earth read from Figure 4. The symbols (•) and (x) represent points corresponding to southern and northern latitudes, respectively. Occultation by the planet produces an apparent asymmetry in the emission from the two hemispheres. (b) Bottom graph. This is obtained by replotting the intensities read in Figure 31 for the combined zones as a function of the zenomagnetic latitude of the Earth read from Figure 4. The symbols (•) and (x) represent points corresponding to southern and northern latitudes, respectively. The asymmetry is enhanced by adding the inner zone which has a relatively greater amount of occultation.

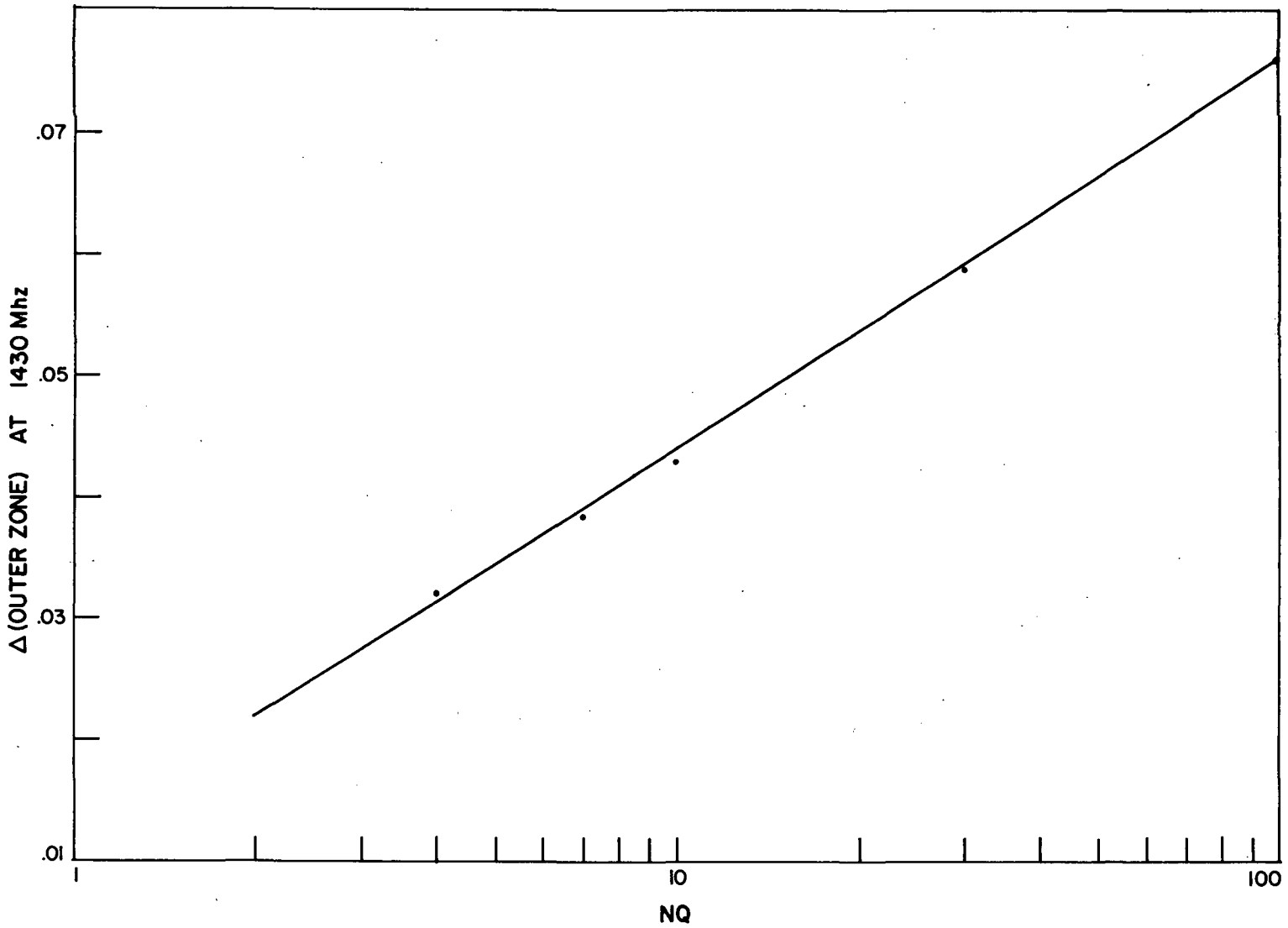

Figure 22. Δ (see the text) as a function of NQ. The asymmetry shown in Figure 21 increases with increasing NQ since the effect of the occultation on a distribution of particles confined to the magnetic equator is much greater than the same effect on an isotropic distribution.

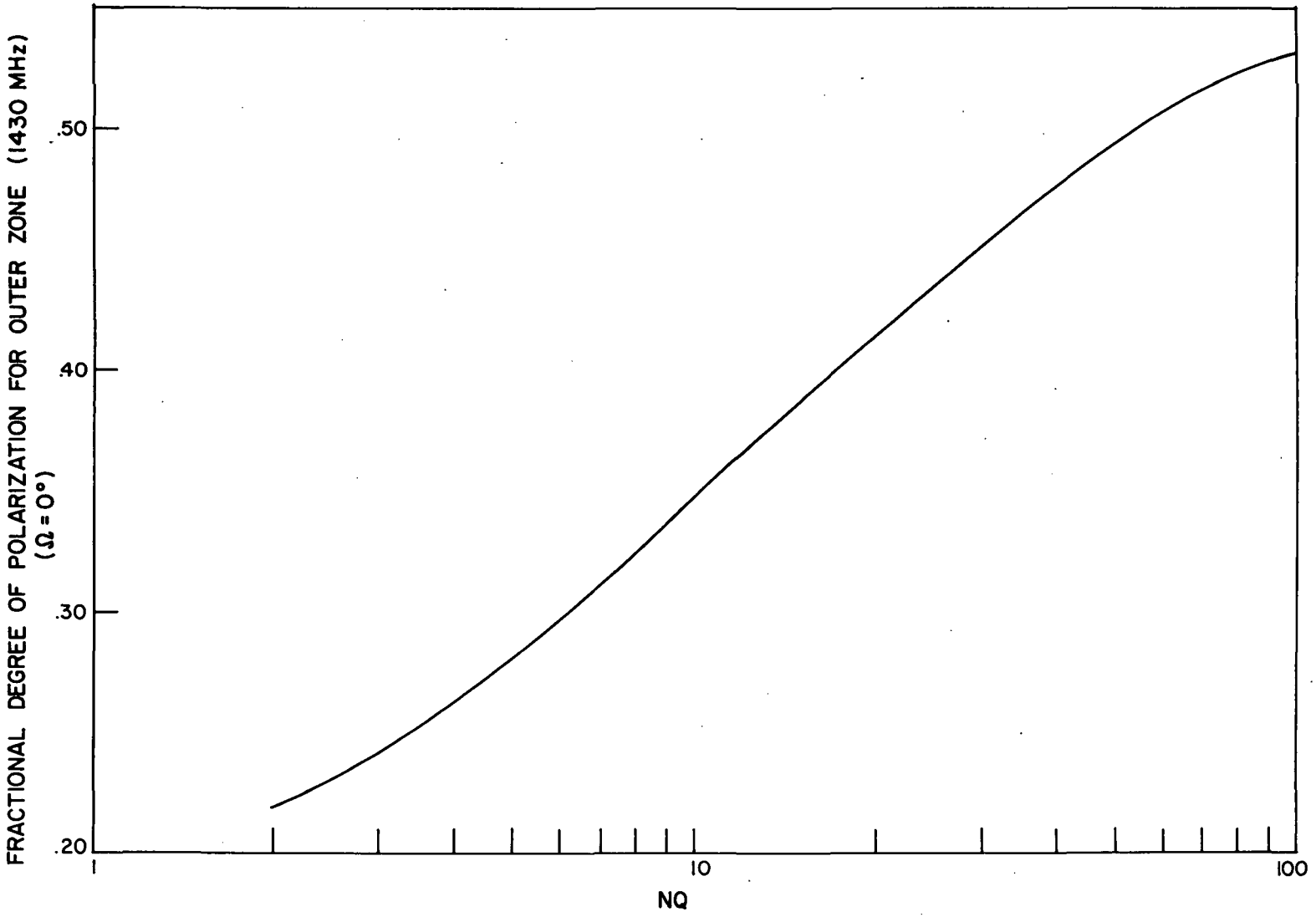

Figure 23. The degree of polarization increases rapidly with increasing NQ, that is, with an increasing contribution to the emission from a population of electrons largely confined to the magnetic equator ($\sin^{60} \alpha_e$).

asymmetry for NQ = 4. It is convenient to define a quantity Δ such that

$$\Delta = \frac{F(\theta_0 = 83^\circ)_N - F(\theta_0 = 83^\circ)_S}{F(\theta_0 = 90^\circ)} \quad , \tag{81}$$

where θ_0 is the zenomagnetic colatitude of the Earth and N and S stand for the northern and southern magnetic colatitudes, respectively. Roberts (1965) found $\Delta = 0.034$ at 2650 MHz.

Figure 22 shows Δ as a function of NQ. Δ increases with increasing NQ since the effect of the occultation on a distribution of particles confined to the magnetic equator (compare the intensities at $\Omega = 0^\circ$ and $\Omega = 180^\circ$ in Table 7) is much greater than the same effect on an isotropic distribution.

The variation of the degree of polarization at a frequency of 1430 MHz with increasing anisotropy is shown in Figure 23 for a uniform distribution of particle energies.

Table 8 shows the flux density spectra obtained for each monoenergetic ($\Delta u' = 10$) distribution of electrons in the outer zone. The numbers represent the ratio of the flux density at 1430 MHz to that received at frequency f.

As expected, the spectrum is generally flat except at the extremes of high and low energy. Also the peak in the spectrum moves towards higher frequencies with increasing energy. It should be noted that the shape of the spectrum is a very slowly varying function of the equatorial pitch-angle distribution of the electrons, i.e., of the anisotropy factor NQ. Also, the spectrum is essentially independent of the intensity profile chosen for the outer zone (See below, the inner zone).

TABLE 8

INTENSITY SPECTRA FROM MONOENERGETIC ELECTRON DISTRIBUTIONS (OUTER ZONE)

	f(MHz)							
u'	100	400	600	800	1000	1430	2000	3000
10	0.01	0.08	0.15	0.25	0.64	1.00	2.50	9.23
20	0.11	0.29	0.41	0.54	0.84	1.00	1.66	3.35
30	0.26	0.42	0.53	0.65	0.88	1.00	1.36	2.14
40	0.44	0.53	0.62	0.72	0.91	1.00	1.30	1.82
50	0.63	0.64	0.71	0.78	0.93	1.00	1.23	1.64
60	0.82	0.75	0.79	0.83	0.95	1.00	1.18	1.51
70	1.01	0.84	0.85	0.88	0.96	1.00	1.13	1.38
80	1.17	0.92	0.91	0.92	0.97	1.00	1.10	1.29
90	1.31	0.99	0.96	0.96	0.98	1.00	1.07	1.21
100	1.44	1.04	1.00	0.99	0.99	1.00	1.04	1.15
110	1.55	1.09	1.04	1.01	1.00	1.00	1.02	1.10
120	1.64	1.13	1.07	1.03	1.00	1.00	1.01	1.06
130	1.72	1.17	1.09	1.05	1.01	1.00	1.00	1.03
140	1.79	1.20	1.11	1.06	1.01	1.00	0.99	1.00
150	1.85	1.22	1.13	1.07	1.01	1.00	0.98	0.98
160	1.90	1.24	1.14	1.08	1.02	1.00	0.97	0.96
170	1.94	1.26	1.16	1.09	1.02	1.00	0.96	0.94
180	1.98	1.28	1.17	1.10	1.02	1.00	0.96	0.93
190	2.01	1.29	1.18	1.11	1.02	1.00	0.95	0.92
200	2.04	1.31	1.19	1.11	1.03	1.00	0.95	0.91
210	2.06	1.32	1.19	1.12	1.03	1.00	0.94	0.90
220	2.09	1.33	1.20	1.12	1.03	1.00	0.94	0.89
230	2.11	1.34	1.21	1.13	1.03	1.00	0.94	0.88
240	2.12	1.35	1.21	1.13	1.03	1.00	0.93	0.87
250	2.14	1.36	1.22	1.13	1.03	1.00	0.93	0.87

It is immediately apparent that to produce the high frequency bend in the spectrum described on Page 63, i.e., for F(1430)/F(3000) = 1.5, we must sacrifice the bend on the low-frequency side and vice-versa; thus from Table 8, if we set F(1430)/F(3000) = 1.5, we read F(1430)/F(100) = 0.82. This problem persists as a direct consequence of the flatness of the derived spectrum. Thus, in comparison to the emission spectrum of a single relativistic electron, we find that the decline of the intensity above and below the maximum frequency of emission are both replaced by much softer curves.

A monoenergetic distribution at u' = 70 produces a maximum bend in the spectrum on the high frequency side and yet maintains a relatively flat spectrum towards the low frequency side. This distribution is shown as configuration B in Figure 24. Distribution A represents the best numerical solution which will reproduce this same spectrum. Since it is more physically plausible than a monoenergetic configuration, A is taken as the most desirable distribution of electron energies in the outer zone.

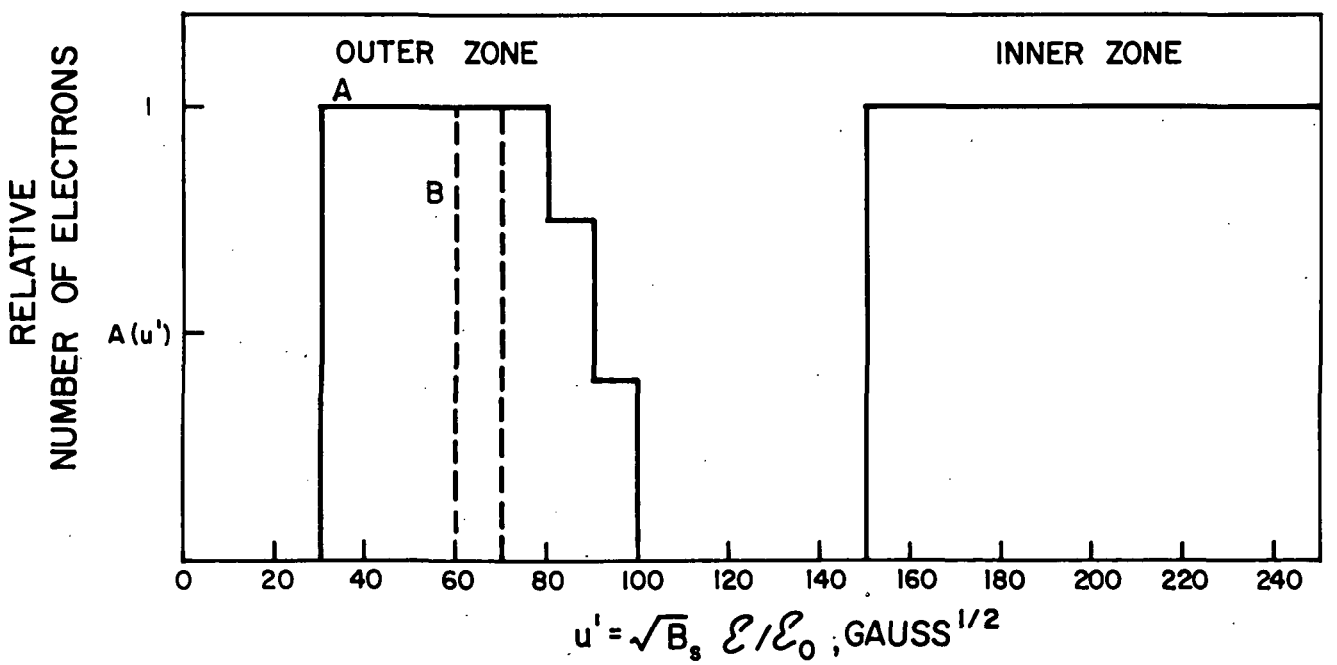

Figure 24. Electron energy distributions.

Figure 25 shows the spectrum of the degree of polarization in the outer zone for the energy distributions (A) and (B). This spectrum was derived for the particular anisotropic distribution a = 2 and b = 4 in Equation (80). Varying NQ will change the magnitude of the degree of polarization in the manner shown in Figure 23 for f = 1430 MHz. At higher frequencies, the rate of change of P with NQ becomes less pronounced. However, the actual shape of the polarization spectrum remains generally independent of the energy distribution and NQ. This shape is in marked contrast with the observed spectrum of the degree of polarization of the synchrotron component shown in Figure 18 which showed a peak near 0.30 at 1430 MHz and declined slowly at higher frequencies.

The polarization spectrum of the non-thermal component, $P_{NT}(f)$, shown in Figure 18, was derived from the expression

$$P_{NT}(f) = P_0(f) \left[\frac{F_{NT}(f) + F_T(f)}{F_{NT}(f)} \right] , \qquad (82)$$

where $P_0(f)$ is the fractional polarization of the total emission (Figure 17); $F_{NT}(f)$ is the non-thermal flux density which is obtained by subtracting the flux density of the thermal emission at frequency f, $F_T(f)$, from that of the total emission (Figure 16a). The thermal spectrum, $F_T(f)$, becomes quite uncertain at low frequencies (See Page 63).

The pattern in Figure 18 contradicts the result obtained by Legg and Westfold (1968), for a monoenergetic isotropic distribution of electrons moving in a uniform magnetic field which shows an increase of the degree of polarization with increasing frequency. If we refer to Figure 11 we see that this same trend occurs for a given L-shell. For constant L, u decreases with increasing frequency [See Equation (68)].

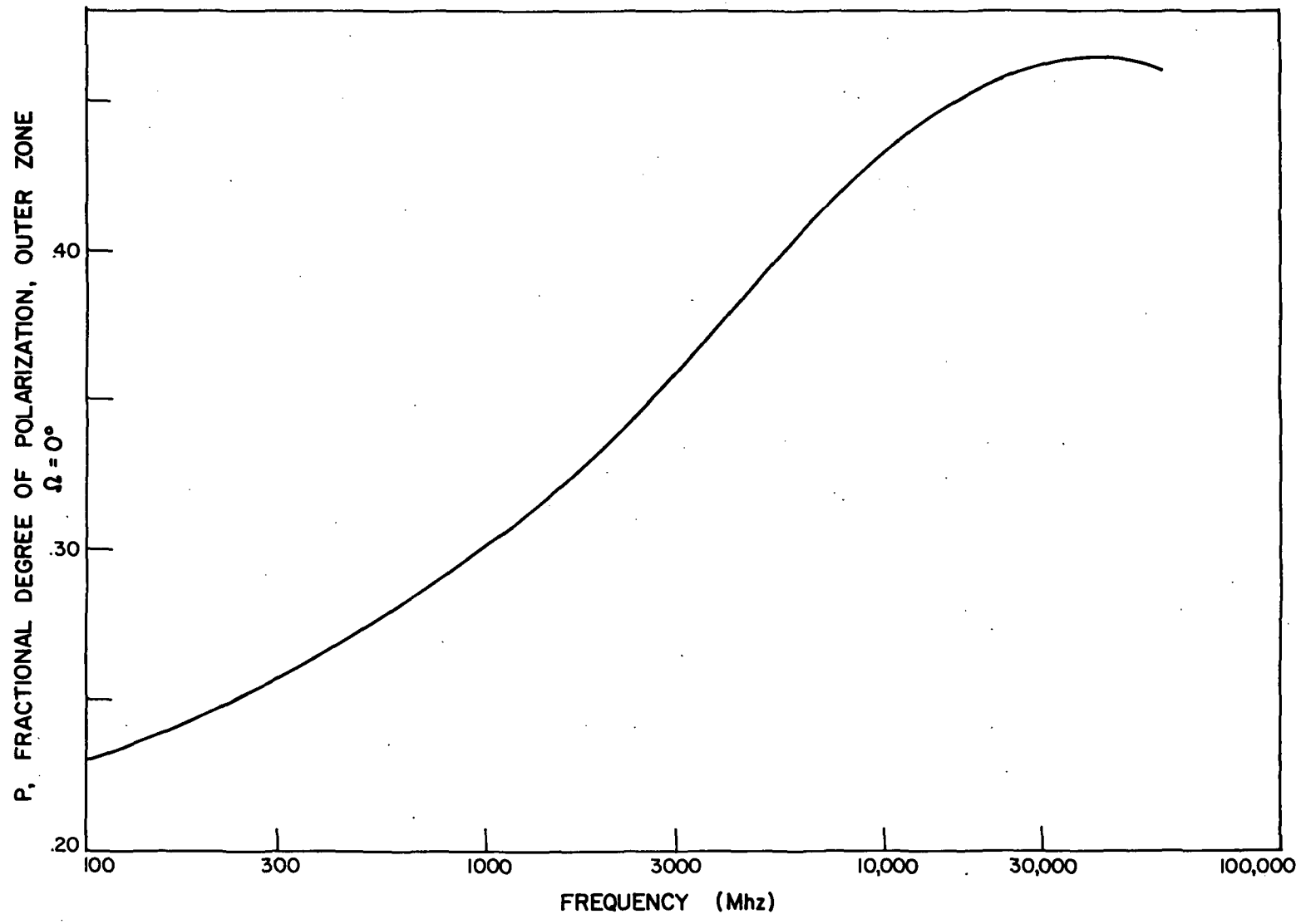

Figure 25. Polarization spectrum for the outer zone. Note the steady increase with frequency in contrast to the synchrotron spectrum of Figure 18.

Therefore, the degree of polarization increases with increasing frequency for an isotropic distribution of electrons in a dipolar field (it is nearly constant at 0.56 for a pitch-angle distribution confined to the magnetic equator as shown in Chapter II, Section H-2). However, the observations show that the high frequency emission originates from a region close to the planet, and certainly at less than L = 2 for 10000 MHz. It is immediately obvious from Figure 11 that we may anticipate a drop in the degree of polarization at the high frequencies if the emission at these frequencies is relatively more intense in the region $1 < L < 2$ than in the outer zone.

3. The inner zone

The three-dimensional effect of the dipolar field geometry on an isotropic distribution of electrons produces a region of minimum degree of polarization when the electric vectors received from different ϕ-planes show a maximum difference in phase. In the particular case of the Jovian magnetic field, this minimum occurs near L = 1.6 showing a general decrease in the range between L = 1.1 and L = 2. (See Chapter II, Section H-1). This region ($1.1 \leq L < 2$), described as the inner zone, is responsible for most of the high frequency emission from the radiation belts. It will be demonstrated now that the properties of the electrons in this zone are quite different from the properties of those in the outer zone.

To describe the intensity of emission at 1430 MHz in the inner zone we use a curve with the same form as Planck's distribution. This function is used here as a convenient mathematical approximation, particularly since the position of the maximum is easily determined by a single parameter (Wien's law).

$$F(L) = 1.20/[y^5(e^B - 1) \quad , \tag{83}$$

where $y = 2.1 - L$,

$B = 1.50/(y*k)$,

and k is a constant that determines the position of the maximum intensity. For L greater than the position of the maximum intensity, the distribution falls rapidly to nearly zero at L = 2. For L less than the position of the maximum intensity, it declines slowly towards L = 1.1. For k = 1, .8, .6, .5, and .4, the peak occurs at L = 1.8, 1.7, 1.6, 1.5, and 1.3, respectively.

Table 9 gives the spectra obtained for different monoenergetic distributions of electrons in the inner zone with an intensity distribution at 1430 MHz which peaks at L = 1.6 (k = 0.6).

The spectra are nearly independent of the position of the maximum of intensity within the inner zone and also nearly independent of the particular intensity profile chosen. As might be anticipated from Figure 15, there is relatively more emission at higher frequencies for a given energy than in the outer zone; the effect becomes more pronounced with increasing energy.

Figure 26 shows the fractional degree of polarization at 10000 MHz as a function of the electron energy for an isotropic pitch-angle distribution in the inner zone. Clearly, if we require the inner zone to contribute the weakly polarized component of the synchrotron emission at high frequencies, we can predict that the energy of the electrons in the inner zone is such that $u' > 100$.

4. The parameters of the combined zones

We have the following expressions for the spectrum and the fractional degree of polarization of the combined emission from the two zones

TABLE 9

INTENSITY SPECTRA FROM MONOENERGETIC ELECTRON DISTRIBUTIONS (INNER ZONE)

	f(MHz)							
u'	100	400	600	800	1000	1430	2000	3000
10	0.01	0.05	0.09	0.20	0.54	1.00	4.01	27.40
20	0.18	0.29	0.38	0.50	0.81	1.00	1.79	4.39
30	0.66	0.61	0.67	0.74	0.91	1.00	1.35	2.17
40	1.14	0.88	0.87	0.89	0.96	1.00	1.15	1.50
50	1.46	1.05	1.00	0.98	0.99	1.00	1.06	1.22
60	1.69	1.15	1.08	1.04	1.00	1.00	1.01	1.08
70	1.84	1.21	1.12	1.07	1.01	1.00	0.98	1.00
80	1.94	1.26	1.16	1.09	1.02	1.00	0.96	0.95
90	2.02	1.30	1.18	1.11	1.02	1.00	0.95	0.92
100	2.07	1.32	1.20	1.12	1.03	1.00	0.94	0.89
110	2.11	1.34	1.21	1.13	1.03	1.00	0.94	0.88
120	2.14	1.36	1.22	1.14	1.03	1.00	0.93	0.86
130	2.17	1.38	1.24	1.15	1.03	1.00	0.93	0.86
140	2.20	1.39	1.25	1.15	1.04	1.00	0.92	0.85
150	2.22	1.40	1.25	1.16	1.04	1.00	0.92	0.84
160	2.24	1.40	1.26	1.16	1.04	1.00	0.92	0.83
170	2.25	1.41	1.26	1.16	1.04	1.00	0.91	0.83
180	2.26	1.41	1.26	1.16	1.04	1.00	0.91	0.82
190	2.27	1.41	1.26	1.17	1.04	1.00	0.91	0.82
200	2.27	1.42	1.27	1.17	1.04	1.00	0.91	0.81
210	2.29	1.42	1.27	1.17	1.04	1.00	0.91	0.81
220	2.29	1.42	1.27	1.17	1.04	1.00	0.91	0.81
230	2.27	1.42	1.27	1.17	1.04	1.00	0.91	0.81
240	2.33	1.42	1.27	1.17	1.04	1.00	0.90	0.80
250	2.29	1.42	1.27	1.17	1.04	1.00	0.91	0.80

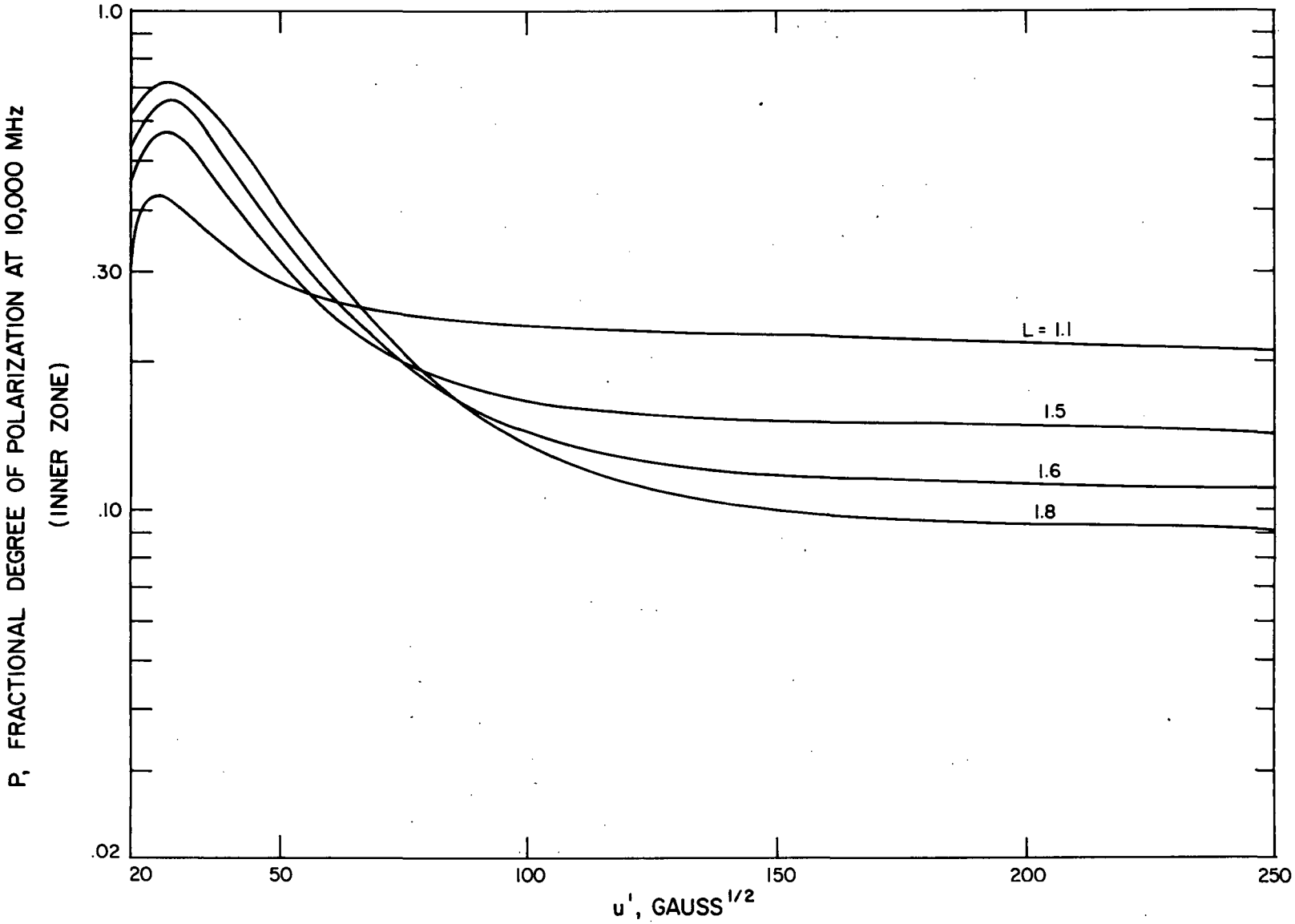

Figure 26. Fractional degree of polarization at 10000 MHz for emission from the inner zone as a function of electron energy. The labels indicate the value of L corresponding to peak intensity in Equation (83). As will be seen later, in order to reproduce the bend in the polarization spectrum of Figure 18 we must have u' > 100.

$$F(1430)/F(f) = \frac{[1/x + R/y]}{1 + R} \quad , \tag{84}$$

and

$$P_{NT}(f) = \frac{[zP_i + P_o]}{z + 1} \tag{85}$$

where $F(1430)/F(f)$ is the net flux density at frequency f.

The subscripts i and o refer to the inner and outer zones, respectively,

$$x = F_i(1430)/F_i(f) \ ,$$

$$y = F_o(1430)/F_o(f) \ ,$$

$$z = \frac{1}{R}\left[\frac{y}{x}\right] \ ,$$

and $R = F_o(1430)/F_i(1430)$, the ratio of the flux at 1430 MHz of the outer and inner zones.

We also define a spectral index between the frequencies of 1000 and 3000 MHz:

$$C = \frac{1}{\log 3} \log \left[\frac{F(3000)}{F(1000)}\right] \quad . \tag{86}$$

In combining the two zones, we assume the electrons in the outer region to have the energy distribution which produces a maximum spectral curvature at high frequencies, i.e., Figure 24A. The particles in the inner zone have a uniform energy distribution with either an upper cut-off energy [u'(MAX)] or a lower cut-off energy [u'(MIN)]. In Figure 27 we see how the quantities P_{NT}, C, and the ratio F(1430)/F(100) vary with the energy distribution in the inner zone. These plots were derived for R = 2.5 (the ratio of the intensities of the outer and inner zones) but vary slowly with changing R (See Table 11). From the graph we see that a solution which is most compatible with the observations is one for

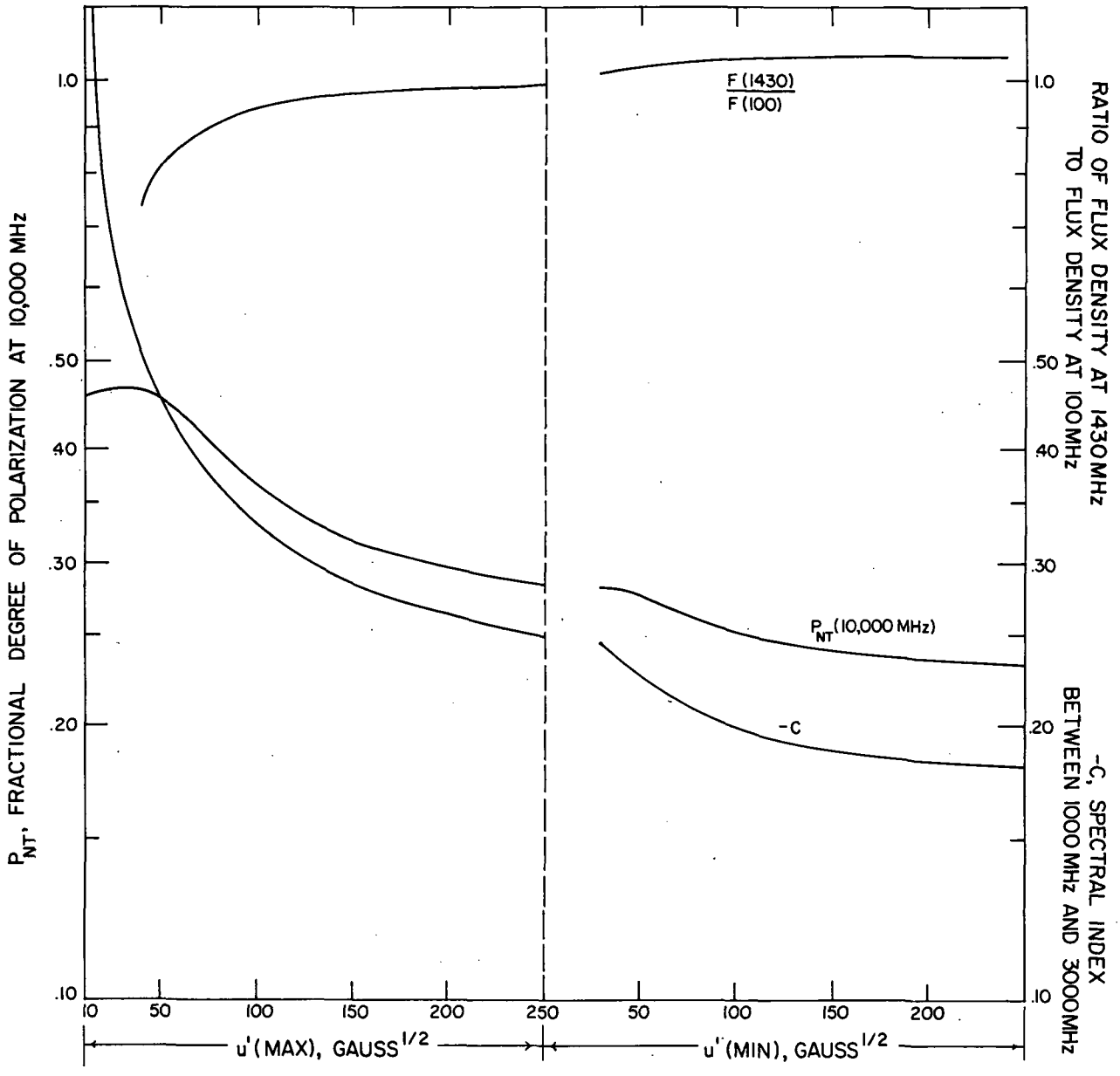

Figure 27. The observables P_{NT}(10000 MHz), C and F(1430)/F(100) as a function of uniform energy distributions with upper and then lower energy cutoffs. It is not possible to define a precise energy distribution for the inner zone and only cutoffs can be invoked. From Figures 26 and 27 we obtain the energy distribution for the inner zone, shown in Figure 24B.

which the inner zone has a low energy cut-off u'(MIN),and the value of this quantity is about 150. At this point the observables are: $C \sim -0.2$ (giving F(1430)/F(3000) = 1.2), F(1430)/F(100) $\sim$ 1.05, and P_{NT}(10000 MHz) = 0.24. The combined intensity and polarization spectra for this particular case are shown in Figures 28 and 29, respectively. The peak in the intensity spectrum occurs in the range 400 - 600 MHz and shows slightly less curvature in both directions than the synchrotron component derived in Figure 16a (Dickel, Degioanni and Goodman, 1970).

The polarization spectrum now shows a decrease at high frequencies (as opposed to Figure 25 for the outer zone only). A peak of about 0.30 occurs near f = 1430 MHz. The agreement with the derived spectrum of Figure 18 is good at high frequencies but the decline at lower frequencies is less marked. However, as shown in Figure 17, the observed degree of polarization of the total emission at 100 MHz has a large error. This discrepancy is discussed later.

To obtain the fractional polarization of the total emission we must consider the large thermal component to the observed intensity at high frequencies. The spectrum of the total flux density from Jupiter is shown in Figure 16a and the approximate flux densities at several frequencies are tabulated in Table 10. From this we can obtain the fractional polarization spectrum of the total intensity shown in Figure 30.

The spectrum of the total non-thermal intensity using the model just derived is compared with the observed spectrum on the transparent overlay on Figure 16b. The effect of the decreased curvature in the spectrum of the non-thermal component at high frequencies is to lower the thermal component at 3000 MHz from $\sim$2.9 FU to $\sim$2.0 FU. Thus it appears that the thermal and non-thermal models best agree if the

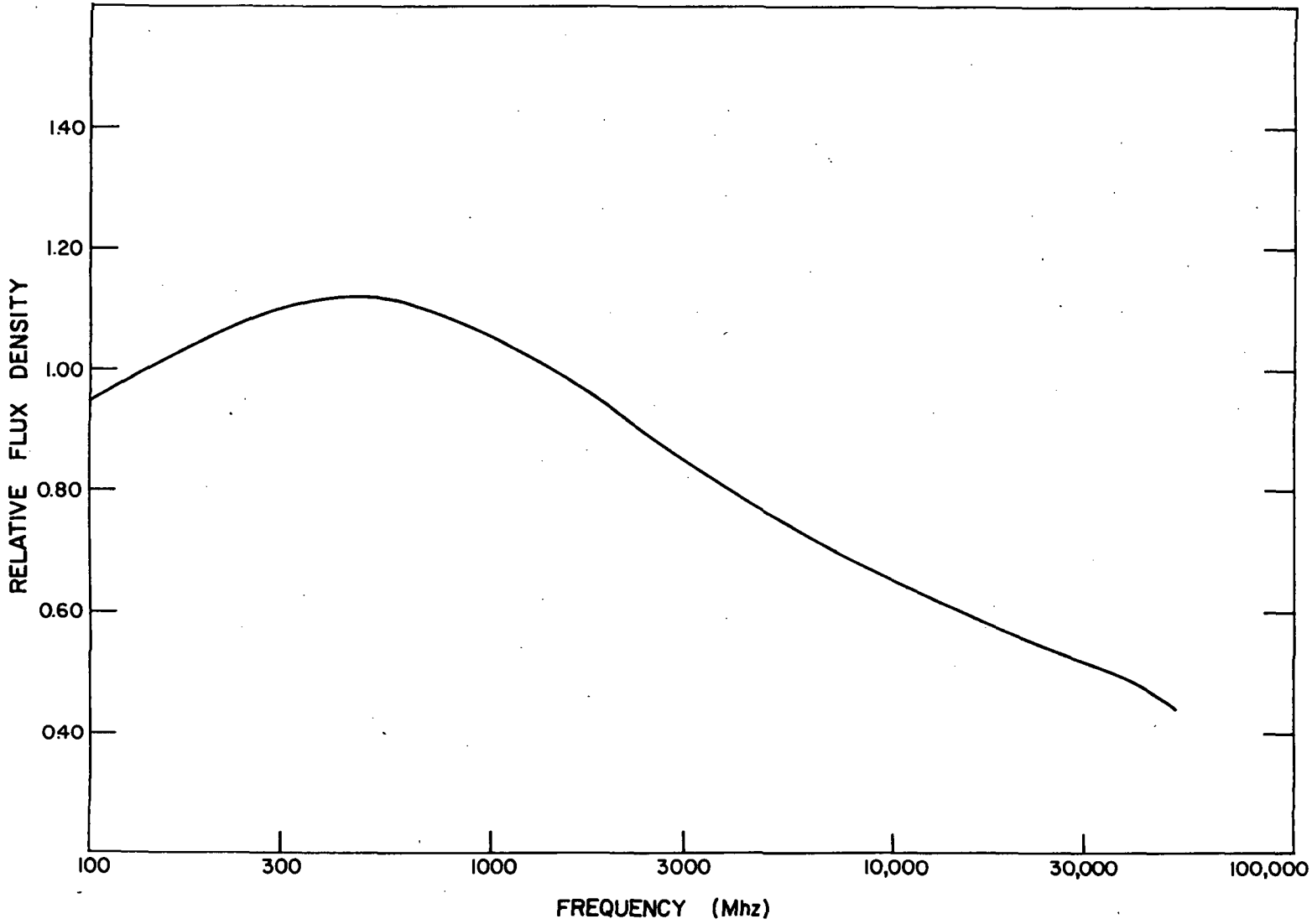

Figure 28. The intensity spectrum for the model described in Chapter III, Section B. Plotted is the mean flux density ratio. The ratio is taken relative to the flux density at f = 1430 MHz.

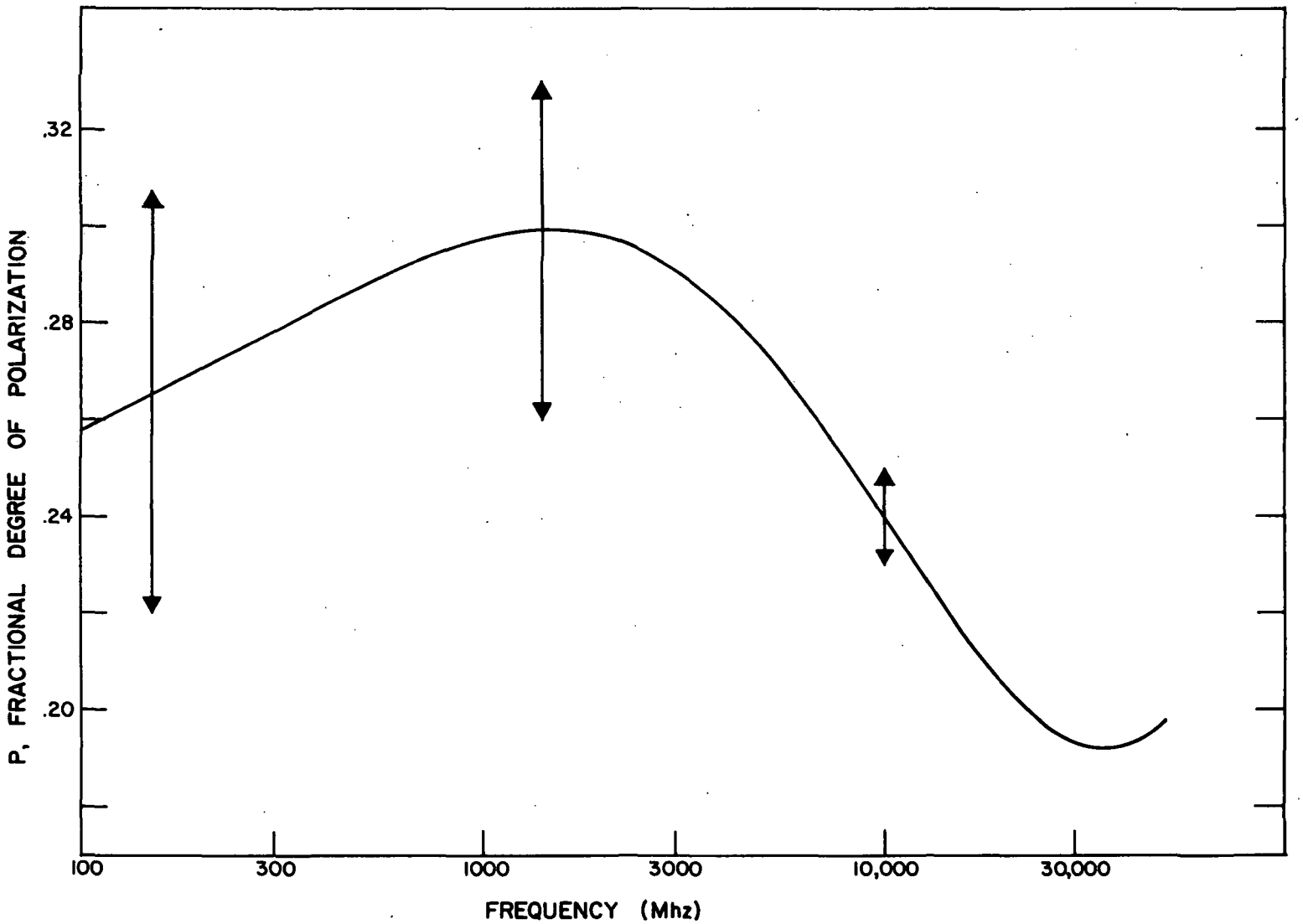

Figure 29. Polarization spectrum for the model described in Chapter III, Section B. Plotted is the mean degree of polarization. The arrows indicate the range of variation with the rotation of the planet.

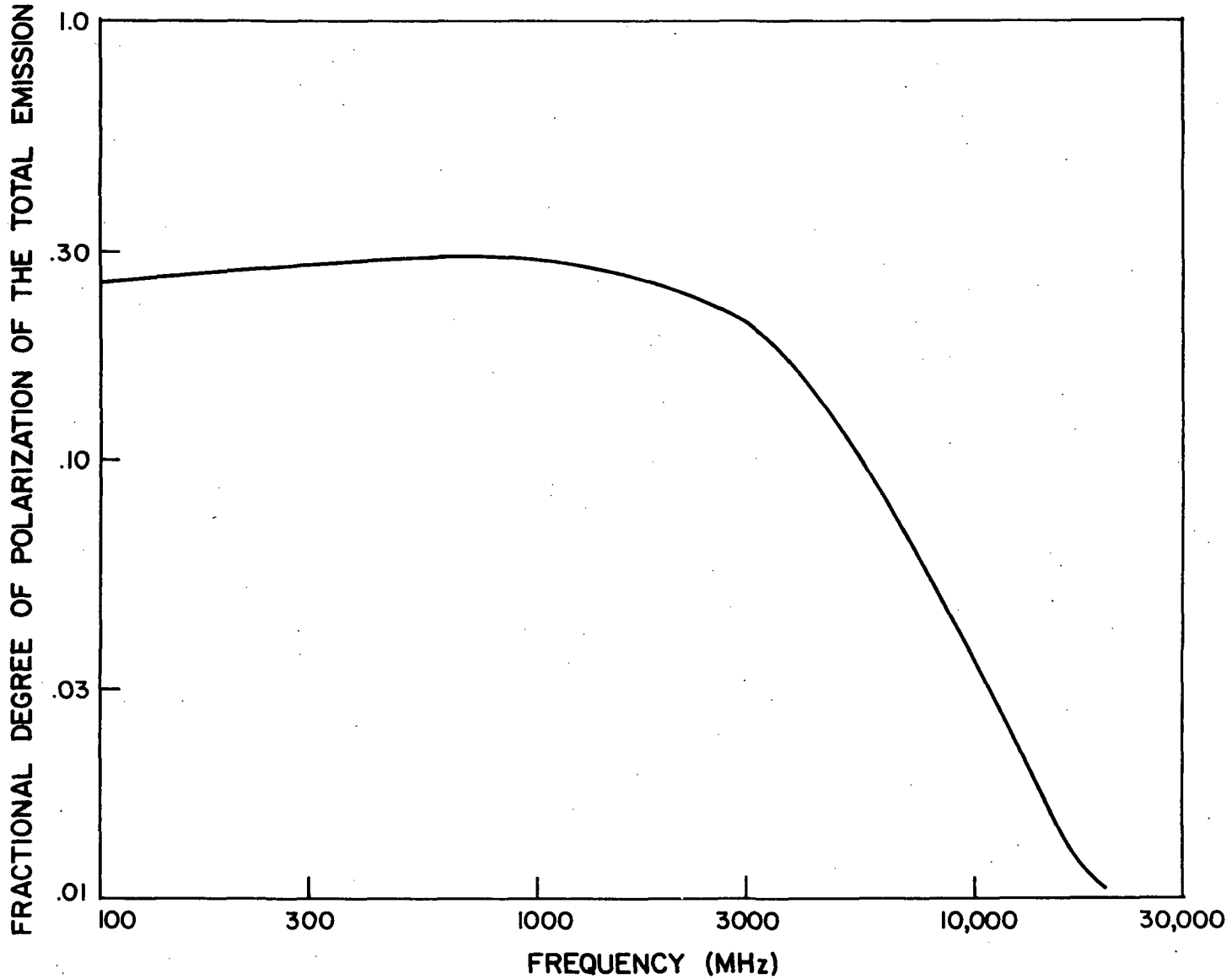

Figure 30. Fractional degree of polarization of the total emission. This curve was obtained from Figure 29 and the values listed in Table 10. For $f \leq 800$ MHz the thermal contribution was completely neglected.

TABLE 10

APPROXIMATE FLUX DENSITY RECEIVED FROM JUPITER, NORMALIZED TO A PLANETARY DISTANCE OF 4.04 A.U.
(These values were read from Figure 16a. Below 800 MHz the thermal component was considered negligible and the non-thermal emission from from Figure 28 was equated to the total emission.)

f(MHz)	Flux Density (FU)
800	7.0
1000	7.2
1430	7.3
2000	7.4
3000	7.5
5000	12.0
10000	28.0
20000	60.0
30000	155.0
50000	500.0

emission from the disk at 3000 MHz derived by Berge (1966) is reduced by a factor of 0.7, i.e., T_{η}(3000 MHz) = 180° K. This lower temperature would require a larger mixing ratio of ammonia than has usually been assumed in the Jovian atmosphere but does not seem to violate any other observable parameters. The fractional abundance of NH_3 will become about 0.003 (Goodman, 1969).

The results described above assume an intensity ratio R = 2.5. Table 11 shows the effect of a changing R on the observable parameters C, P_{NT}(1000 MHz) and F(1430)/F(100).

TABLE 11

OBSERVABLE PARAMETERS AS A FUNCTION OF THE MODEL PARAMETER R = $F_o(1430)/F_i(1430)$

R	C	P_{NT}(10000 MHz)	F(1430)/F(100)
0.5	+0.072	0.16	1.48
1.0	+0.038	0.19	1.26
1.5	-0.107	0.21	1.16
2.0	-0.154	0.23	1.10
→ 2.5	-0.190	0.24	1.06
3.0	-0.215	0.25	1.03
4.0	-0.252	0.28	0.99
5.0	-0.278	0.29	0.97
6.0	-0.296	0.31	0.96
7.0	-0.310	0.32	0.94
8.0	-0.321	0.33	0.94
10.0	-0.337	0.35	0.92
20.0	-0.371	0.39	0.90

Furthermore, in the model we assumed that the pitch-angle distribution in the inner zone is isotropic, (NQ = 0) for L < 1.8. The effect of increasing NQ on the parameters C, P_{NT} and F(1430)/F(100) is shown in Table 12.

TABLE 12

OBSERVABLE PARAMETERS AS A FUNCTION OF NQ (R = 2.5)

NQ	C	P_{NT}(10000 MHz)	F(1430)/F(100)
0	-0.190	0.24	1.06
0.5	-0.190	0.31	1.06
1.0	-0.190	0.33	1.06
1.5	-0.190	0.34	1.06
2.0	-0.190	0.35	1.06

Thus we have obtained two zones in the Jovian radiation belt which probably are distinct since they possess rather different energy distributions and electron pitch-angle distributions. Now, we must rule out the possibility that the two zones may not represent two distinct belts but are one belt with a gradient of energy which increases towards the planet.

For this purpose we constructed five different models of the outer zone with five energy gradients of decreasing steepness across the zone. The inner limit was defined by the energy distribution in the inner zone and the outer limit in the farthest L shell (or the one with the lowest energy distribution) was varied towards increasing levels. The twenty resultant spectra for the four different outer limits are given in Table 13.

These results must be compared with Table 8 for the outer zone.

TABLE 13

EFFECT ON THE INTENSITY SPECTRUM OF INTRODUCING A GRADIENT OF ENERGY ACROSS THE OUTER ZONE

(There are five models of decreasing steepness in the energy gradient between the outer and innermost shell. Four different energy distributions mark the boundary at the outermost shell. The spectra become flatter as we move towards flatter gradients, i.e., down the column for a given model, and for all gradients, they become flatter as we raise the energy level in the outermost shell, i.e., from Model 1 through 4.)

		f(MHz)							
MODEL		100	400	600	800	1000	1430	2000	3000
1	1	0.87	0.83	0.86	0.89	0.93	1.00	1.10	1.27
	2	0.89	0.86	0.88	0.91	0.94	1.00	1.08	1.22
	3	0.92	0.88	0.90	0.92	0.95	1.00	1.07	1.18
	4	0.98	0.92	0.93	0.94	0.96	1.00	1.05	1.13
	5	1.05	0.96	0.96	0.97	0.98	1.00	1.03	1.08
2	1	1.14	0.96	0.95	0.95	0.97	1.00	1.05	1.16
	2	1.17	0.98	0.96	0.96	0.97	1.00	1.04	1.13
	3	1.19	0.99	0.98	0.97	0.98	1.00	1.03	1.10
	4	1.24	1.03	1.00	0.99	0.99	1.00	1.02	1.06
	5	1.30	1.06	1.03	1.01	1.00	1.00	1.01	1.03
3	1	1.41	1.07	1.02	1.01	1.00	1.00	1.02	1.08
	2	1.42	1.08	1.03	1.01	1.00	1.00	1.01	1.06
	3	1.44	1.10	1.04	1.02	1.01	1.00	1.01	1.04
	4	1.48	1.12	1.06	1.03	1.01	1.00	1.00	1.02
	5	1.53	1.15	1.08	1.04	1.02	1.00	0.99	0.99
4	1	1.62	1.16	1.09	1.05	1.02	1.00	1.00	1.02
	2	1.63	1.17	1.09	1.05	1.03	1.00	0.99	1.01
	3	1.65	1.18	1.10	1.05	1.03	1.00	0.99	0.99
	4	1.67	1.20	1.11	1.06	1.03	1.00	0.98	0.98
	5	1.71	1.22	1.12	1.07	1.04	1.00	0.97	0.96

Clearly, the spectra derived for the distributions with a gradient are all significantly flatter than the case when a single energy distribution is assigned to the entire zone. Thus, the spectrum would get flatter and the disagreement with Berge's thermal model would be significantly enhanced. In conclusion, the solution that gives a double-belt system with distinct energy distributions shows much better agreement with the observations.

The effect upon the longitudinal variation of the intensity of combining the two zones is shown in Figure 31. The amplitude of the variation is decreased compared to what we find for the outer zone alone since the inner zone with NQ = 0 contributes no oscillation. In fact, the intensity simply declines from $\Omega = 0^{o}$ to $\Omega = 180^{o}$ because of the increasing amount of occultation by the planet, as shown in Table 4. Furthermore, since we add a zone which undergoes a stronger occultation effect (since it is closer to the planet) we expect the asymmetry described on Page 63 to be enhanced. This is shown in Figure 21b, where we see that the quantity Δ for the combined zones is increased.

Table 14 shows the range in the oscillations of the degree of polarization.

TABLE 14

VARIABILITY IN THE DEGREE OF POLARIZATION AS A FUNCTION OF FREQUENCY

f(MHz)	$P_{NT}(\Omega = 0^{o})$	$P_{NT}(\Omega = 90^{o})/P_{NT}(\Omega = 0^{o})$
100	0.21	1.40
400	0.24	1.38
600	0.25	1.33
800	0.25	1.31
1430	0.26	1.26
2000	0.27	1.23
3000	0.27	1.19
5000	0.26	1.14
10000	0.23	1.08
30000	0.19	1.05

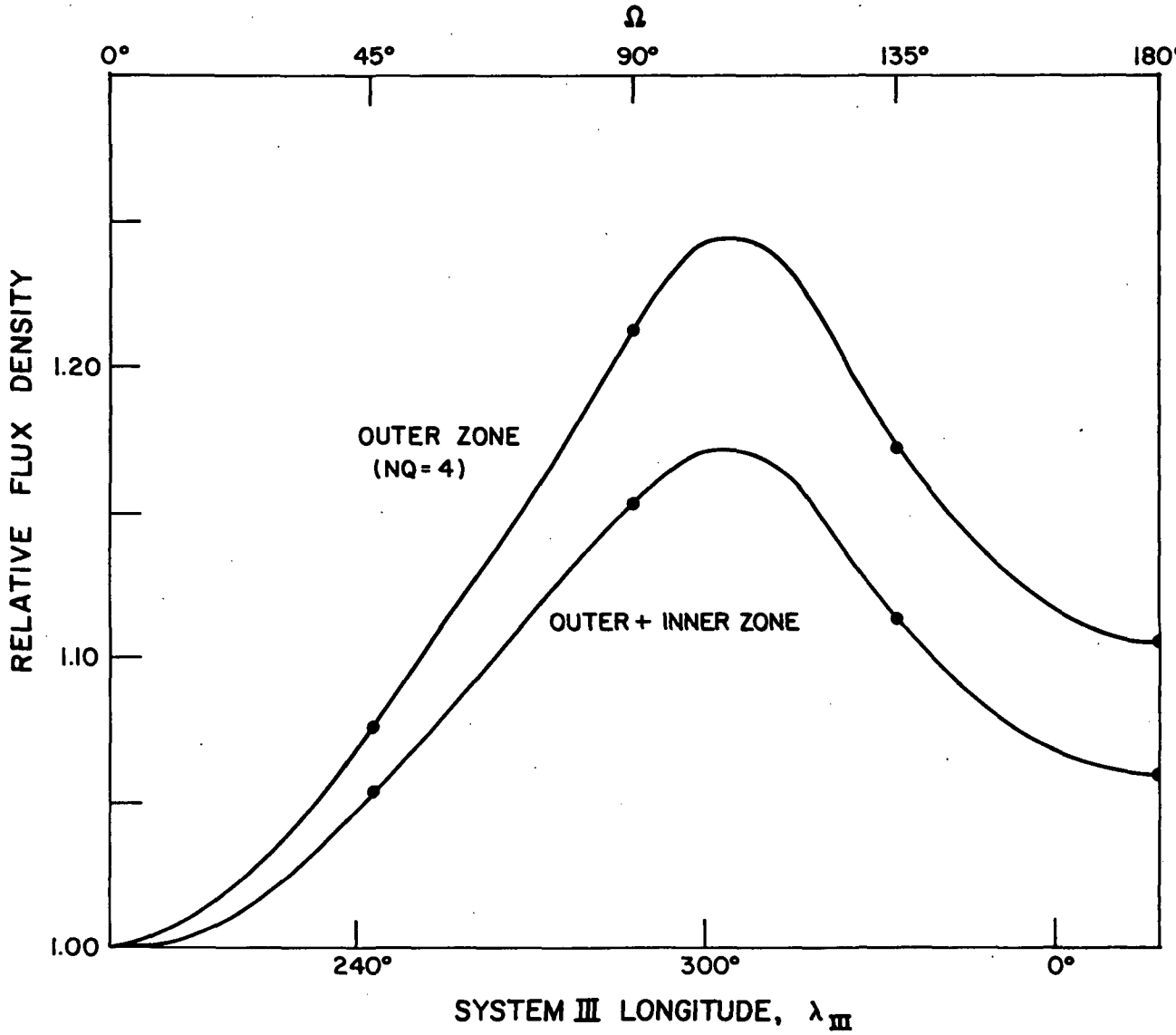

Figure 31. Effect upon the longitudinal variation of the intensity of combining the two zones. Note that the abscissa begins with $\Omega = 0^{o}$ in this graph. This is done to demonstrate most clearly how the relative decline in the intensity in the range $\Omega = 105^{o}$ to 180^{o} is maintained and, in fact, enhanced by combining the two zones. This results in the enhanced asymmetry as shown in Figure 21 (b).

Clearly, the results predict a greater variability for the degree of polarization at low frequencies than at higher ones.

Figure 32a shows the frequency dependence of the total range of the longitudinal variation in intensity for the combined belts. There is a gradual decline with increasing frequency. This is expected since the emission at high frequencies comes from a region where the pitch-angle distribution of the electrons is isotropic and where occultation by the planet is a maximum (See discussion on Page 76). The solution obtained is adequate since the variability in the range from 1000 to 5000 MHz is of the order of 10 percent. According to some authors (Dickel, 1965), the decline in variability may be somewhat too fast towards higher frequencies. To change the amplitude of the oscillations, the distribution of NQ must be altered. This, however, will rapidly affect the polarization spectrum (See Table 11). There exists another approach, however, that will increase the variability at higher frequencies. This consists in replacing the intensity profile in the inner zone [given in Equation (83)] by a narrow distribution of uniform intensity between $L = 1.5$ and $L = 1.8$. Such a square pulse raises the amplitude of the oscillations, particularly at higher frequencies (Figure 32b), because there is no contribution of emission from the highly occulted component of radiation when $L < 1.5$.

If we replace the intensity profile of the inner belt with the square pulse for $1.5 \leq L \leq 1.8$ and keep the same distribution as above for the outer belt [Equations (77a) and (77b)], we obtain the oscillations of the combined belts at 2600 MHz and 600 MHz shown in Figure 33b. The curve at 2600 MHz includes a thermal contribution of 20 percent at that frequency. For comparison, the observations at these same frequencies

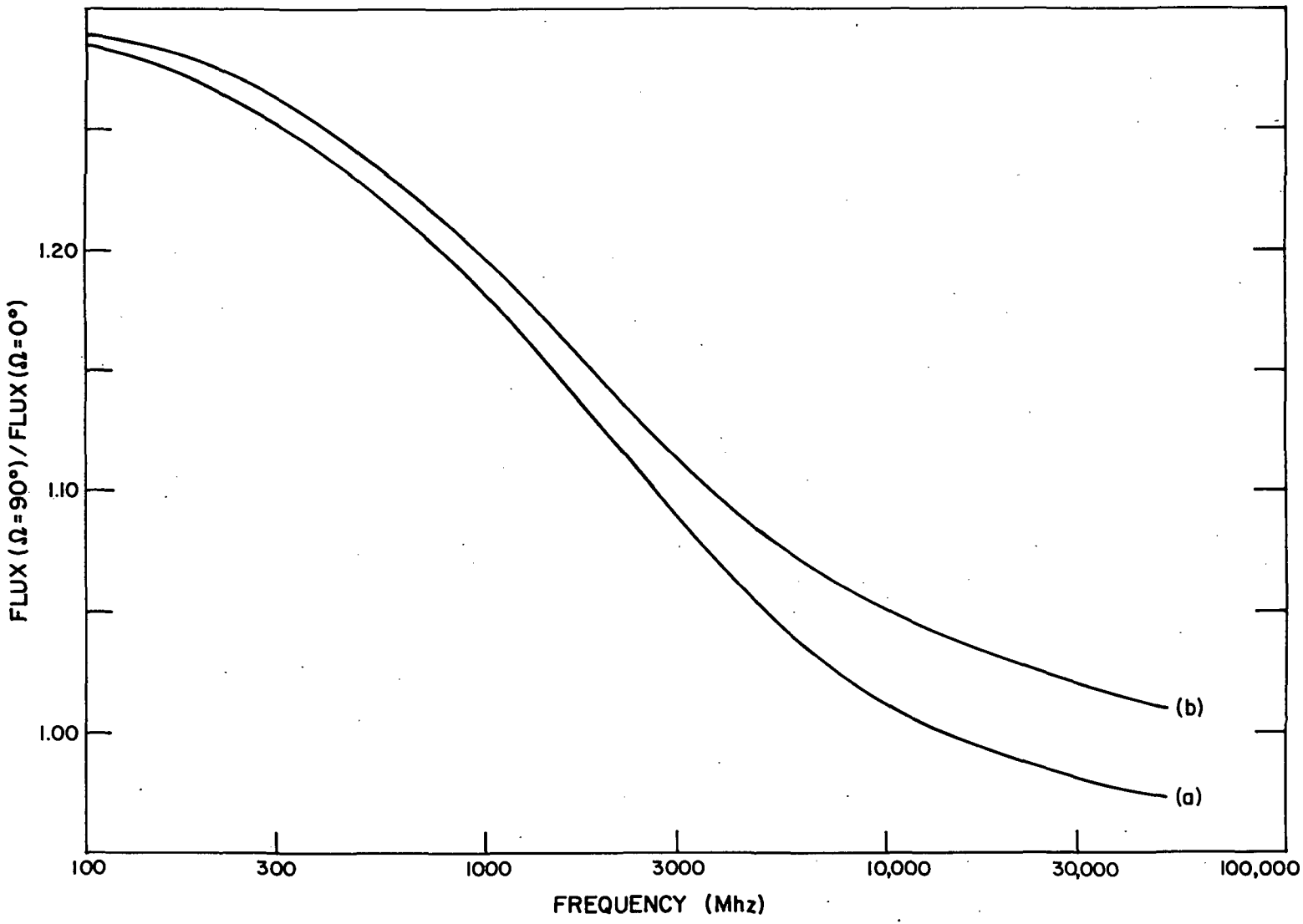

Figure 32. (a) The total range of the longitudinal variation in intensity as a function of frequency. The outer belt is described by Equations (77a) and (77b) and the inner belt by Equation (83) with k = 0.6 (See Page 70).
(b) Total range of the longitudinal variation in intensity as a function of frequency. The outer belt is described by Equations (77a) and (77b) and the inner belt consists of a uniform profile between L = 1.5 and L = 1.8.

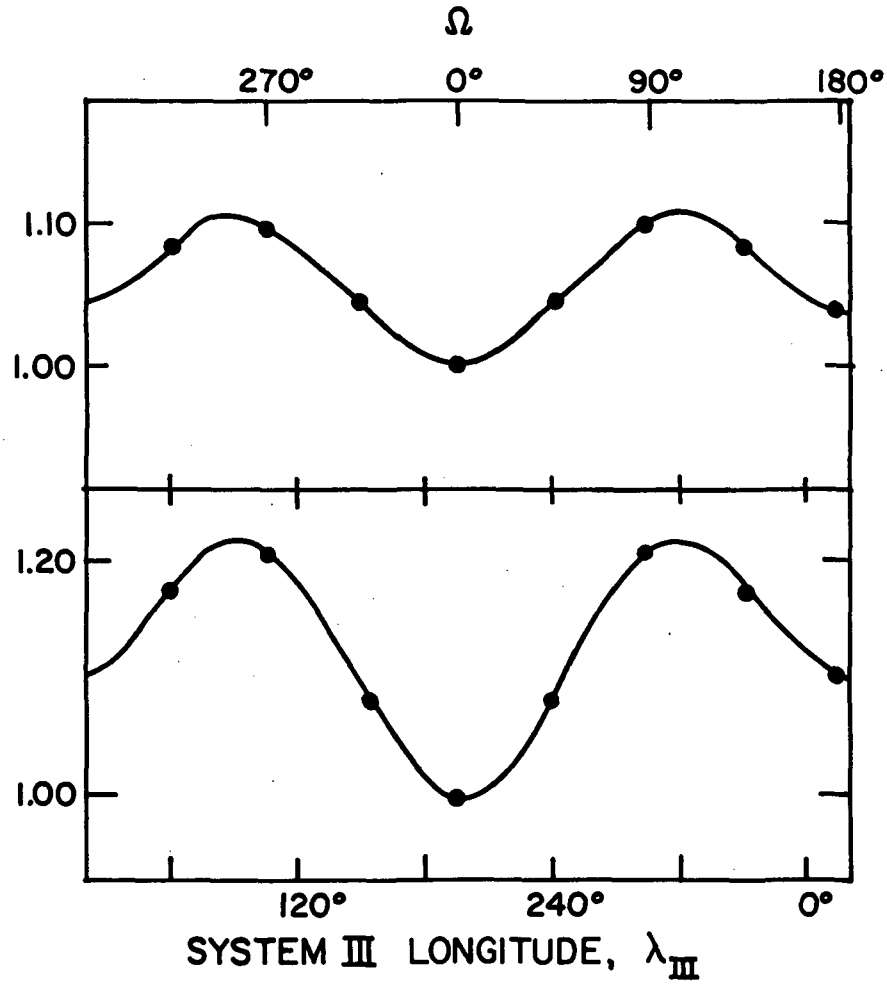

Figure 33b. (Overlay) Predicted variations at 2600 MHz and 600 MHz for the present model with the inner zone consisting of a square pulse between L = 1.5 and L = 1.8. The oscillations at 2600 MHz contain a non-variable contribution of 20 percent from the thermal component.

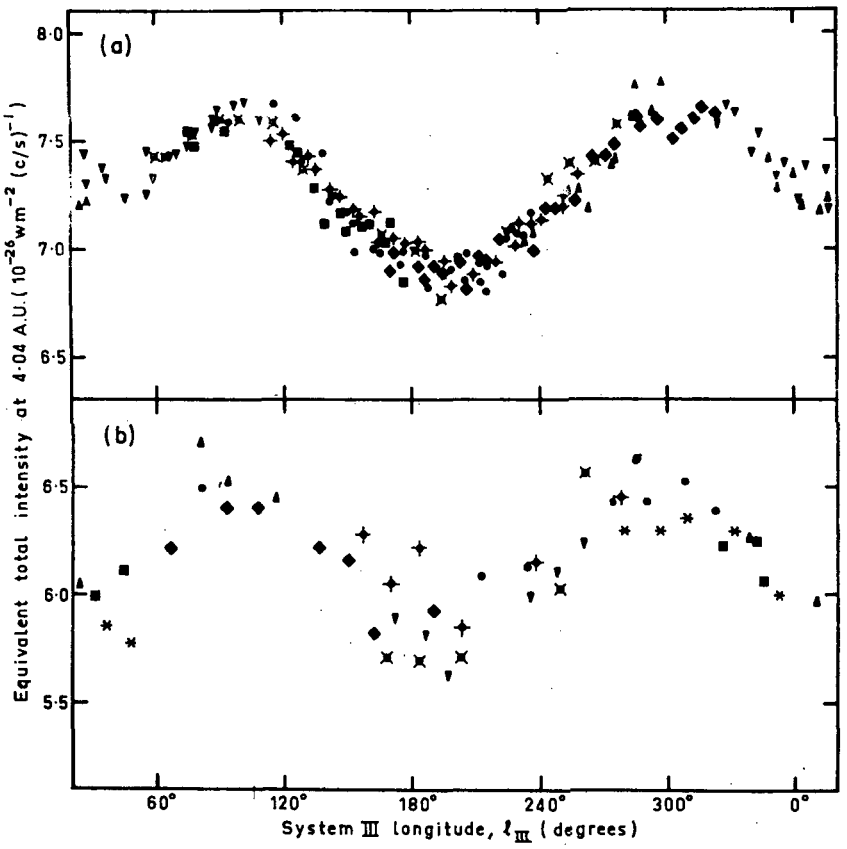

Figure 33a.
Reproduced from Roberts and Ekers (1968). Longitudinal oscillations of the observed brightness of Jupiter at 2650 MHz (top graph) and 620 MHz (bottom graph).

by Roberts and Ekers (1968) are also shown. The predicted results (overlay) emphasize the fact that the oscillations are enhanced at the lower frequency and yet the fit to the observations is reasonable at both frequencies.

Figures 34 and 35 show the intensity profiles of the emission at 100, 1430 and 15000 MHz for the rotational angles $\Omega = 0^{\circ}, 45^{\circ}, 90^{\circ}, 135^{\circ}$ (corresponding to $\lambda_{III} = 198^{\circ}, 243^{\circ}, 288^{\circ}, 333^{\circ}$). When $\Omega = 0^{\circ}$, the profile at 1430 MHz is that given by Equations (77a), (77b) and (83) for the outer and inner zones, respectively. There is complete symmetry of components (1) and (2) at this angle (See Page 43). Clearly the extent of the emission decreases with increasing frequency and the structure of the inner belt becomes very prominent at 15000 MHz. With increasing rotational angle Ω the two components become asymmetric with the west (component 1) greater than the east (component 2). This is particularly true for the inner belt. The asymmetry is, of course, reversed for rotation angles $180^{\circ} < \Omega \leq 360^{\circ}$. Thus the sequence of asymmetry produced by the occultation follows the same pattern as that described by Branson's (1968) "hot spot." It should be emphasized, however, that Figures 34 and 35 do not represent projections of the radiation belts in the plane of the sky but instead are plots of the intensity integrated over a single shell at the radial distance L as a function of L. A true projection map would require summation over all the shells along the line of sight rather than the single shell solution as outlined by Chang and Davis (1962).

Figure 36 shows the profiles of the degree of polarization for the cases NQ = 2.5 and NQ = 4 in the outer zone (NQ = 0 in the inner zone). As expected the degree of polarization has a minimum near L = 1.5. Note

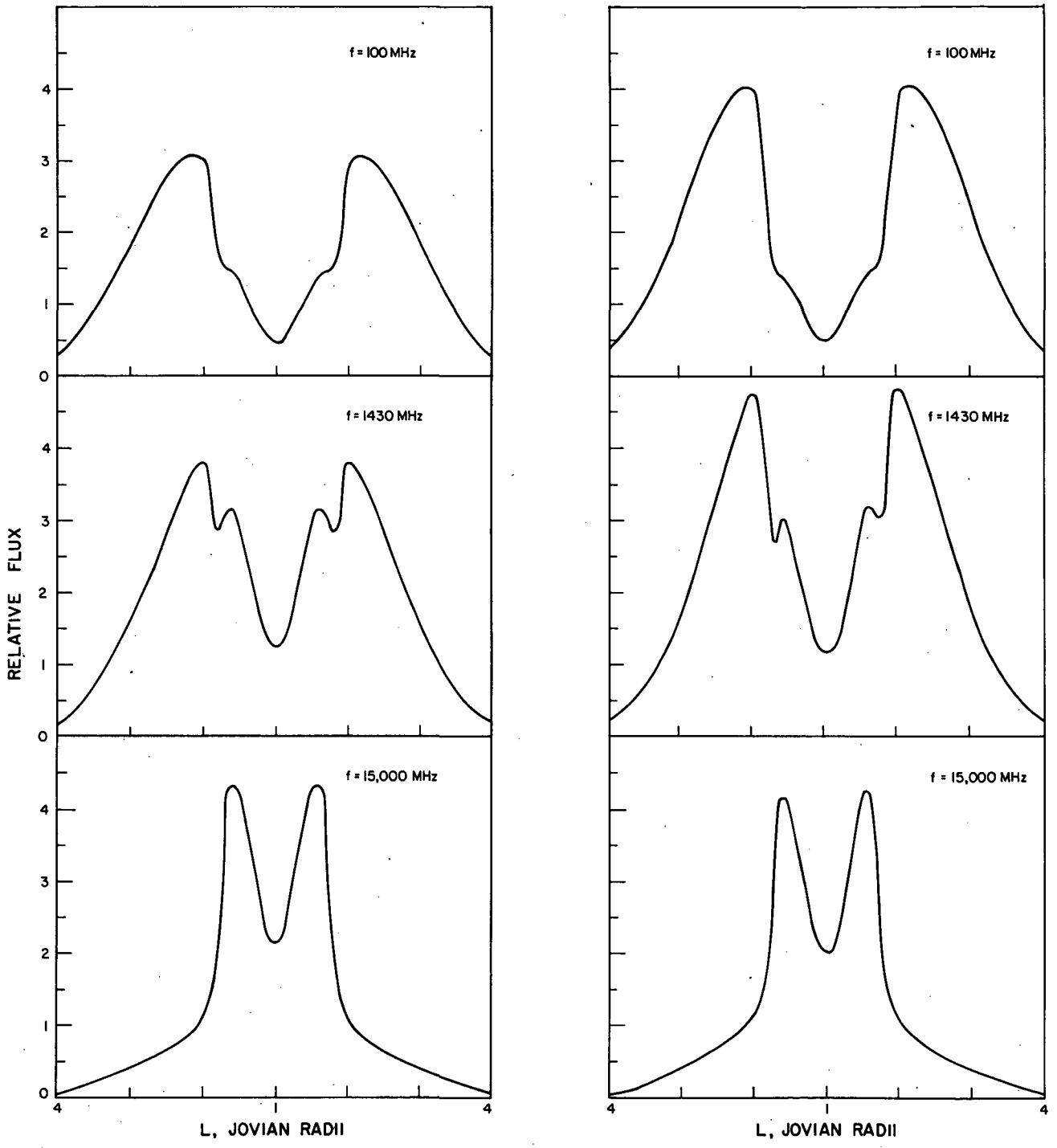

Figure 34. Intensity profiles for $\Omega = 0^{o}$ (left) and $\Omega = 90^{o}$ (right). Note how the extent of the emission varies with frequency (see discussion in the text).

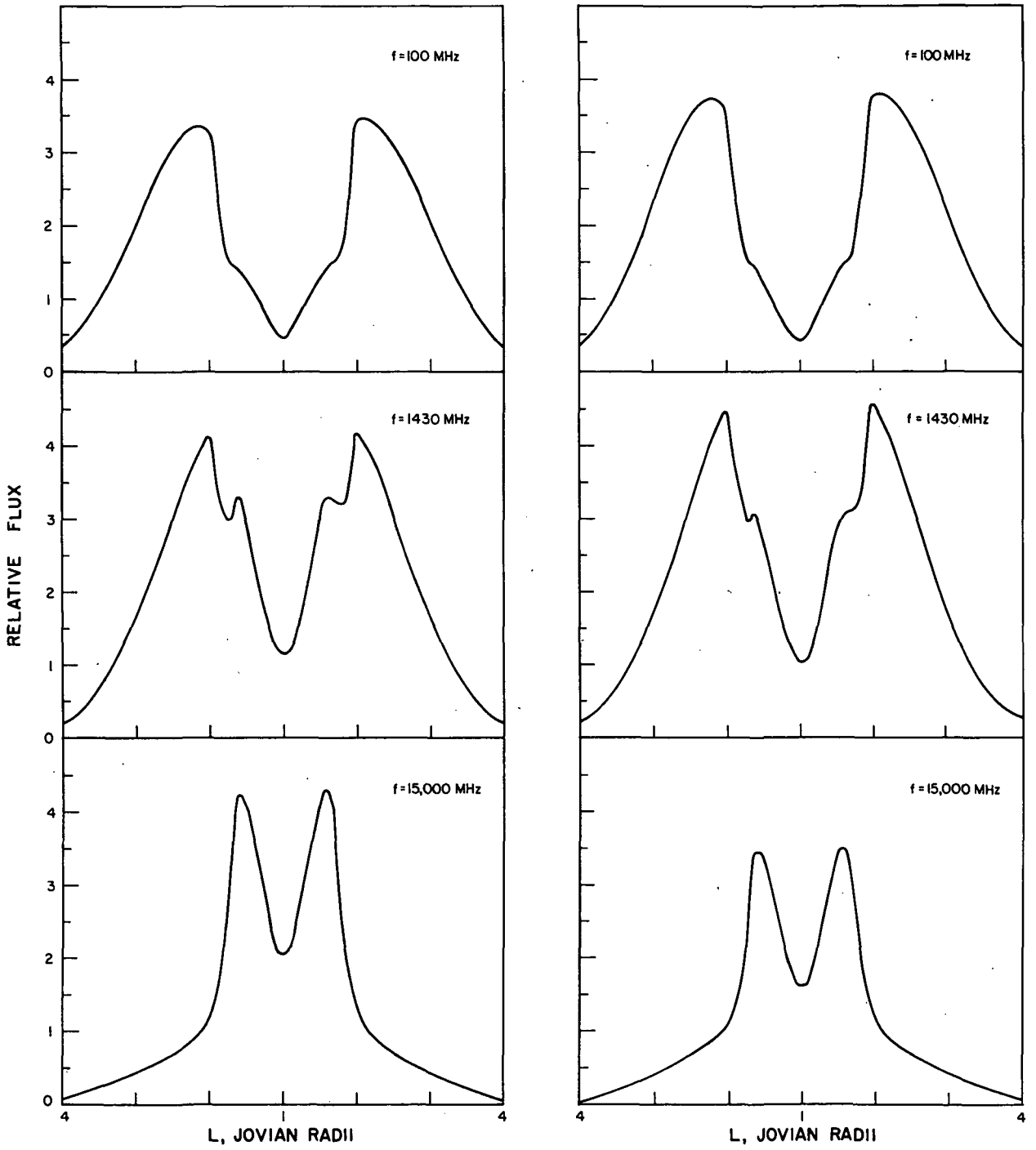

Figure 35. Intensity profiles for $\Omega = 45^{o}$(left) and $\Omega = 135^{o}$(right). Note how the extent of the emission varies with frequency (see discussion in the text).

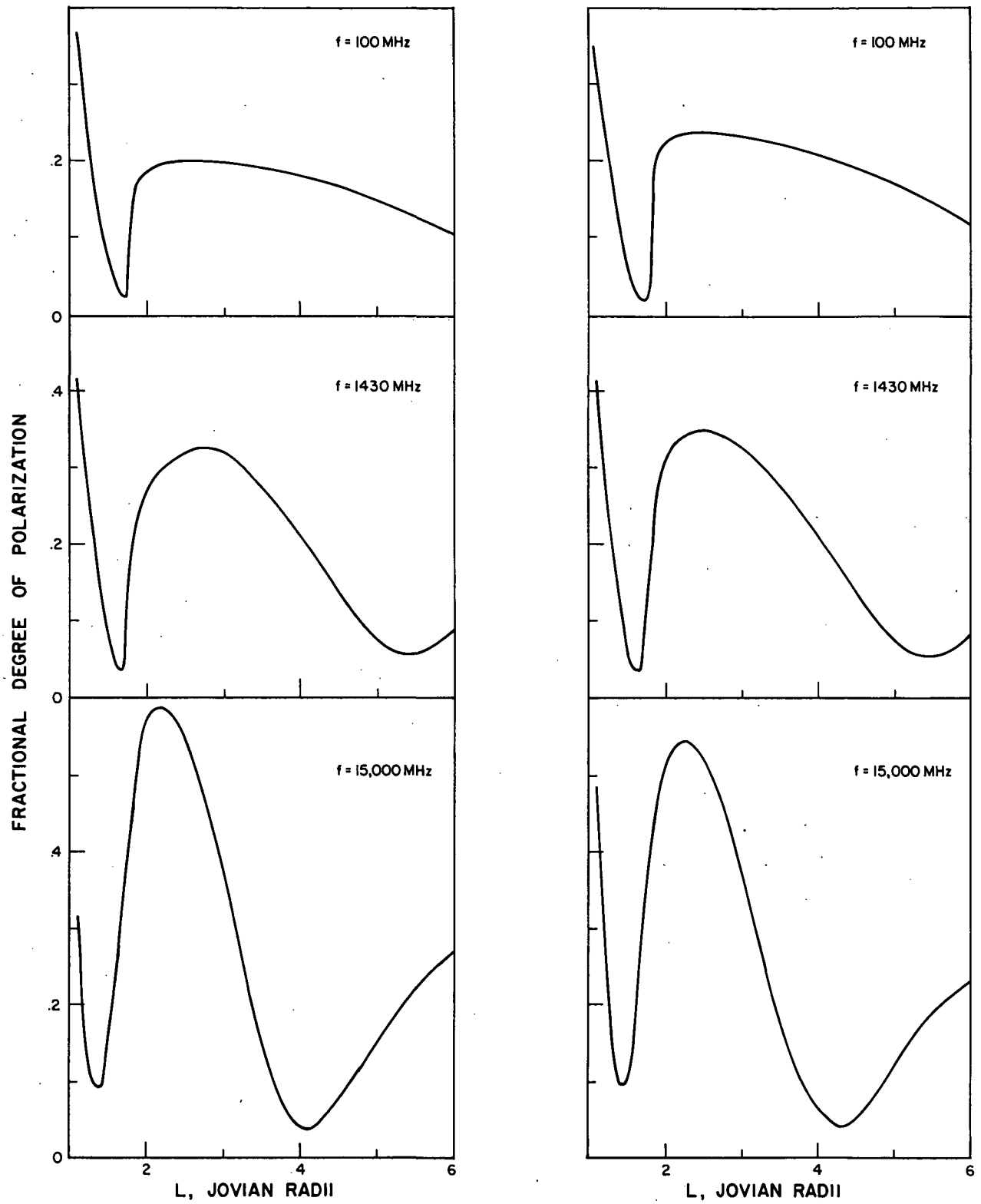

Figure 36. The profile of the fractional degree of polarization as a function of frequency, NQ = 2.5 (left) and NQ = 4.0 (right). Note that the minimum near L = 1.5 at 15000 MHz coincides with the maximum emission at that frequency in Figures 34 and 35. The degree of polarization in the outer zone is increased with increased NQ, as expected from Figure 23.

that this minimum coincides with the maximum of the intensity profile at 15000 MHz, i.e., the inner belt.

5. The density profile of the radiation belts and the B-L distribution of the electron flux

The purpose of this section is to obtain the radial dependence of the particle density and the latitude dependence of the electron flux in our model for the radiation belts. The density-dependent quantity $D(L) = B_S N(L)$ (where B_S is the equatorial surface field strength) can be solved from Equation (79). Figure 37 shows the resultant profile for the double zone system described in Sections B-2 and B-3. A power function that will fit this profile for $L > 2$ has the form

$$D(L) \propto L^{-3.7}.$$

Thus, we see that the number density of electrons along the equator falls approximately with the fourth power of the distance.

This result can be compared with the distribution of the thermal plasma in the outer region as derived in a model by Melrose (1967). He finds that the density falls off as BL^{-1} which in the equatorial plane is also proportional to L^{-4}. Thus, it appears that, at least for $L > 2$, the distance dependence of the equatorial plasma density is very similar for both the thermal particles and the relativistic electrons in the radiation belts.

Now, we want to obtain the dependence of the electron flux on distance and magnetic latitude. For this purpose, we use the standard B-L coordinate system (McIlwain, 1961). The expression for the omni-directional electron flux at the magnetic colatitude θ is

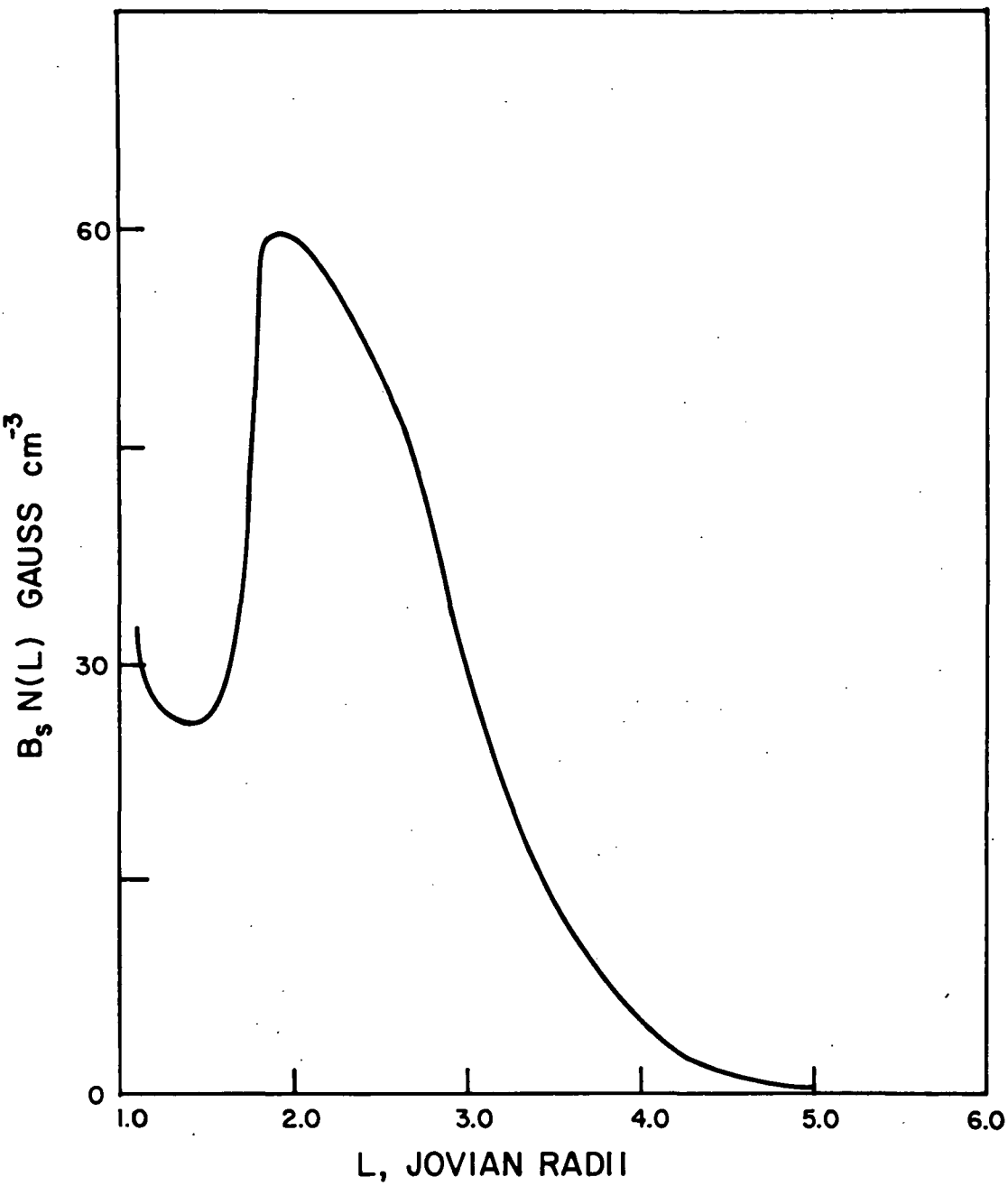

Figure 37. Profile of the particle density in the equatorial plane. B_S is the surface magnetic field. This result was obtained from the best solution of Equation (78) for the intensity profiles given in Equations (77a), (77b) and (83), and a pitch angle distribution for the particles given by Equation (80).

$$J(\theta) = \left[K_0 m_0 \int_{\alpha_e(MIN)}^{\alpha_e(\theta)} (4\pi \sin \alpha_e) d\alpha_e + K_{60} m_{60} \int_{\alpha_e(MIN)}^{\alpha_e(\theta)} (\sin^{60} \alpha_e) x (4\pi \sin \alpha_e) d\alpha_e \right]$$

$$N_o(L)\bar{v}_o \left[1 + \frac{N_i(L)\bar{v}_i}{N_o(L)\bar{v}_o} \right] \text{ cm}^{-2} \text{ sec}^{-1} \quad , \tag{87}$$

where $N_o(L)$ and $N_i(L)$ are the number densities in cm^{-3} for the outer and inner zones, respectively; $\bar{v}_o$ and $\bar{v}_i$ are their respective mean electron velocities in cm/sec.

$\alpha_e(\theta)$ is the equatorial pitch angle that corresponds to the mirror point at magnetic colatitude θ. We have, from Equation (58),

$$\sin \alpha_e(\theta) = \frac{\sin^2 \theta}{(1 + 3 \cos^2 \theta)^{1/4}} \quad . \tag{88}$$

Figure 38 shows the results for the intensity distribution from Equation (83) in the inner zone (of the same form as Planck's curve with a peak at L = 1.6), and the intensity distribution from Equations (77a) and (77b) in the outer zone. In Figure 39 are the results for a square pulse distribution in the inner zone for L = 1.5 to 1.8 (a distribution which increases the amplitude of the variability with longitude, particularly at high frequencies) and the same intensity profile for the outer zone [Equations (77a) and (77b)]. These figures show that in contrast to the radiation belts of the Earth, which have distinct peaks at L = 1.2 and L = 4.5 (Hess, 1968), the Jovian belts do not have such a distinct feature in the outer region; they do, however, show a distinct increase in electron flux for L < 2. This, of course, reflects the energy difference between the outer and inner zones. Furthermore, the electron flux in the Jovian belts is generally a factor of 1000 larger than for

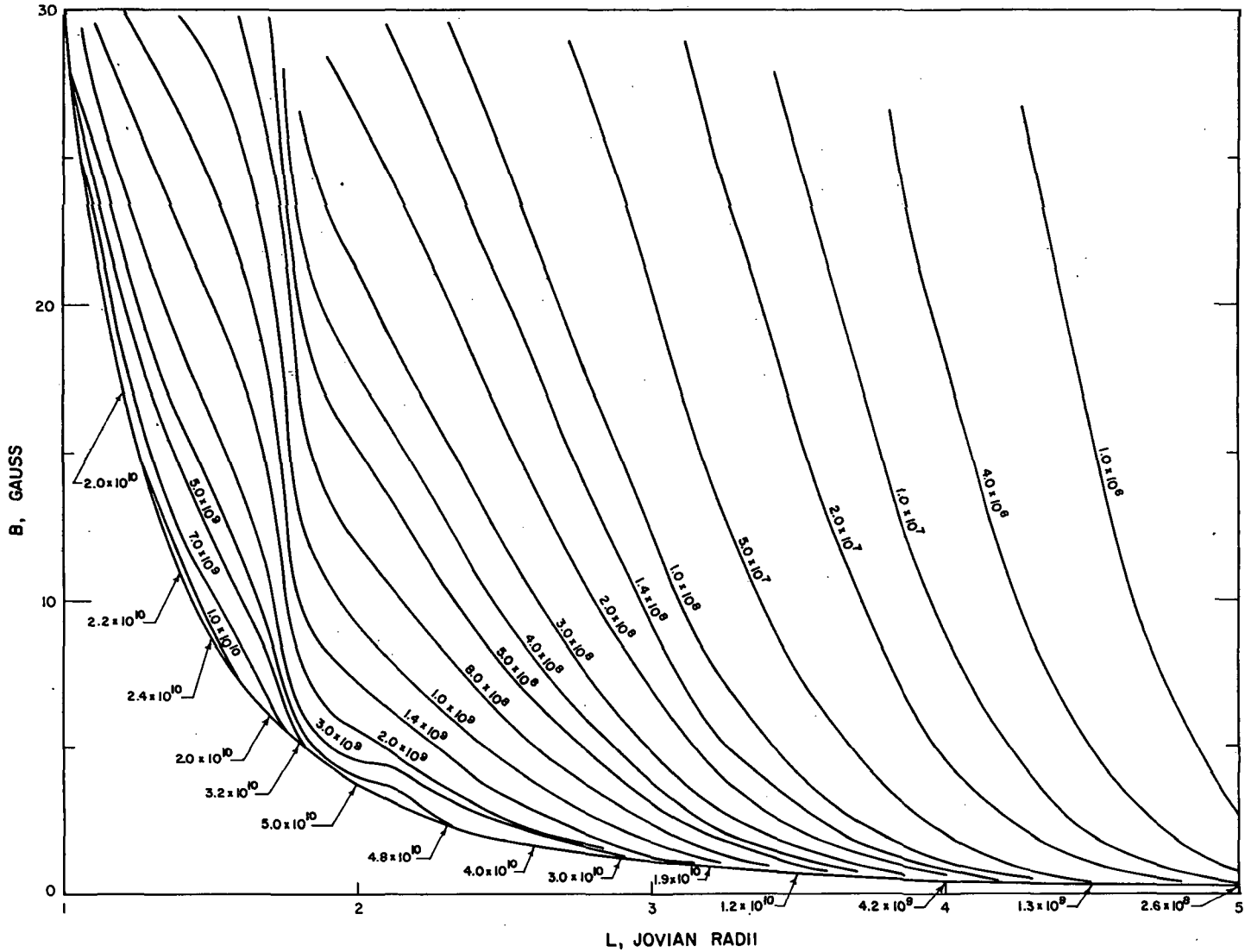

Figure 38. A B-L plot of the electron flux for an outer zone described by Equations (77a) and (77b) and the inner zone described by Equation (83) (with k = 0.6). The electron flux is in cm^{-2} sec^{-1}. Note the sudden increase in flux at the boundary of the inner and outer zones. A surface field of 30 Gauss is assumed (Warwick, 1963). Changing the value of B_S will not qualitatively affect the distribution.

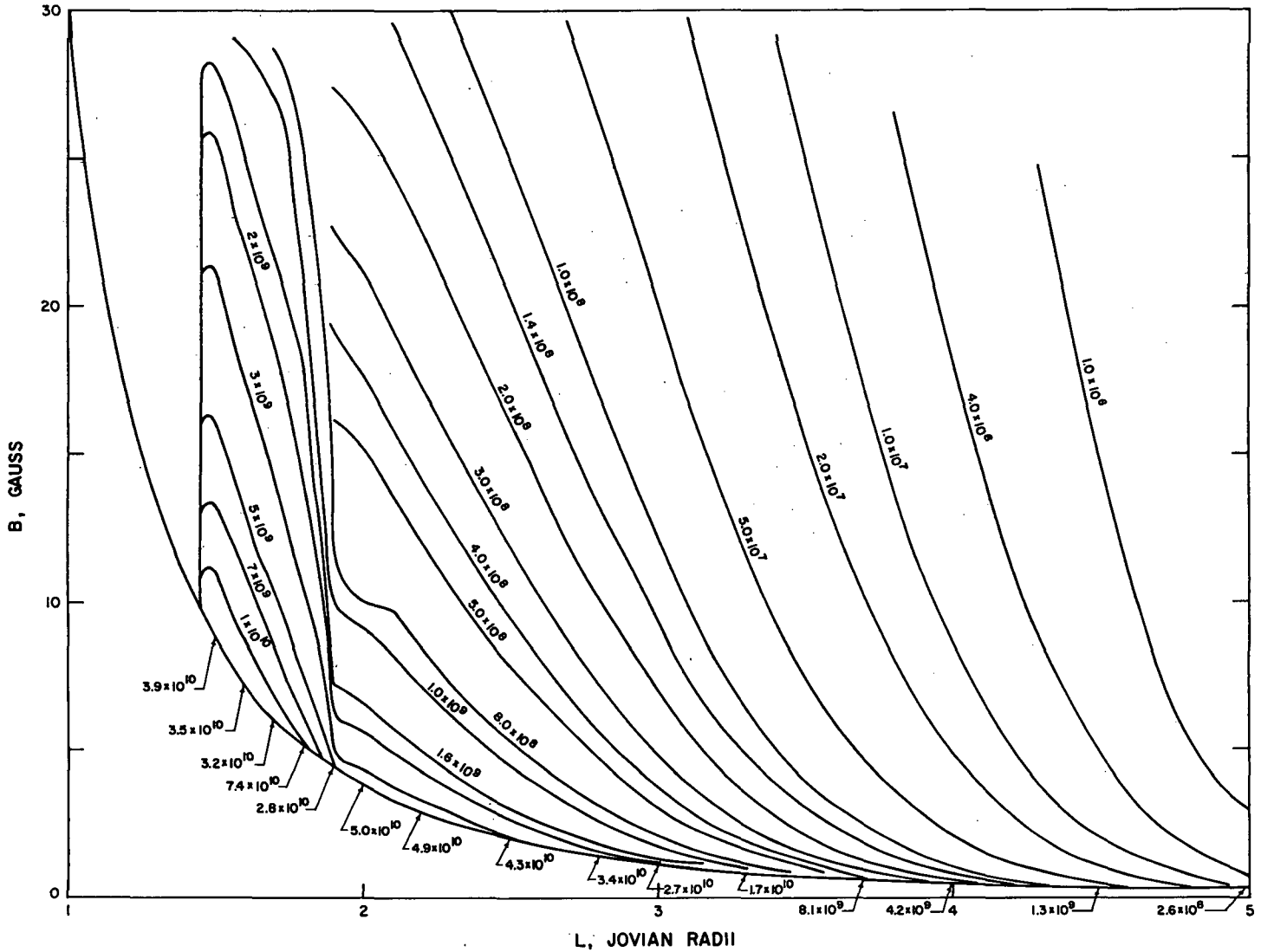

Figure 39. A B-L plot of the electron flux for an outer zone described by Equations (77a) and (77b) and the inner zone described by a square pulse between L = 1.5 and 1.8. The electron flux is in cm^{-2} sec^{-1}. Compared to Figure 38, this distribution shows no significant flux at L < 1.5. Consequently, the oscillations at higher frequencies are increased because a smaller portion of the source undergoes occultation than would be the case in Figure 38. This distribution can account for the predicted oscillations in Figure 33b.

the Earth's if we assume that the surface field of Jupiter is about 30 Gauss. The sudden increases in electron flux at L = 1.8 and L = 2 in the equatorial plane reflect the discontinuities in the anisotropy factor NQ at these L values [See Equation (80)].

6. The Position Angle of the Plane of Linear Polarization

The quantity tan $2\chi = U(u,L)/Q(u,L)$ allows determination of the angle χ between the plane of the linear polarization and the magnetic equator (represented by $\hat{e}_y$ in Figure 3). This quantity was plotted in Figure 13 as a function of u for different L-shells. Clearly, there is a region between L = 1.2 and L = 2 where the angle becomes quite large. However, this is the same region where the degree of polarization, i.e., Q(u,L), shows a minimum produced by the field geometry (See Figure 11). Thus, the intensity of the polarized component from the inner zone, which would cause a significant angular displacement of the plane of polarization from the magnetic equator, may be expected to be only a small fraction of the total emission from the inner zone. Furthermore, the intensity of the emission from the outer zone is greater than that from the inner zone and at least 80 percent of the emission from the outer zone is polarized in the plane of the magnetic equator. As a consequence, we would expect in our present dipole model that the plane of polarization lies in the direction of the magnetic equator at any given longitude.

This is indeed seen to be true in Figure 40 which shows the position angle of the plane of linear polarization relative to the planet's equator as a function of longitude at different frequencies. The sinusoidal curve $PA = 10^{\circ} \sin(\lambda_{III} - 198^{\circ})$ represents the variation in the position angle of the magnetic equator relative to the planet's equator. At different frequencies, we see that the emission remains

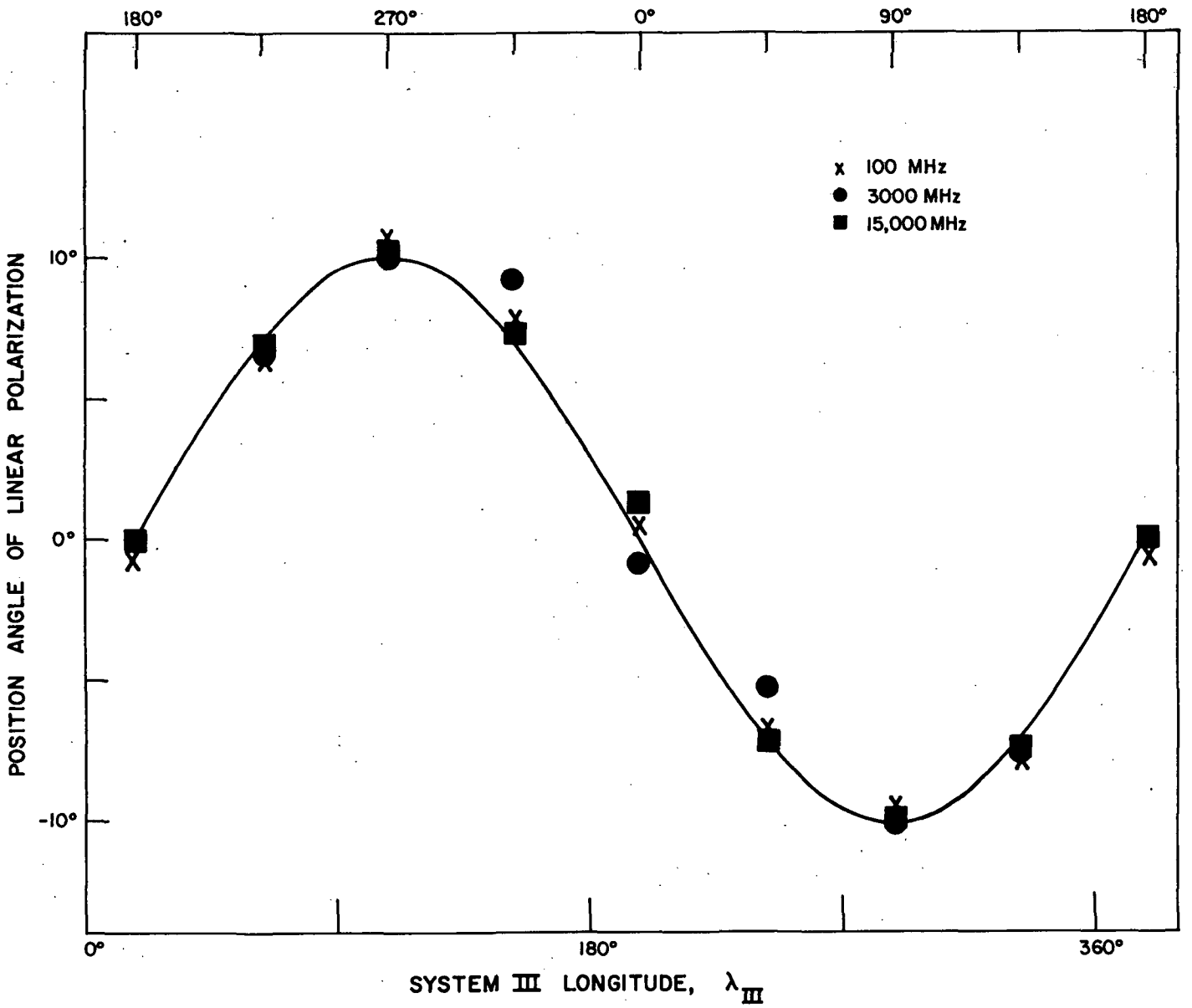

Figure 40. The position angle of the plane of linear polarization in relation to the planet's equator as a function of the longitude. The curve represents the function PA = 10^{o} sin (λ_{III} - 198^{o}).

strongly polarized in the plane of the magnetic equator throughout the rotation of the planet.

Thus, our model does not account for the departure, as observed by Roberts and Komesaroff (1965) from the simple sinusoid of Figure 40 at different frequencies (See Chapter III, Section A). This phenomenon, along with Branson's (1968) asymmetry in east-west strip distributions previously discussed (See Chapter III, Sections A and B-4), is probably best explained in terms of a regional anomaly in the magnetic field (Conway and Stannard, 1972).

CHAPTER IV. CONCLUSION

In summary, the spectral characteristics and longitudinal variation of the Jovian decimetric emission were used to derive the structure of the radiation belts. A double belt system exists such that the outer belt consists of lower energy electrons ($\bar{E}$ = 6.4 Mev if B_S = 30 G) whose equatorial density falls as L^{-4} for $L \geq 2$. The model predicts an equatorial electron density of about 2 cm^{-3} at L = 2 if B_S = 30 G. The inner belt, located in the region $1 < L < 2$, consists of higher energy electrons ($\bar{E}$ = 18 Mev if B_S = 30 G) and has an equatorial density which is about one-half the peak density in the outer zone. The pitch angle distribution of the electrons becomes gradually more confined to the magnetic equator with increasing distance from the planet in the outer region. We find that a distribution which is isotropic for $1.1 < L < 1.8$, 67 percent confined(*) for $1.8 < L < 2$ and 80 percent confined for $L > 2$ satisfactorily accounts for the degree of polarization and the intensity variation with rotation of the planet. The eclipse of the radiation belts by the planet satisfactorily explains the asymmetry of the observed radiation between northern and southern zenomagnetic latitudes of the Earth. The departure from a pure sinusoid in the variation of the orientation of the plane of polarization with Jovian rotation and the asymmetry in east-west components of the source on projected maps are probably better explained by a regional anomaly in the dipole field rather than occultation of the radiation belts by the planet. The observed spectral characteristics of the non-thermal emission are reproduced by

---

(*) The confinement refers to the proportion of electrons which belongs to a population with equatorial pitch angle distribution of the form $\sin^{60} \alpha_e$.

the model although the peak in the spectrum of the total intensity is not as prominent as previously expected. This implies a brightness temperature for the thermal emission from the planetary disk of 180^{o} K at 3000 MHz. B-L plots of the radiation belts show little fine structure except near the boundary of the outer belt with the more energetic inner belt. Electron fluxes are of the order of 1000 times those found in the terrestrial belts if the surface field on Jupiter is 30 Gauss.

LIST OF REFERENCES

Berge, G. L. (1966), Astrophys. J., 146, 767.

Born, Max, and Wolf, Emil (1965). Principles of Optics. Pergamon Press, New York.

Branson, N. J. B. A. (1968), Monthly Notices Roy. Astron. Soc., 139, 155.

Chandrasekhar, S. (1960). Radiative Transfer. Clarendon Press, Oxford.

Chang, D. B., and Davis, L. (1962), Astrophys. J., 136, 567.

Conway, R. G., and Kronberg, P. P. (1968), Planet. and Space Sci., 16, 445.

Dickel, J. R. (1965). "Magnetism and the Cosmos," in Microwave Observations of Jupiter, pp. 296-309. Oliver and Boyd, Edinborough, England.

Dickel, J. R., Degioanni, J., and Goodman, G. (1970), Radio Sci., 5, 517.

Dollfus, A. (1970), Icarus, 12, 101.

Drake, F. D., and Hvatum, S. (1959), Astron. J., 70, 137.

Epstein, I. R., and Feldman, P. A. (1967), Astrophys. J., 150, L109.

Gary, B. L. (1963), Astr. J., 68, 568.

Gulkis, S. (1970), Radio Sci., 5, 505.

Hess, W. N. (1965). The Radiation Belt and Magnetosphere. Blaisdell Company, Waltham, Massachusetts.

Hones, E. W. Jr., and Bergson, J. E. (1965), J. Geophys. Res., 70, 4951.

Ioannidis, G., and Brice, N. (1971), Icarus, 14, 360.

Jackson, J. D. (1966). Classical Electrodynamics. J. Wiley and Sons, Inc., New York.

Lanzerotti, L. J., and Schulz, M. (1969), Nature, 222, 1054.

Legg, M. P. C., and Westford, K. C. (1968), Astrophys. J., 154, 499.

McCormac, B. M. (1966). Radiation Trapped in the Earth's Magnetic Field, p. 129. D. Reidel Publishing Company, Dordrecht, Holland.

McIlwain, C. E. (1961), J. Geophys. Res., 66, 3681.

Melrose, D. B. (1967), Planet. and Space Sci., 15, 381.

Roberts, J. A. (1965), Radio Sci., 69D, 1543.

Roberts, J. A., and Ekers, R. D. (1968), Icarus, 8, 160.

Roberts, J. A., and Komesaroff, M. M. (1965), Icarus, 4, 127.

Scheuer, P. A. G. (1968), Astrophys. J., 151, L139.

Störmer, C. (1955). The Polar Aurora. Clarendon Press, Oxford.

Thorne, K. S. (1963), Astrophys. J. Suppl., 73, 1.

Van Allen, J. A. (1967). Proceedings of the Conference Physics of the Magnetosphere, p. 147. D. Reidel Publishing Company, Dordrecht, Holland.

Warwick, J. W. (1963), Astrophys. J., 137, 41.

Warwick, J. W. (1967), Space Science Reviews, 6, 841.

Westfold, K. C. (1959), Astrophys. J., 130, 241.

Wilkinson, J. E. (1970), Austral. J. Phys., 23, 197.

VITA

Joseph Degioanni was born [redacted] near [redacted]. He attended primary and secondary schools in Rio de Janeiro, Brazil and later in Montreal, Canada. He graduated from McGill University with a B.Sc. with Honours in Physics in 1967. He received the M.S. degree in Astronomy from the University of Illinois in 1969 and entered Northwestern University Medical School that same year. He will receive the M.D. degree in June 1973. He is a member of Phi Kappa Phi Honor Society.